

2

DTIC

16 September 1989

**MF/HF Multistatic Mid-Ocean Radar Experiments  
in Support of SWOTHR**

**Final Report**

Covering the period November 1987 to November 1988

Prepared by:

Alan A. Burns (PI) and Daniel S. Naar

Vista Research, Inc.

100 View St., P.O. Box 998

Mountain View, CA 94042

(415) 966-1171

Contract No. DASG60-88-C-0014

(111387-110388)

Prepared for:

Commander

U.S. Army Strategic Defense Command

Huntsville, AL 35807

Sponsored by:

Defense Advanced Research Projects Agency (DOD)

ARPA Order No. 6237

**DTIC**  
**ELECTE**  
**OCT. 26 1989**  
**S B D**

AD-A213 830



**VISTA RESEARCH, INC.**

100 View Street • P.O. Box 998

Mountain View, CA 94042 • (415) 966-1171

**DISTRIBUTION STATEMENT A**  
Approved for public release;  
Distribution Unlimited

89 10 26 053



# Contents

Illustrations .....	iii
Tables .....	iv
Acknowledgements .....	v
1 Introduction and Summary .....	1
2 SWOTHR Concept .....	3
3 Field Experiment .....	19
3.1 Experiment Description .....	19
3.2 Site/Noise Survey .....	27
3.3 Software Development .....	31
3.4 Experiment Execution .....	39
3.5 Additional Data Processing Steps .....	41
4 Test Results .....	45
4.1 Target Detection .....	45
4.2 Fixed Echoes and Sea Clutter .....	54
4.3 Receiver 2 Target Detection .....	59
5 Conclusion .....	65
References .....	64
Appendix A .....	A-1
Appendix B .....	B-1
Appendix C .....	C-1
Appendix D .....	D-1

For	
NTIS GRA&I	<input checked="" type="checkbox"/>
DTIC TAB	<input type="checkbox"/>
Unannounced	<input type="checkbox"/>
Justification	
By _____	
Distribution/	
Availability Codes	
Dist	Avail and/or Special
A-1	

## Illustrations

Figure 1. SWOTHR concept. ....	3
Figure 2. Example of spatial resolution cell for 0.1-m pulse width. ....	4
Figure 3. SWOTHR data network. ....	6
Figure 4. Early performance predictions. ....	9
Figure 5. Elements of the performance model. ....	10
Figure 6. Individual receiver signals for $f=5$ MHz. ....	14
Figure 7. HF RCS models for the "small threat." ....	15
Figure 8. SNR prediction comparisons using NEC-code RCS values for the "small threat." ....	17
Figure 9. Land-based SWOTHR experiment concept. ....	20
Figure 10. Test site locations. ....	22
Figure 11. Experiment detection-performance predictions: (a)Receiver 1 (North); (b) Receiver 2 (South). ....	24
Figure 12. HF A-4 backscatter RCS. ....	25
Figure 13. Examples of Noise Measurement at (a) Poipu Beach, Kauai, HI (2/7/88 1144 HST) and (b) Morro Beach, Los Angeles, CA (2/12/88 1206 PST). ....	29
Figure 14. Data processing flow. ....	32
Figure 15. Spectral response function. ....	35
Figure 16. Basic elements of an MTT system. ....	36
Figure 17. MTT filter comparisons. (a) Comparison 1. High SNR, single- observation initial estimate. (b) Comparison 2. High SNR, multiple-observation initial estimate. (c) Comparison 3. Low SNR,multiple-observation initial estimate. ....	37
Figure 18. Sample positions relative to the received pulses versus time. ....	43
Figure 19. Range-Doppler frames, first inbound pass, Receiver 1, 5/16/88 Test. ....	46
Figure 20. Target IRTDR vs. time. ....	52
Figure 21. Comparison between the measured SNR and a prediction. ....	54
Figure 22. Clutter examples, Receiver 1, 5/16/8 120213 HST frame; (a) range- Doppler contour plot, (b) spectrum at 162-km IRTDR. ....	56
Figure 23. Spectrum from -8 to +8 Hz at 114-km IRTDR (a) negative side; (b) positive side. ....	58

## Tables

Table 1. Baseline SWOTHR System Parameters .....	8
Table 2. Experimental System Parameters .....	20
Table 3. SNR vs. Estimated Range .....	53
Table 4. SNRs of Echoes from Niihau Island .....	59
Table 5. Ranges (in Kilometers) for Receivers 1 and 2 .....	61

## Acknowledgements

Vista Research, Inc., gratefully acknowledges the excellent support provided by the officers and enlisted personnel of the U.S. Navy Squadron VC-1, Barbers Point NAS, and by the personnel at PMRF, Barking Sands, HI.

Special thanks go to the XO of VC-1, LCDR W. Prince, and to the pilots, Lts. S. Hendrix and J. McCarthy. We would also like to express special appreciation to Mr. R. R. Valencia, Mr. V. Nishina, and Mr. J. Dawson at PMRF for their assistance.

## 1 Introduction and Summary

The objective of this program was to conduct a preliminary field experiment to evaluate and demonstrate several aspects of the multistatic, surface-wave over-the-horizon radar (SWOTHR) concept. SWOTHR was conceived to be an organic asset capable of providing early detection and tracking of fast, surface-skimming threats, such as cruise missiles, for naval battle groups. Physically, SWOTHR consists of a transmitter, a minimum of three separated receivers, a communications link, and a distributed real-time processing and threat tracking system. Specific project goals were to verify detection performance predictions for small, fast targets using ground-wave propagation and to develop a multistatic tracking algorithm. This algorithm was to be used in a non-real-time, post-data-run mode to develop target tracks from the data recorded during the experiment.

The development effort and field experiment were successful in meeting most of the project objectives. A small, low-flying cooperative target (an A-4 attack fighter at 300-ft altitude) was detected at 2.8 MHz beyond the horizon and tracked in range-Doppler space as it flew inbound. At 2.8 MHz, the calculated radar cross section (RCS) of the target was about -15 dBsm. The measured SNR agrees closely with the predicted value. The multistatic tracking algorithm was tested with simulated data.

This effort was a successor to an earlier study phase, in which most of the SWOTHR concept was developed and described [1]. Results from a performance simulation model created during the earlier effort showed that a SWOTHR system had significant potential for protecting a naval battle group from such threats.

Equipment was assembled, modified, and built outright in order to make a modest set of measurements with a reduced SWOTHR configuration. This configuration used two, rather than three, receivers; the resulting track ambiguity was acceptable for a test using a cooperative target. Our approach was to minimize construction of specialized hardware by using readily available components such as communications receivers and by simulating real-time receiver operation in digital data processing. The experiment was fielded in a mid-ocean environment (PMRF Barking Sands, Kauai), and a short test series consisting of three flights was conducted using A-4 aircraft as a cooperative targets. The transmitter and receivers were set up as close to the shoreline as possible and were essentially at sea level. About four hours of data were collected at 2.8 and 7.8 MHz.

Only a small part of the data has been scrutinized. An unanticipatedly large temporal slip between the transmitted pulse rate and the receiver digitization clock had the effect of introducing a high, artificial noise level. Compensating for this problem greatly complicated and slowed the data reduction effort. In addition, one of the receiver front ends had evidently burned out some time during the tests. This loss of sensitivity was not uncovered until bench tests were made after the field experiment (in order to verify suspicions that there had been such a loss). There is conflicting evidence concerning when this occurred. It appears that it may not have had a practical effect, since background-noise-limited operation was observed. However, this issue remains open.

In addition to the flight tests, a series of daytime background noise surveys was made in Hawaii and along the California coast. These consisted of frequency spectrum scans using a short vertical antenna. Noise levels from Kauai consistently exhibited dips between 2 and 6 MHz, in general agreement with CCIR predictions. No such minima were seen at sites in northern and southern California; noise levels above 6 MHz were about the same in Hawaii and California. It appears that the CCIR minima are real and can be observed in an isolated, essentially open-ocean setting, and were filled in by man-made noise on the California coast. The noise level and spectral character are important issues for HF radars, including the SWOTHR concept.

## 2 SWOTHR Concept

**Basic Description.** Figure 1 is a cartoon illustration of the SWOTHR concept. It relies on low-loss propagation of MF/HF (2- to 20-MHz) signals via the vertically polarized ground-wave mode to reach over the horizon. This propagation mode is particularly strong in a maritime environment due to the high electrical conductivity of sea water. The optimum wavelength is a complex tradeoff between propagation loss, which favors low frequencies, threat rcs, which favors high frequencies, and atmospheric noise levels, which are very variable. At these wavelengths (15 to 150 m), antennas with beamwidths having adequate angular resolution are impractically large for shipboard installation. SWOTHR overcomes this limitation by employing a multistatic radar approach, where separated receivers are used to provide spatial resolution. Physically small antennas such as vertical whips are postulated for SWOTHR. Besides minimizing the impact of shipboard installation, this approach affords continuous 360° coverage, and the effects of other structures on the ship on system performance due to beamshape distortions are lessened because SWOTHR does not rely on beamshape for tracking.

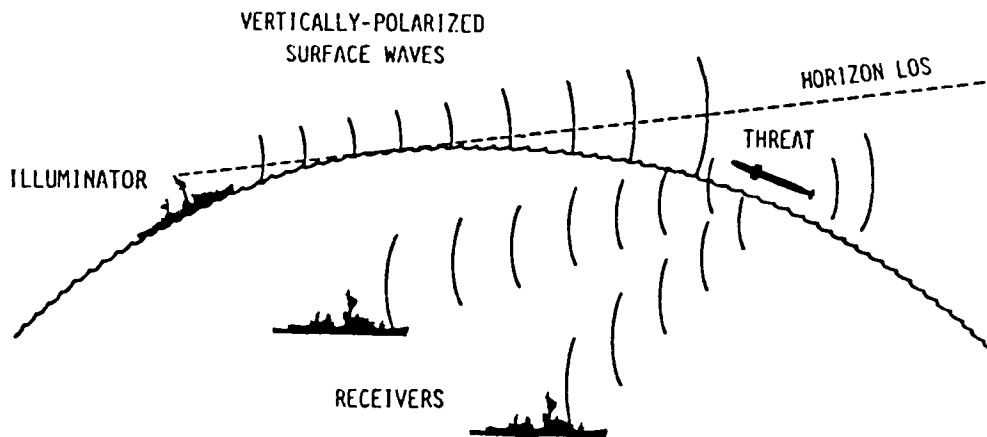


Figure 1. SWOTHR concept.

The basic SWOTHR configuration consists of one transmitter and three receivers. Other configurations are possible, such as two-transmitter/two-receiver and three-transmitter/one-receiver arrangements. At least three separated elements are needed to form an unambigu-

ous track. It is not necessary to use the same frequency in the multiple transmitter arrangements. These alternative arrangements may have value in some circumstances for countering ECM efforts. Here, however, we will concentrate on the basic configuration.

**SWOTHR Tracking.** SWOTHR tracking is based on measuring the time-difference-of-arrival (TDOA) between the direct signal from the transmitter to a receiver and the signal reflected from the threat and measuring the Doppler shift between those signals. TDOA/Doppler measurements from a minimum of three receivers are needed to locate a threat unambiguously. Figure 2 illustrates the intersection of three TDOA ellipses, which produces an odd-shaped resolution cell elongated in azimuth, or cross-range direction. Because differential Doppler shifts depend on both threat position and its velocity vector and are more sensitive to azimuthal position than to range, the Doppler information improves azimuthal resolution. The uncertainty in threat location is further reduced as more points are added in the process of tracking the threat. Actual spatial resolution depends on the details of the SWOTHR deployment and threat sector. Results from simulated tracks and analytic considerations indicate that the expected SWOTHR cross-range resolution is in general approximately equal to resolution in range.

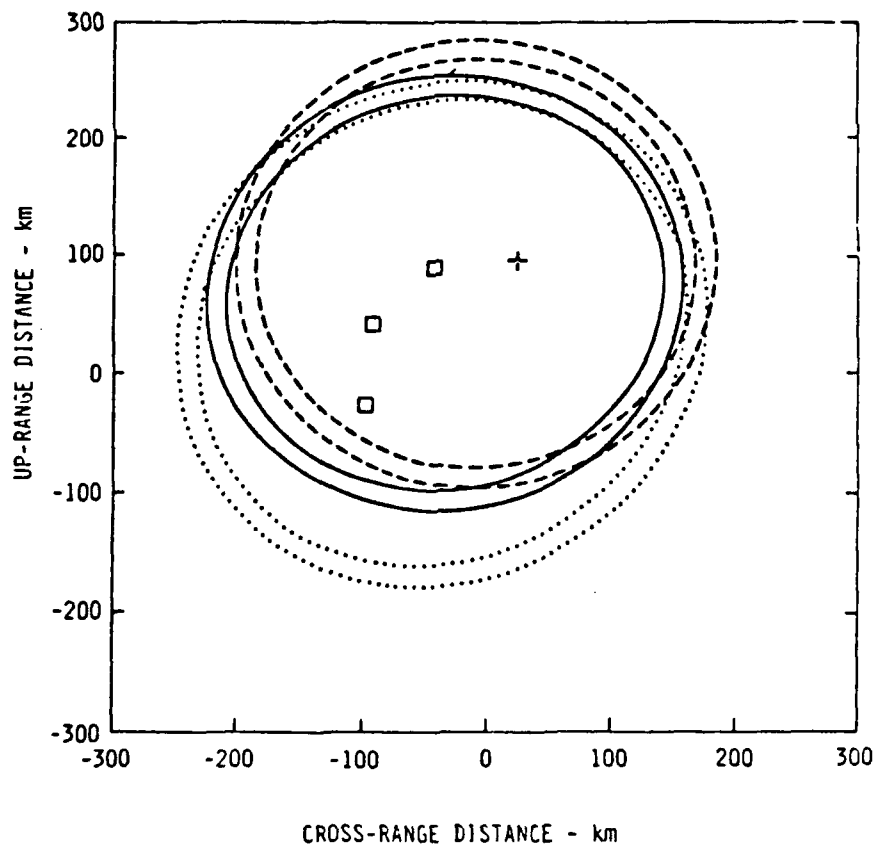


Figure 2. Example of spatial resolution cell for 0.1-m pulse width.

In the SWOTHR concept, threat tracks are formed in a two-step process. First, tracks are established at the individual receivers as trajectories in TDOA/Doppler space. Then the individual TDOA/Doppler tracks are combined into spatial-domain tracks of the threat's geographical position and velocity vector.

Each receiver uses the direct signal from the transmitter as its reference; there is no requirement for precise absolute timing. Individual receiver signal processing consists primarily of suppressing impulsive noise bursts, resolving the received signals into TDOA/Doppler cells (presumably by means of a parallel FFT processor acting on a number of time-delay cells simultaneously), setting thresholds and comparing TDOA/Doppler cell levels to those thresholds, and establishing track files in TDOA/Doppler space. These files comprise the individual receiver outputs, which are then transmitted to other SWOTHR elements. It is also necessary to report SWOTHR element position information.

Since all SWOTHR elements can access the same information, each element can operate independently and in parallel to calculate the final geographical tracks. This eliminates the need to broadcast track data from a central processor back to SWOTHR elements. Figure 3 depicts a SWOTHR net. It is envisioned that an individual SWOTHR element would actually only need to process TDOA/Doppler track data from cells most relevant for its situation regarding location and threat characteristics. Note that non-active elements (i.e., those neither transmitting nor receiving) can access the TDOA/Doppler data and thus also assemble final tracks. More than one SWOTHR net can operate simultaneously, and it is also envisioned that SWOTHR nets may be dynamically constituted and reconstituted as the tactical situation changes.

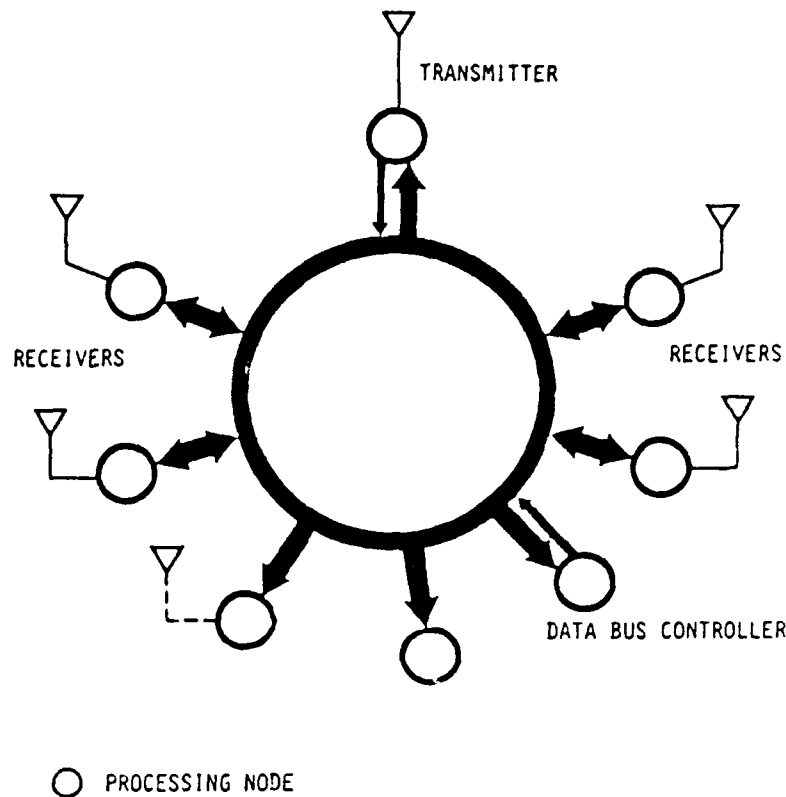


Figure 3. SWOTHR data network.

Producing a geographical track is a rather complex task involving the simultaneous solution of six second-order equations even for a single threat. Having to deal with the real-life situation with multiple targets and false-alarm tracks significantly increases the processing effort because it is necessary to correctly associate TDOA/Doppler tracks by means of the individual receivers and eliminate false tracks. Although the brute-force approach of attempting to solve all possible track combinations rapidly becomes prohibitive, various means to reduce the workload can be devised. This issue is discussed in the previous SWOTHR report [1].

**SWOTHR Performance Predictions.** A computer code to predict signal-to-noise ratio (SNR) was developed in the earlier effort in order to evaluate potential SWOTHR performance. Besides incorporating the primary radar-equation elements---ground-wave propagation loss, threat rcs, and atmospheric noise level---the model also contained elements to account for sea state, to estimate bistatic clutter level and spectral extent, and to predict direct signal levels from the transmitter at the receivers. The latter are important because the receivers must operate in the presence of a strong signal from the transmitter and clutter from sea scatter, which makes the required dynamic range of the receivers an issue, as with all HF radars. (An essentially continu-

ous transmitted waveform is vital to SWOTHR in order for it to maximize the pulse-compression factor (PCF), which is required to provide adequate sensitivity without demanding peak powers incompatible with a shipboard installation; the dynamic range requirement on the receivers is mitigated significantly by the fact that most of the receiver stages only need to deal with the uncompressed direct signal.) In the earlier study, this code was used to predict experimental system performance as well.

Figure 4 repeats some earlier modeling results. Shown are predicted SNRs assuming coherent summation of the individual receiver output signals for three different noise models. These models, whose spectral characteristics are shown in Figure 5c, are based on the standard predicted atmospheric noise levels taken from the CCIR reports [2, 3] at the "30-" and "50-dB" 1-MHz reference levels and on the so-called "QMN" (Quasi-Minimum-Noise) level. QMN noise is used as a rule-of-thumb model by HF naval communications engineers as an approximation for the minimum noise level, including ship noise. For these calculations, the SWOTHR elements are assumed to be deployed on the corners and in the center of a 20-km square box as shown in the inserts in Figure 4. Threat range is measured to the center (i.e., to "R<sub>3</sub>") and the threat is assumed to approach in a horizontal attitude along the direction of the arrow. Some of the results shown in Figure 4 have been updated by means of calculations with an improved rcs model; these are discussed and presented below. Better SWOTHR performance is predicted by the new calculations.

Table 1 lists the "baseline" SWOTHR system parameters assumed for these calculations. Coherent integration times were somewhat arbitrarily chosen to be 4 and 20 s for performance calculation examples; however, they roughly match the dwell time of incoming threats in range cells.

**Table 1. Baseline SWOTHR System Parameters**

---

***Transmitter***

Radiated Power (Average and Peak)	10 kW
Antenna Directive Gain	1.5 db
Antenna Height	10 m
Pulse Repetition Frequency	500 s <sup>-1</sup>
Pulse Compression Factor	20
Compressed Pulse Width	0.1 ms

***Receiver***

Antenna Gain	1.5 dB
Antenna Height	10 m
Instantaneous Bandwidth	0.05 Hz
Coherent Integration Time	20 s
Noise Bandwidth	0.05 Hz

***Environment***

Sea State	3
Atmospheric Noise (re kT)	30 dB CCIR, 50 dB CCIR, QMN

---

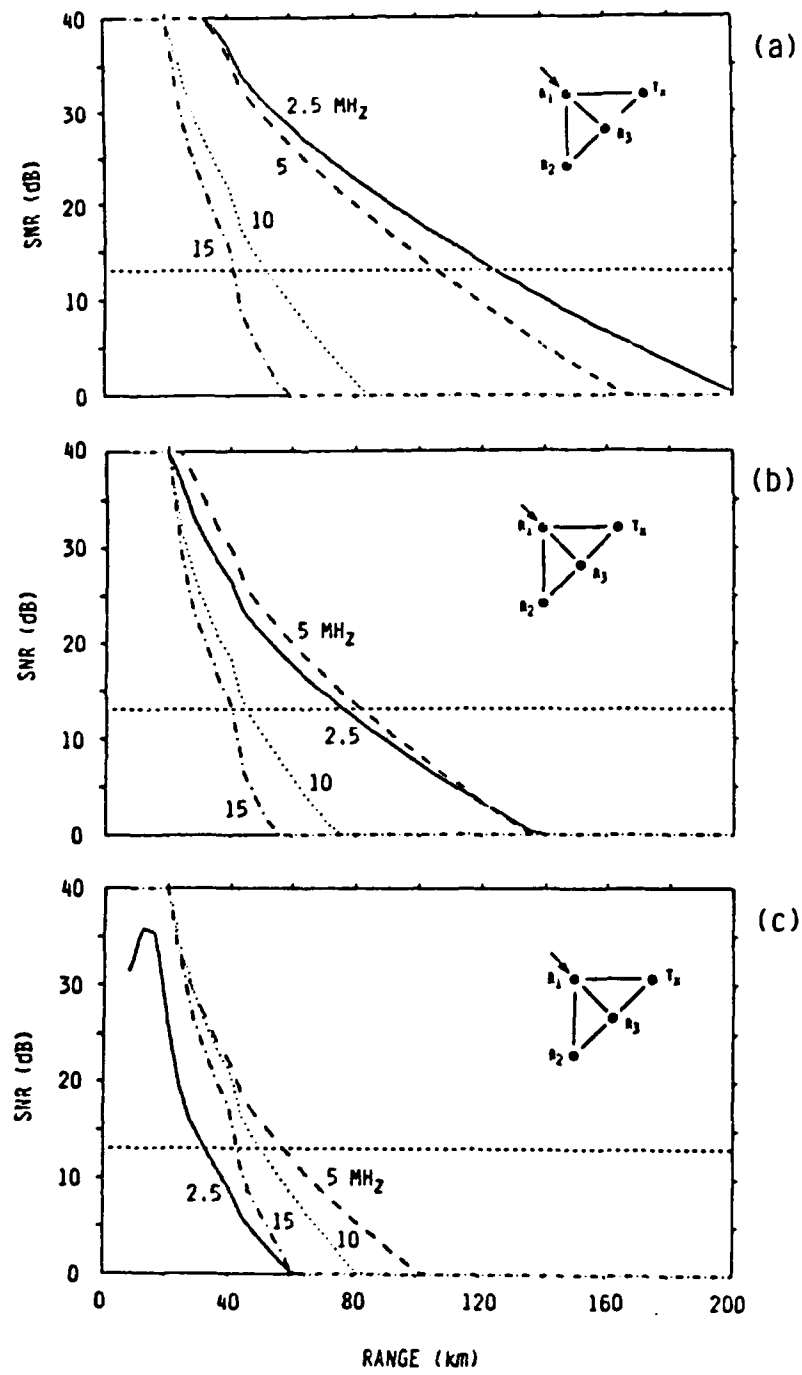


Figure 4. Early performance predictions.

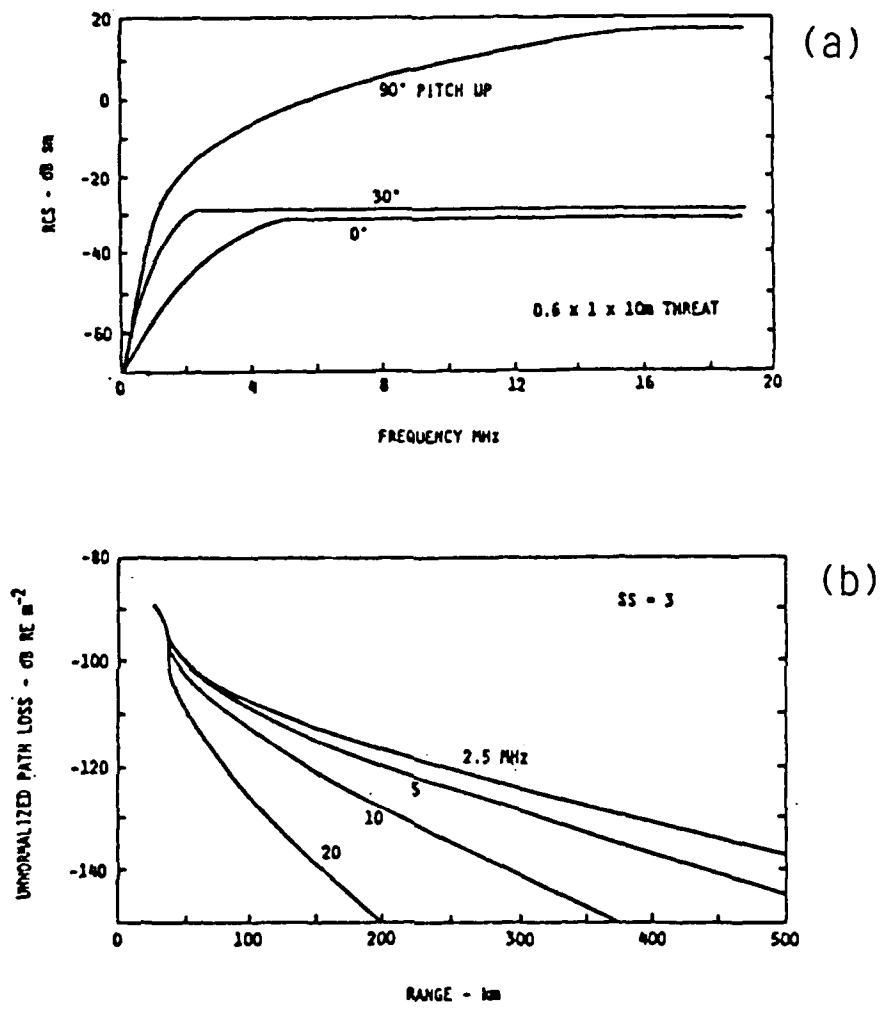


Figure 5. Elements of the performance model.

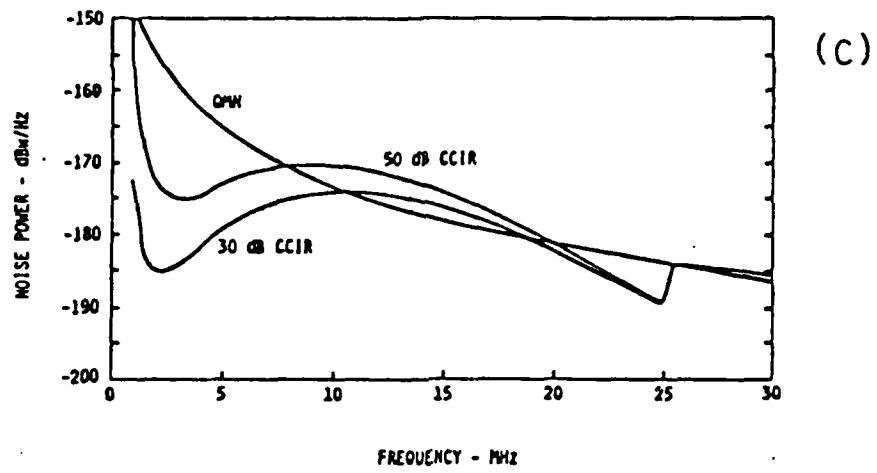


Figure 5 (concluded). Elements of the performance model.

The threat of interest was a generic  $1 \times 0.6 \times 10$  (HWL)-m cruise missile very conservatively modeled as the Rayleigh, and geometric-optics asymptotes of a wingless, finless, prolate ellipsoid (this is referred to as the "small threat"). This model permitted estimation of bistatic rcs for arbitrary illumination. An example showing the backscatter rcs for a vertically polarized field incident in a plane containing the major axis of the ellipsoid is shown in Figure 5a for three pitch attitudes. There are sizeable increases in rcs when an elongated object has a large projected dimension along the vertically polarized ground-wave electric field, which means that a threat will be more detectable at long range at least briefly during a vertical launch phase.

Calculation of the ground-wave propagation loss was the other major part of the model. These calculations were made with a computer program written by Fulks [4] based on formulas developed by Bremmer [5] that predict the surface wave electric field strength. The standard "4/3rds earth" model was used to make modifications to the program in order to account for atmospheric refractivity, and Barrick's formulation [6] was used to make modifications to account for sea state. The path loss,  $P_l$ , can be expressed in terms of the electric field strength,  $E$ , by

$$\begin{aligned}
 P_l &= \frac{\text{Power density at threat or receivers (W/m}^2\text{)}}{\text{Isotropic power radiated (W)}} \\
 &= \frac{E^2/\eta \times 10^{-12}}{10^3} \text{ m}^{-2} \\
 &= -175.8 + 20 \log(E) \text{ dB re m}^{-2}
 \end{aligned}$$

where  $\eta = 377$  ohms and  $E$  is the field strength in microvolts/m due to a 1-KW isotropic radiator. Note that this is an unnormalized path loss, in units of  $\text{m}^2$ . Figure 5b shows how  $P_l$  varies with frequency for Sea State 3. Higher sea states generally increase the path loss and affect the higher frequencies more strongly.

Three major findings emerged from the early study:

- A SWOTHR system with practical parameters had the theoretical capability of detecting surface-skimming threats with radar cross sections lower than -30 dBsm out to 55 nm in a daytime maritime noise environment.
- Operation at lower frequencies than anticipated was favored under low-noise conditions.
- Reducing the atmospheric background noise, especially at night, was the key issue.

*Quasi-Coherent Processing Gain.* It can be shown [1] that the near-equivalent of the processing gain attainable by simultaneously and coherently combining the receiver output signals appropriately can be achieved by setting lower track thresholds at the individual receiver TDOA/Doppler processing stage. For example, coherently combining three equal-strength receiver output signals furnishes about a 5-dB gain. The coherently added signal can then be compared to a threshold level such as 13 dB SNR for the desired probability of detection and false-alarm rate. Alternatively, all three of the individual signals can be required separately and simultaneously to exceed an 8-dB SNR threshold. This leads to essentially the same detection performance statistics as before, and the lower threshold is equivalent to a gain of 5 dB more.

One of the major advantages of this "quasi-coherent" multiple-receiver processing is that coherence between receivers is not required, which would be very difficult to implement in a moving, changing environment because the locations of the transmitter and receivers would have to be known to a small fraction of the rf wavelength. Another important advantage is that data transfer requirements are greatly reduced because only processed track data rather than full receiver bandwidth signals need to be sent. Setting a lower threshold on the individual receiver outputs does produce a penalty in increasing the false-alarm rate at that level, but that should be a manageable challenge. Estimated data transfer rate requirements are 1 to 2 kbits per second per receiver for 100 to 300 actual and false-alarm tracks.

Figure 6 illustrates this effective processing gain. Shown are the individual receiver SNR's for the same scenario as used to generate the 5-MHz curve presented in Figure 4(a). All three individual receiver outputs are above the 8-dB threshold at ranges closer than about 105 km, which is close to the maximum range for which the coherent sum exceeds a 13-dB threshold.

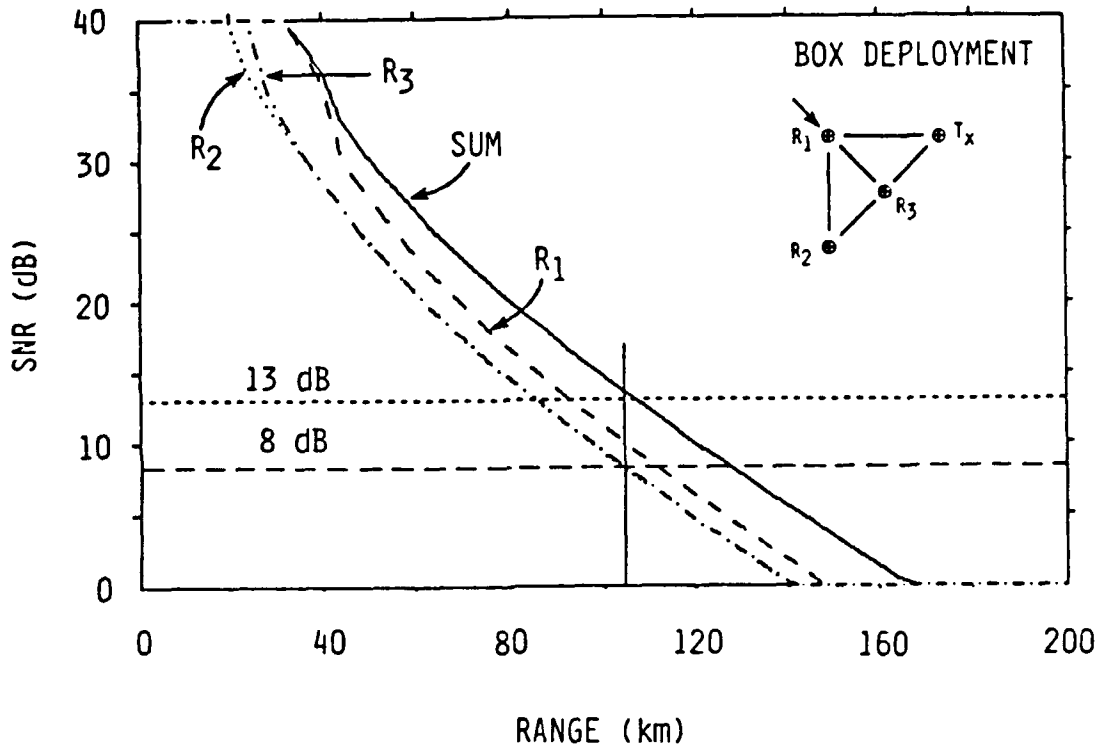


Figure 6. Individual receiver signals for  $f=5$  MHz.

**Updated SWOTHR Predictions.** Much of the bias toward low-frequency operation comes from the rcs model, which is shown for backscatter in Figure 5b for several pitch-up attitudes of the missile. Although it was known that the rcs was conservatively modeled, more recent exact numerical calculations show that the rcs of this object is as much as 17 dB higher in the resonance region than the geometric-optics (high-frequency) asymptote (Figure 7). Furthermore, protuberances such as fins will further increase the rcs and fill in the null seen at 15 MHz in Figure 7. Most of the discrepancy between the old model and the new results is due to the low strength of the geometric-optics asymptote. Since the geometric-optics asymptote is entirely controlled by scattering from the nearest tip and depends on local curvature there, it is not likely to be a good approximation. The higher rcs values predicted by the exact calculations will improve overall predicted SWOTHR performance and tend to overcome the increased propagation losses at higher frequencies. This would shift the optimum operating frequency to shorter wavelengths and broaden the range of useful wavelengths.

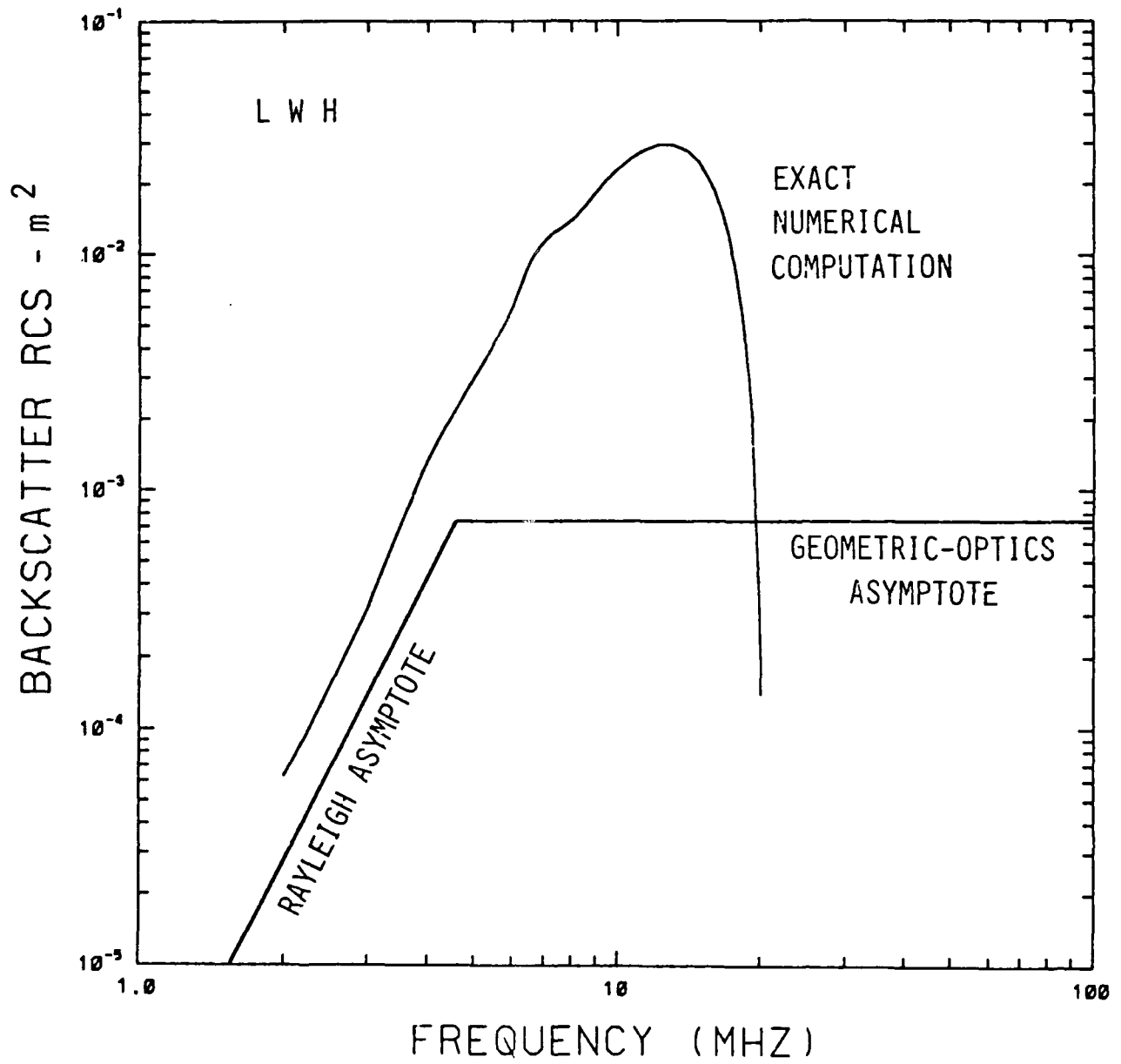


Figure 7. HF RCS models for the "small threat."

Another contributor to the bias toward low frequencies is our preference of daytime CCIR noise models over others such as QMN. QMN noise includes both external and ship-generated noise, and is based on a broad set of conditions that include all times of day, all seasons, and multiple world-wide locations [7]. Recently measured daytime shipboard noise levels were often under QMN levels, particularly below 6 MHz, which implies that external noise may be dominant and, in turn, may reflect successful attempts to clean up the shipboard noise environment [7]. These considerations were used to justify using the CCIR models for daytime SWOTHR performance predictions. The Kauai measurements support this choice.

Nighttime operation is another matter. The earlier report identified this as an important issue and pointed out that some sort of noise cancellation would be needed to provide equivalent performance during the night, when the ionospheric channel opens up to permit long-range propagation at lower frequencies and thus leads to dramatic increases in noise level. Noise cancellation based on polarization, which exploits the fact that ionospherically propagated noise is randomly polarized while the desired ground-wave echoes are strictly vertically polarized, may be the best and simplest approach.

Locally generated noise is mostly impulsive in nature. It can be more easily dealt with than high levels of continuous background noise because individual impulses can be excised over the coherent-processing interval without having much effect.

Figure 8 compares SNR predictions based on the new calculations with improved rcs values with those shown in Figure 4b. These predictions apply for the small threat and a 50-dB CCIR noise model. From this, the following tentative conclusions may be drawn:

- Potential SWOTHR performance is significantly better than originally predicted for the physically small threat studied earlier, particularly above 5 MHz.
- There is less variation in performance with operating frequency, which means that SWOTHR has the option of operating over a substantially wider frequency band with less effect on performance than originally believed.
- Low HF-band operation is still favored for these categories of targets, though not as strongly.

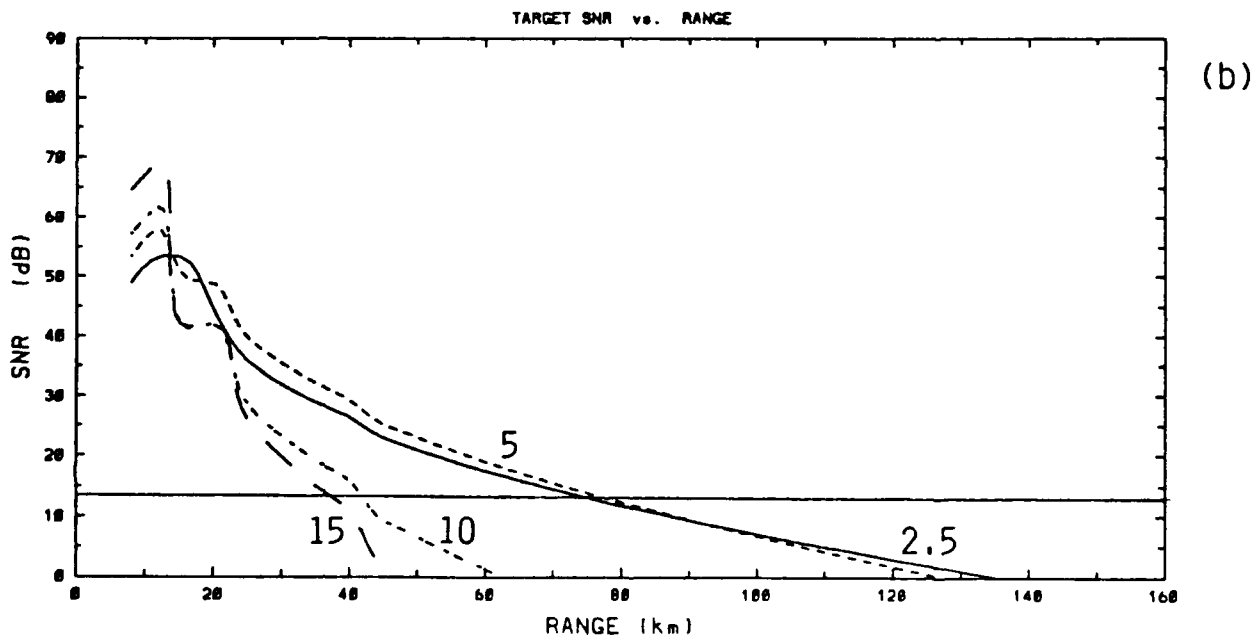
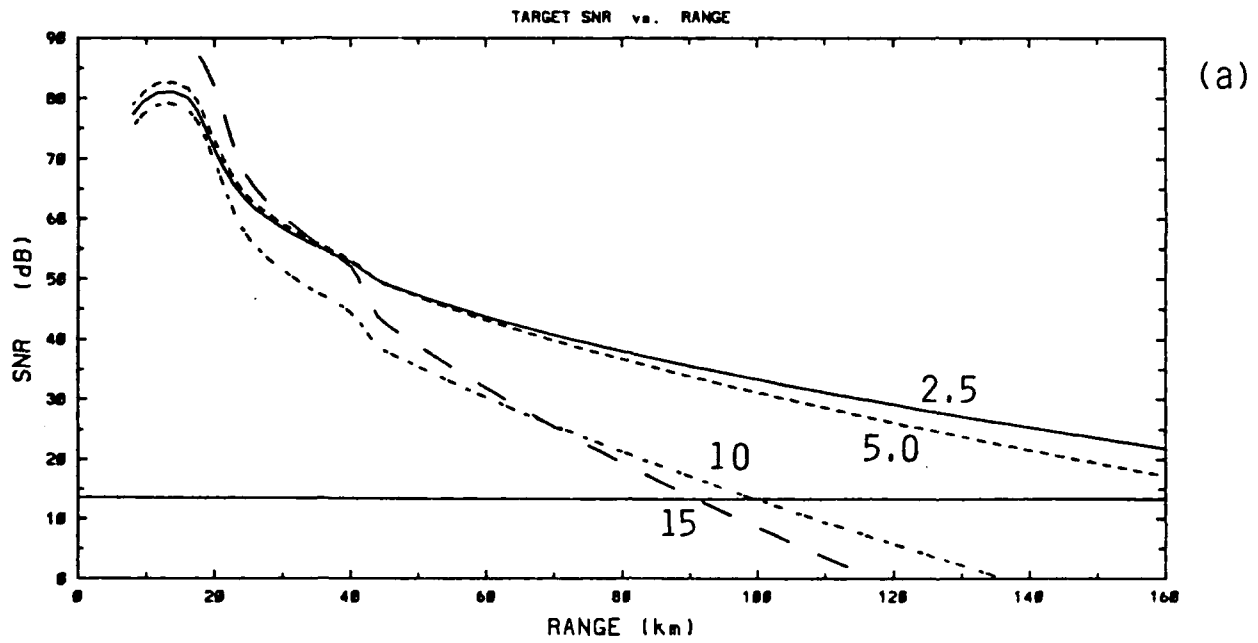


Figure 8. SNR prediction comparisons using NEC-code RCS values for the "small threat."

The findings from the earlier study greatly affected the design of the experiment described in this report. In particular, it influenced the choice of 2.8 and 7.8 MHz as operating frequencies for the flight tests. Later calculations of predicted SNR for the test conditions using exact rcs values validated these choices. SNR predictions using the test target and conditions are presented in Section 3.

### 3 Field Experiment

#### 3.1 Experiment Description

The field experiment was a shoreline-based SWOTHR deployment using a reduced configuration with only two receivers (Figure 9). The resulting two-fold target position ambiguity was deemed acceptable for a shoreline-based test using a cooperating target. That is, all tracks would be assumed to be on the seaward side of the bisectors between transmitter and receivers. The use of two rather than three receivers also reduces the potential processing gain from about 5 to about 3 dB (or, alternatively, requires raising the individual receiver thresholds from 8 to 10 dB). This difference is essentially negligible.

Placing the antennas on land (especially for the low-conductivity soil that characterizes the Hawaiian test site) produces a performance penalty due to antenna ground losses, poor propagation to the shoreline, and a mismatch loss at the shoreline. Although these losses can be minimized by using appropriate ground planes and installing the antennas as close to the water as feasible, it was decided to make up at least part of the loss by providing 5-dB directive antenna gain. Thus, unlike the SWOTHR concept, which calls for continuous 360° coverage, the experiment used two-element antennas with broad main lobes directed out to sea.

Another compromise was the use of a simple pulse-Doppler transmitter waveform rather than a compressed one. In addition, it was not feasible to employ a transmitter more powerful than 2 kW. The pulse width (64  $\mu$ s at the -6 dB points) and waveform were designed to match the impulse response of the receiver. The range of prf's, whose time interval could be selected in increments of 256  $\mu$ s, was chosen as a compromise between high average power, unambiguous range, and data storage limitations, and to permit shifting any sky-wave backscatter out of the target range. Finally, the test system differed from the SWOTHR concept in that there were no data links between elements and data processing was to take place after the tests rather than in real time. Table 2 lists the test system parameters and compares them to those of the "baseline" SWOTHR system. Although the test system thus had to be built with several compromises in order to permit fielding within time and resource constraints, which tended to make it appear somewhat unlike the SWOTHR concept in detail, it theoretically was capable of meeting the test objective of demonstrating over-the-horizon multistatic radar tracking of small, high-speed targets with ordinary hardware.

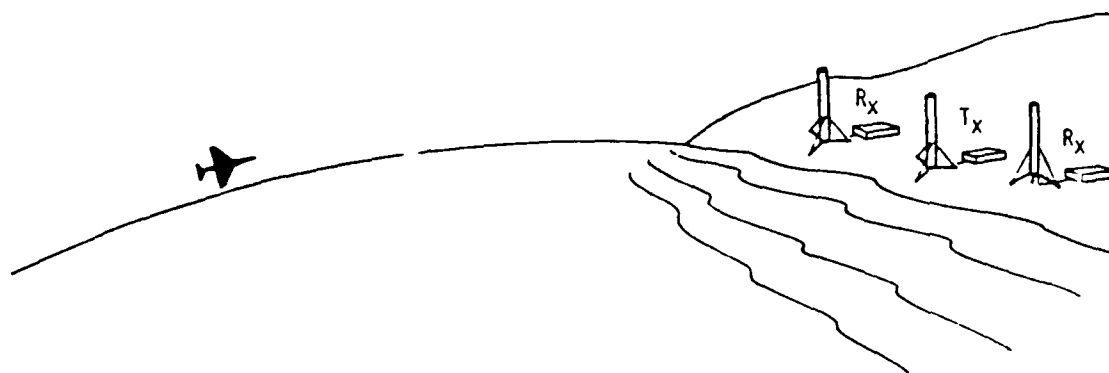


Figure 9. Land-based SWOTHR experiment concept.

Table 2. Experimental System Parameters

	Experimental System	SWOTHR
Frequency (MHz)	2.8 & 7.8	
Peak Power (kW)		
-- Transmitter Output	2	
-- Radiated	0.34 (2.8 MHz) & 0.56 (7.8 MHz)	10
PRF (s <sup>-1</sup> )	244/391	500
Pulse Compression Factor	1	20
Matched Pulse Width (μs)	82	100
Antenna Directive Gain (dB)	4.8	1.5
Antenna Height (m)	2	10
Receiver Bandwidth (kHz)	15	10
Coherent Integration Time (s)	13/26	20
Spectral Processor Loss (dB)	3	1

Details of the experiment design and the equipment appear in Appendices A and B. Appendix A contains excerpts from the formal Test and Operations Plan written prior to fielding in order to guide test execution. We note that the test equipment was portable, and, except for the larger transmitting antennas, which were in a relatively secure location, was packed up every evening and set up again in the morning.

The range resolution of the experimental system was set by the 15-kHz bandwidth available with the receiver modified for these tests. Analysis and tests showed that the receiver was well matched by a raised-cosine transmitter waveform. The resulting matched-filter output waveform was a pulse with a 82- $\mu$ s width at the 50% response points (Appendix B). This corresponds to a range resolution of about 12 km. At 450 kn, the A-4 aircraft used as cooperative targets thus have an effective dwell time of up to about 52 s at each range delay.

In principle, a 52-s effective integration time would provide the best match and highest SNR, at least for a directly incoming target. However, achieving that would require that the target maintain its "radial" velocity to within 1 kn, or 0.2%, for long periods. This is too stringent, so shorter integration times were planned.

The Kauai test site was chosen for the following reasons:

- It provides a reasonable approximation of an open-ocean environment and fairly good access to the shoreline for several sites.
- It was expected that man-made noise would be low due to the remoteness of the test site, which was far from population centers and heavy industrial activity. A noise survey (Appendix C) confirmed this expectation.
- It was anticipated that there would be a low level of other high-speed aircraft activity that might compete with tracking the cooperating target.
- Range support and security from PMRF Barking Sands might be provided, as well as borrowed frequency allocations.
- The site provides good logistics from the West Coast.

Figure 10 is a map of the final receiver and transmitter locations chosen. Also shown are the respective  $4/3$ rds-earth radar-horizon arcs for an aircraft at 300-ft altitude and a typical flight path. Negative aspects of this site were the presence of strong fixed echoes from Niihau Island, potential interference from the nearby WWVH transmitters, and relatively difficult intersite communication.

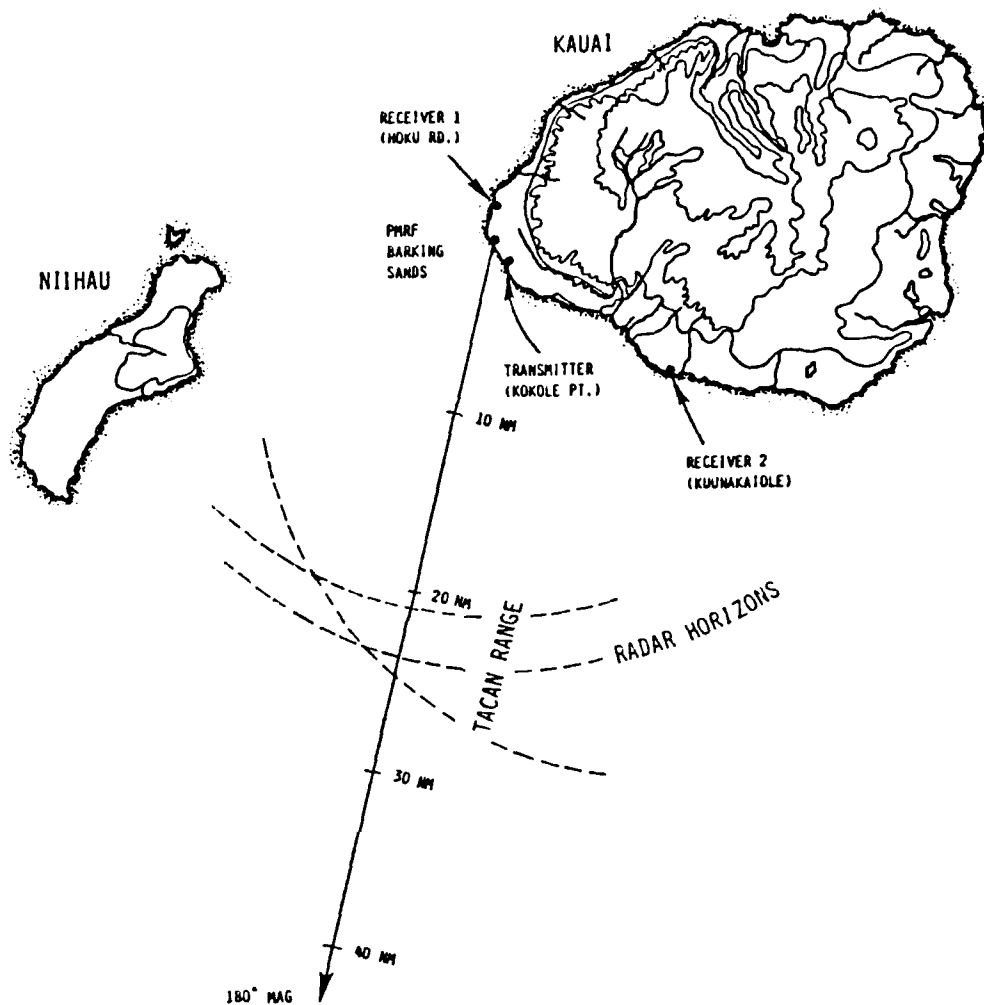


Figure 10. Test site locations.

Individual-receiver output SNRs were recalculated using these locations and the exact rcs of a model for the A-4 target aircraft. These new SNR predictions are presented in Figure 11, and supercede the initial combined-receiver SNR predictions issued in the Test and Operations Plan (Appendix A). Figure 12 shows the backscatter rcs of the A-4, which was modeled as illustrated because the horizontal flying surfaces contribute negligibly to electromagnetic scattering of the vertically polarized ground wave. It is not surprising that the dominant scatterer is the vertical stabilizer, because of its elongation in the direction of the electric vector. A 56-dB CCIR atmospheric noise reference level was used for the curves

presented in Figure 11, and the coherent integration time was assumed to be 16 s; they also apply for other combinations, such as a 50-dB CCIR reference level and 13-s integration. The other parameters are as presented in Table 2. Because of system-parameter uncertainties and the highly variable background noise level, the "predictions" of Figure 11 are to be considered useful for general guidance only. Although we tried to make these estimates realistic, they were thought to be conservative.

The discontinuities seen at various ranges in Figure 11 are produced by the surface-wave field-strength (propagation-loss) calculation, and represent transitions from predominantly line-of-sight to predominantly ground-wave propagation conditions. These occur at the three target-to-transmitter ranges that correspond to the points where the target goes below the horizon at the two receiving sites and the transmitter.

Figure 11 predicts that the A-4 should be detectable above a 10-dB threshold at over-the-horizon ranges at both receivers and for both the 2.8- and 7.8-MHz chosen test frequencies. For the A-4 target, operating much above 7.8 MHz would not have improved detectability because the increase in rcs (Figure 12) is more than compensated for by the rapidly increasing propagation loss (Figure 5) with frequency. As will be seen in the next section, the expected atmospheric noise level was relatively flat with frequency above 8 MHz and thus would not have been a significant factor. The 2.8-MHz test frequency was near the relative minimum atmospheric and man-made noise level. Even though 7.8 MHz benefitted from a relatively high rcs and better transmitter antenna efficiency, the predicted target detectability was not as good at 2.8 MHz due to poorer ground-wave propagation.

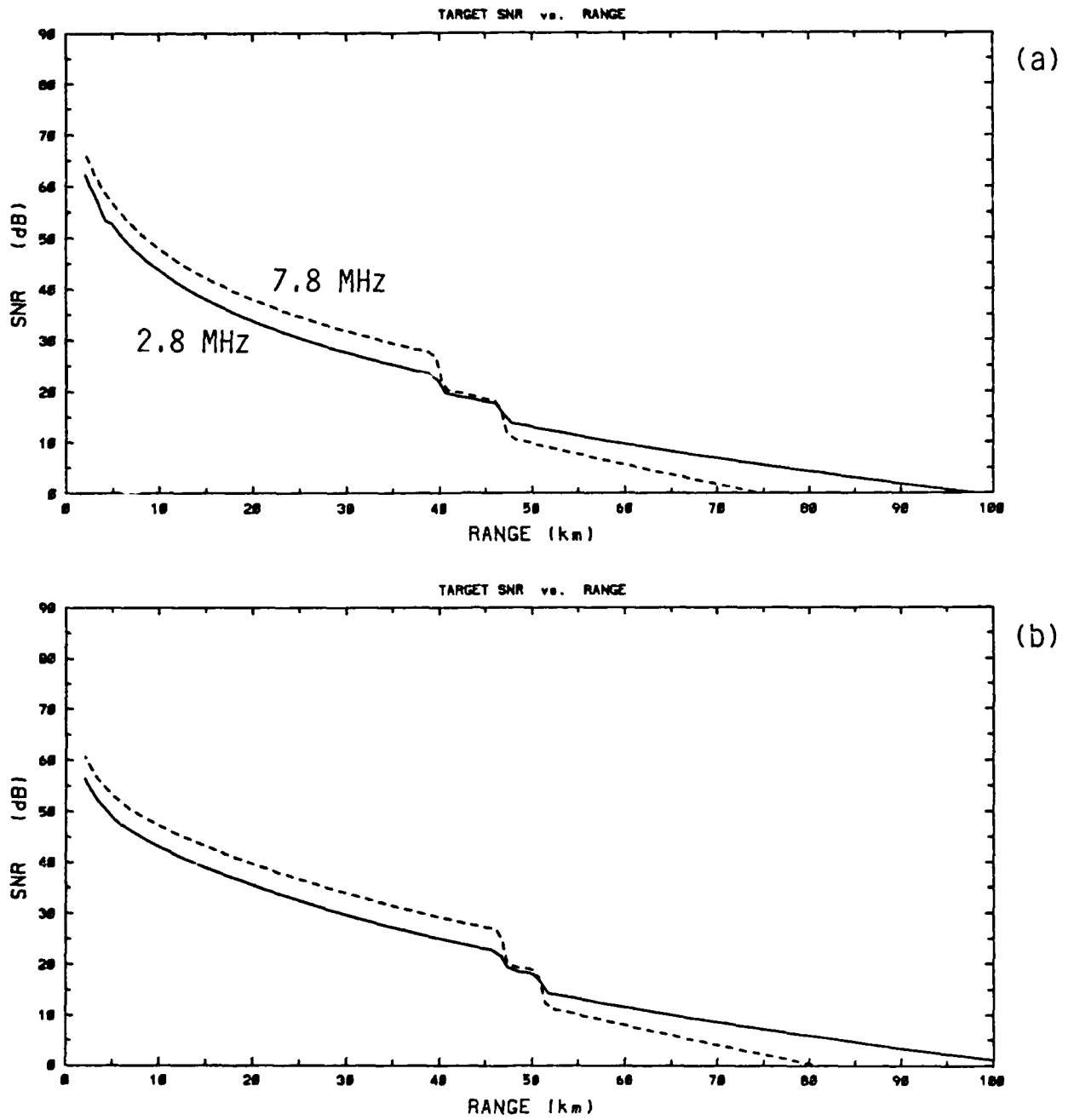


Figure 11. Experiment detection-performance predictions: (a) Receiver 1 (North); (b) Receiver 2 (South).

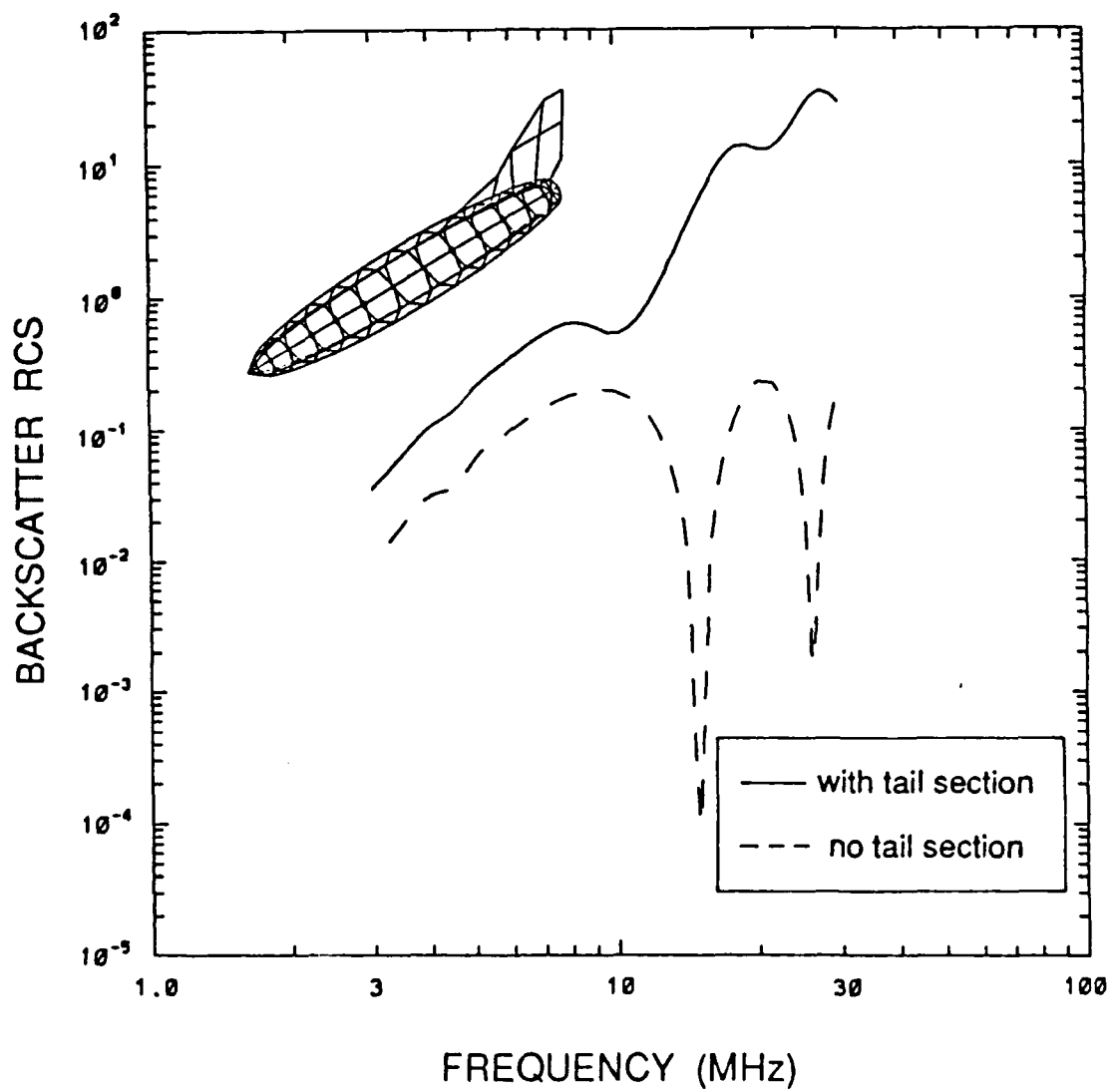


Figure 12. HF A-4 backscatter RCS.

One somewhat unusual feature of the receiver detector was the use of a single-digitizer, "quasi-quadrature" detection system that operated directly on the IF signal. An additional mixing stage was added to each receiver to produce a 25-kHz IF output. This IF output was digitized at 25 kHz using a pair of trigger pulses spaced one-fourth of a cycle, or 10  $\mu$ s, apart. Besides requiring fewer components, this approach eliminated the need for well-balanced, wide-dynamic range quadrature detectors and well-matched, separate digitizers for each quadrature channel. The 16-bit digitizer used provided 96-dB dynamic range and a 100-kHz maximum sampling rate.

Due to the quarter-cycle delay between sample times, this approach produces an exact quadrature representation of the signal in the limit as the IF bandwidth shrinks to zero. However, the error was expected to be small, and could be compensated for during data processing by resampling. The quasi-quadrature method amounts to multiplying the IF output signal,  $z(t)$ , whose analytic representation is

$$\begin{aligned} z(t) &= \Re \{f(t)e^{i\Omega t}\} \\ &= \Re \{[x(t) + iy(t)]e^{i\Omega t}\} \\ &= x(t) \cos \Omega t - y(t) \sin \Omega t, \end{aligned}$$

by a pair of offset pulse trains:

$$\begin{aligned} s_1(t) &= \sum_n \delta(t - n\tau) \\ s_2(t) &= \sum_n \delta(t - n\tau - \tau/4) \end{aligned}$$

This is equivalent to convolving the spectral representation of  $z(t)$  with

$$\begin{aligned} S_1(f) &= \frac{1}{\tau} \sum_m \delta\left(f - \frac{m}{\tau}\right) \quad \text{and} \\ S_2(f) &= \frac{1}{\tau} e^{-i\pi f\tau/2} \sum_m \delta\left(f - \frac{m}{\tau}\right) \end{aligned}$$

The "fundamental" alias arises from convolution with the  $m=\pm 1$  terms. Considering only these terms, we have

$$\begin{aligned}
s_1'(t) &= \frac{1}{\tau} \int_{-\infty}^{\infty} e^{i2\pi f t} \left[ \delta\left(f - \frac{1}{\tau}\right) + \delta\left(f + \frac{1}{\tau}\right) \right] df \\
&= \frac{1}{\tau} [e^{i2\pi/\tau} + e^{-i2\pi/\tau}] = \frac{2}{\tau} \cos(2\pi f_0 t) \quad \text{and} \\
s_2'(t) &= \frac{1}{\tau} \int_{-\infty}^{\infty} e^{i2\pi f(t - \tau/4)} \left[ \delta\left(f - \frac{1}{\tau}\right) + \delta\left(f + \frac{1}{\tau}\right) \right] df \\
&= \frac{1}{\tau} [e^{i2\pi f(t - \tau/4)} + e^{-i2\pi f(t - \tau/4)}] = \frac{2}{\tau} \sin(2\pi f_0 t)
\end{aligned}$$

Thus the "fundamental" components of the sampling waveforms have the proper cosine and sine forms that multiply the IF signal used to recover the quadrature components in the conventional fashion. The sampled I-Q quadrature components themselves are

$$\begin{aligned}
z_I(t) &= [x(t) \cos(2\pi f_0 t) - y(t) \sin(2\pi f_0 t)] \sum_{n=-\infty}^{\infty} \delta(t - n\tau) \quad \text{and} \\
z_Q(t) &= [x(t) \cos(2\pi f_0 t) - y(t) \sin(2\pi f_0 t)] \sum_{n=-\infty}^{\infty} \delta(t - n\tau - \tau/4)
\end{aligned}$$

Noting that at the sample times,  $t = n\tau$ ,  $\cos(2\pi f_0 t) = 1$ ,  $\sin(2\pi f_0 t) = 1$ , etc., we finally have

$$\begin{aligned}
z_I(t) &= x(t) \sum \delta(t - n\tau) \quad \text{and} \\
z_Q(t) &= y(t) \sum \delta(t - n\tau - \tau/4)
\end{aligned}$$

Although I-Q components are recovered by this quasi-quadrature sampling scheme, the quadrature component is sampled late. If the delay is small compared to the reciprocal of the signal bandwidth, any error will be small. For the experimental conditions,  $\tau/4 = 10\mu\text{s}$  and the reciprocal of the bandwidth is approximately (1/15 kHz), or 67  $\mu\text{s}$ , so the error is expected to be minimal. An "I-Q alignment" step was applied as part of the data processing, which consisted of delaying the in-phase sample by 5  $\mu\text{s}$  and advancing the quadrature sample by the same amount through linear interpolation. No significant change resulted from this step, which supports the expectation that any errors would be negligibly small.

### 3.2 Site/Noise Survey

A site survey including noise measurements was conducted prior to test fielding. Details of these measurements are described in Appendix D.

Comparable noise measurements were made at several California coastal locations as well. Figure 13 shows examples of the noise scans that typify all of the Kauai and California results. These are compared to the 50-dB CCIR prediction for the season and time of day of the measurements and to the expected man-made noise in a quiet, rural location in Germany. The background noise continuum corresponds to the *bottom envelope* of the noise scan traces and is produced by atmospheric noise, man-made unintentional noise, and the juxtaposition of myriad distant transmitters; the high spikes are due to strong, discrete transmitters. We note that both areas have similar predicted CCIR noise levels (in the range of 30 to 45 dB above kTB) for the time of day and season of the measurements [2, 3]. As would be expected, the measured levels are somewhat greater than the CCIR predictions.

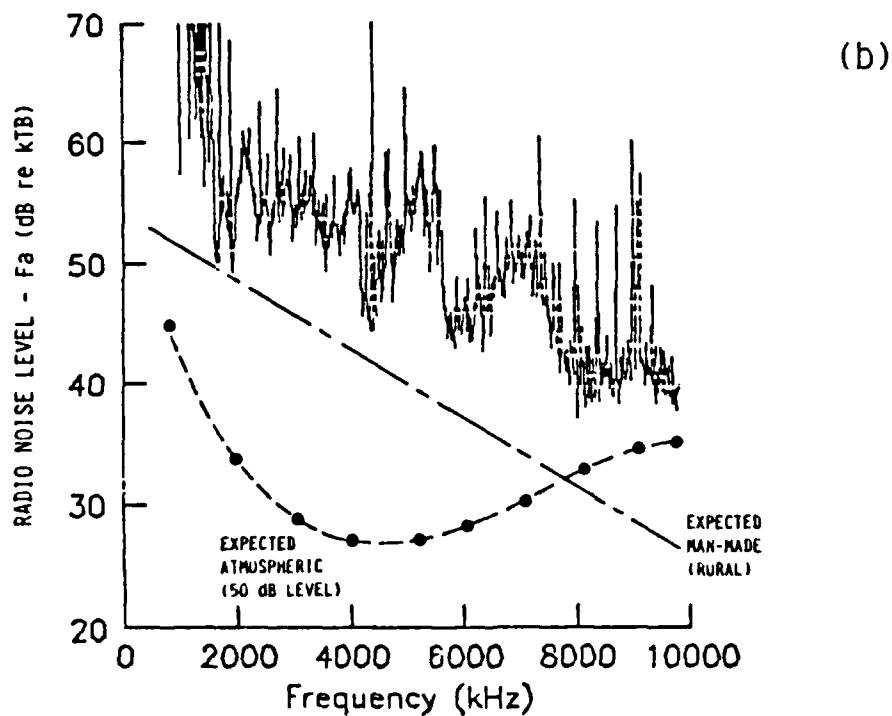
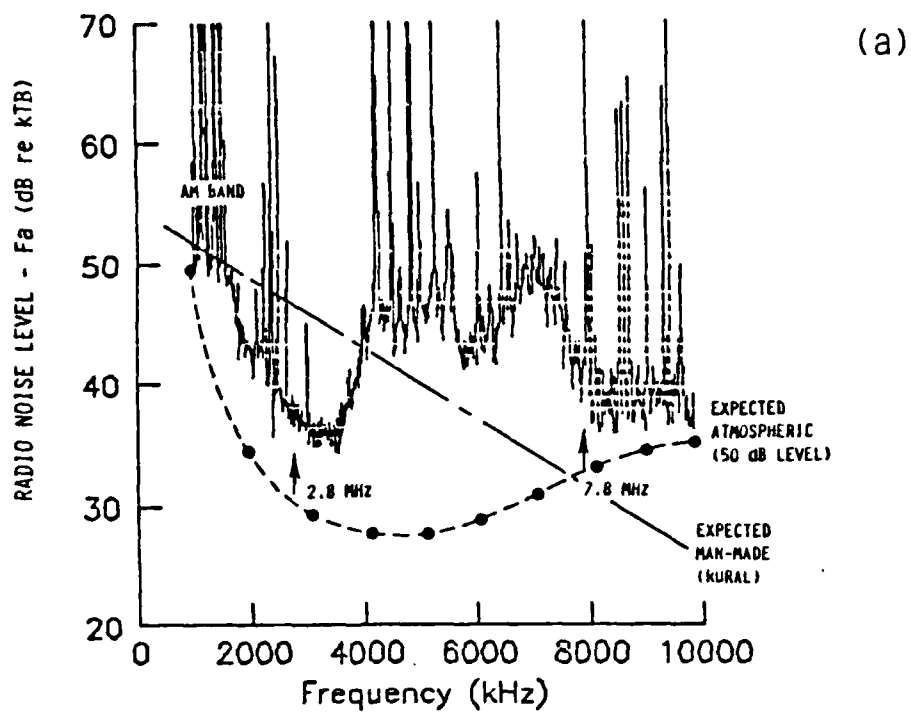


Figure 13. Examples of Noise Measurement at (a) Poipu Beach, Kauai, HI (2/7/88 1144 HST) and (b) Morro Beach, Los Angeles, CA (2/12/88 1206 PST).

The primary difference between the California and Kauai noise data is the pronounced dip below 5 MHz. This is the dominant Kauai feature. It is interpreted to be the effect of locally generated man-made noise filling in the spectral region below 5 MHz in California. Because of progressively lower antenna efficiency, below 3 MHz the external noise for some of the Hawaii data were so low that the internal receiver noise became dominant (the nominal and measured receiver noise figure was 19 dB).

Background noise from all sources is normally propagated for long distances by means of the ionospheric channel, which tends to become cut off at low frequencies during daytime. The atmospheric contribution arises primarily from three regions in the tropics where thunderstorm activity is strong and persistent; this contribution usually has to propagate long distances to be a factor. Locally generated noise propagates either by the space-wave (line-of-sight) or by the surface-wave conduit and would be expected to quickly die down with distance. The Kauai measurements evince the latter effects. Most of the man-made noise produced locally in the Hawaiian Islands should originate in the single major population center of Honolulu, which is well over the horizon (190 km) from the closest test site. In California, on the other hand, there would be much greater noise production due to the activities of a larger population and, especially for the Los Angeles-area measurement locations, no buffer due to distance from the interfering sources. Since the same receiver type was used for noise surveys and the SWOTHR tests, and the operating conditions were similar, the noise measurements are believed at least to be a fair representation of relative SWOTHR performance potential between the California and Hawaii sites.

There is always an issue in HF radar work concerning receiver dynamic range and spurious noise generation due nonlinear interactions in the presence of strong signals. This effect will increase the effective noise level across the band. Although the dynamic range of the receiver is not specified by the manufacturer, based on its design a dynamic range on the order of 90 dB is expected, which is just acceptable. Standard procedure was to set the receiver gain so that the peak of the direct signal was slightly compressed. There were no obvious noise-level increases due to nonlinear effects seen during the tests. With tuned receiver antennas at 2.8 and 7.8 MHz, experimentally the noise level was seen to be at least partly controlled by external sources because it could be lowered by attenuating the receiver input. This is consistent with the system operating noise figure calculations presented in Appendix B.

### 3.3 Software Development

*Signal Processing Flow.* Figure 14 illustrates the data processing flow. This consists of a series of sequential steps beginning with real-time quadrature digitization and data storage on a 120-MByte hard disk. Subsequent steps are then performed after the fact. First, individual receiver data are processed into range-Doppler frames. Then the frames are combined to form tracks in velocity-position space.

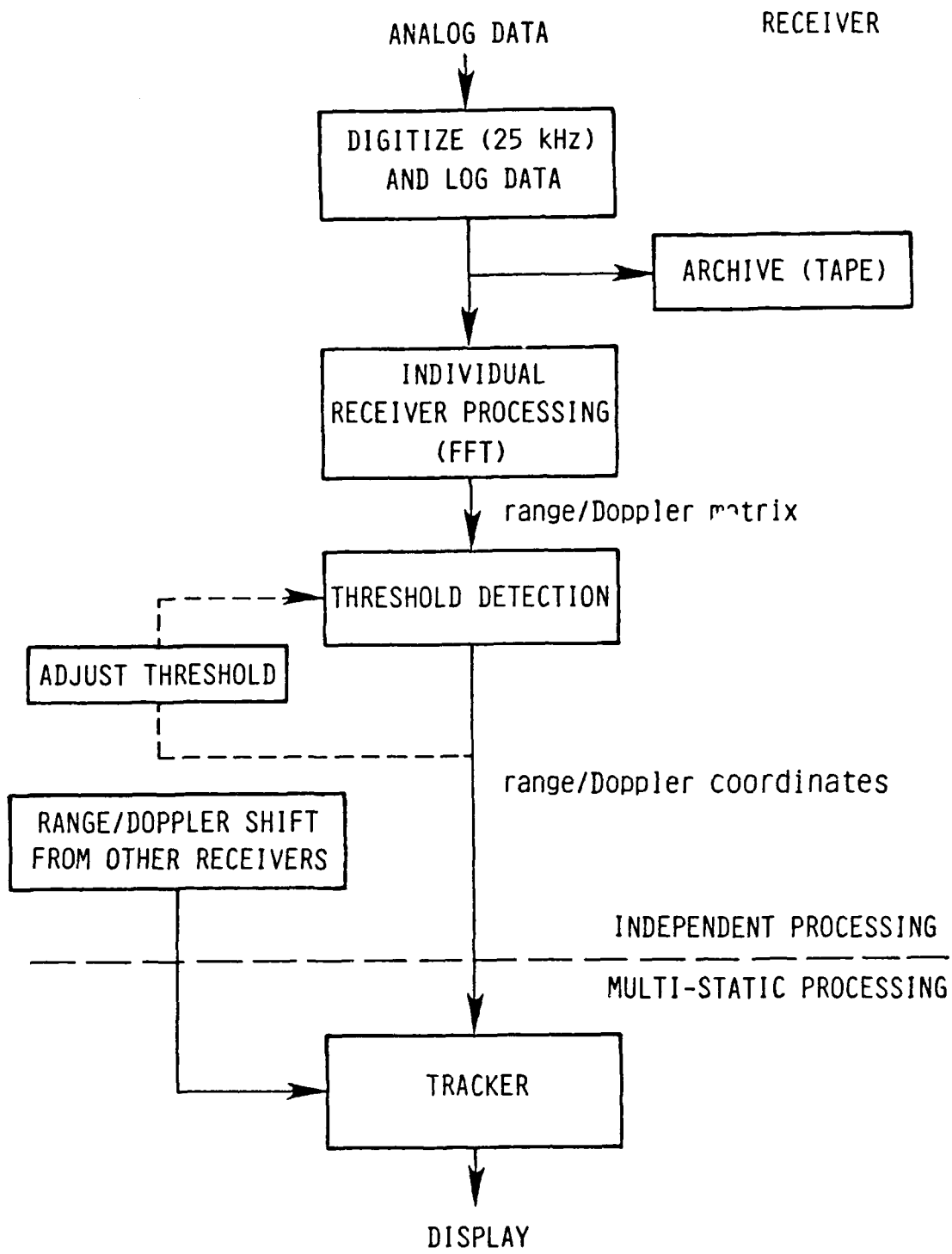


Figure 14. Data processing flow.

**Data-Acquisition Program.** This is based on the software supplied by Data Translation, Inc., with their DT2827 16-bit 100-kHz PC-based A/D cards. A shell program was written to record header information and control the digitizer subroutine. Once it was started, the digitizer effectively took control of the computer (e.g., it was not possible to interrupt the digitizer to read the clock). Logic-level signals generated internally by the receiver dictated the start of the digitization process and the subsequent sample commands, which consisted of bursts of 25-kHz pulse pairs.

Digitization continued until it was manually terminated or until storage space was exhausted. The digitized data were organized into sequentially numbered "raw-data" files containing 294,912 16-bit quadrature sample pairs. To maximize data storage, the data were packed together with no pulse identifiers or time tags, which was deemed acceptable because the strong direct signal was expected to be a steady and unambiguous timing reference (this expectation was borne out in all but one instance, where an average of one pulse in two seconds was lost when an operator mis-set the threshold trigger level). Normally, 32 range cells were digitized per transmitter pulse, which was a value preset by means of a switch within the modified receiver circuitry, so 9216 pulses were digitized per file. At a 390.625-Hz prf, which was used for most of the tests, a new file was written to the disk every 23.6 sec. A count of the files transferred to the disk was provided to the operator on the computer screen so that he could note the time and thus judge if the process was proceeding correctly (file-timing records are presented in Appendix D). Approximately 102 files could be stored on the hard disk.

**Individual-Receiver Signal Processing.** Originally, there were to be three steps to this processing: zero-shifting, downsampling, and range-Doppler spectral analysis. As described in Section 3.5, additional steps had to be added later to compensate for an unanticipated effect of the small offset between transmitter and receiver reference oscillators.

Zero-shifting was a process to eliminate the small offset between the transmitter and receiver reference oscillators and thus simulate phase-locking them together. It was accomplished by measuring the offset frequency of the low-level leakage signal from the transmitter (the transmitter was not completely turned off between pulses). A 4096-point FFT was made on data typically from Range Cell 28 at the beginning of each raw file and the location,  $f_o$ , of the peak determined. Then the entire file was multiplied by  $e^{-2\pi f_o}$ . This forces the quadrature-detected direct signal to dc by shifting the entire spectrum.

At HF there is usually a large difference between an acceptable prf (hundreds of Hz) and the highest Doppler frequency to be encountered (tens of Hz). At the 2.8- and 7.8-MHz operating frequencies chosen for this experiment, the maximum Doppler shifts are 4.3 and 12.0 Hz, for example. Downsampling can thus be used effectively to lower the Nyquist frequency and reduce the spectral processing computational load. Here, this was accomplished by merely sequentially averaging blocks of  $n$  pulses together; typically,  $n = 20$ .

The spectral processing used a standard vector FFT algorithm that transformed data in all (32) range cells simultaneously to produce a range-Doppler frame. A "Hanning" window (which is also known as a "raised-cosine" or "cosine-squared" window) was applied to the data before the FFT to suppress clutter sidelobes. Figure 15 shows the spectral response of this window, which was generated by feeding a numerically generated 1-Hz sinusoid directly into the spectral analysis subroutine. Numerical, round-off errors produced the noise floor, which is about 105 dB below the peak. This dynamic range is considerably larger than any clutter/noise ratio seen experimentally. The penalty for the low sidelobe level is a 3-dB SNR reduction. The coherent integration time is half the length of the overall duration of this window. Typically, a 1024-point FFT length has been chosen for this data processing, which corresponds to a 26-s coherent integration time, or roughly half the expected dwell time of the aircraft in a range cell (note that the target echo will actually span two or three range cells, which are spaced by 6 km). Twenty-five percent overlap between successive frames was employed to maximize data recovery, so a new range-Doppler frame was generated every 13 s.

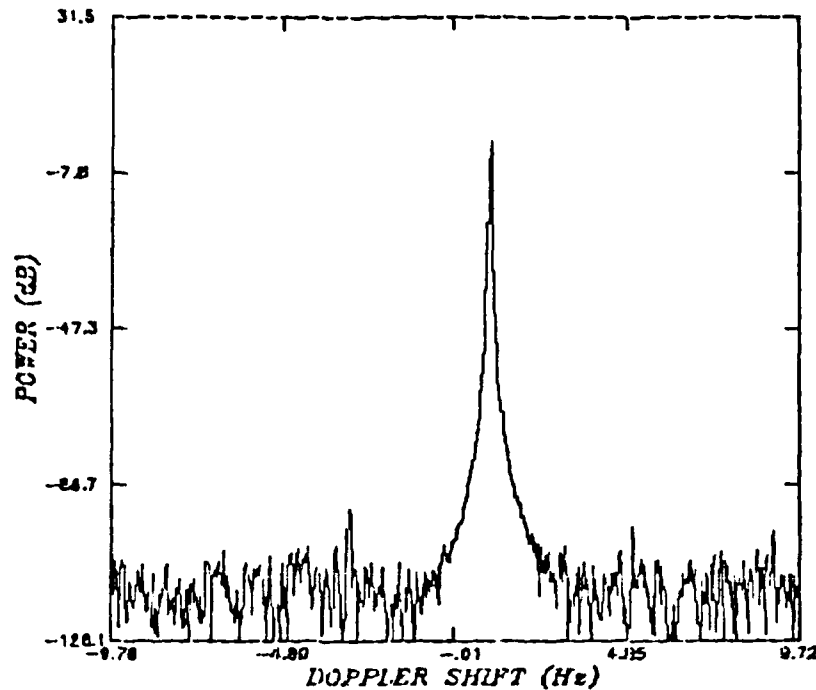


Figure 15. Spectral response function.

The sign of the observed Doppler shift in a system such as this depends on the details of the relationships between local oscillator and rf/IF frequencies, the way the quadrature detection is done, and the data processing, as well as on the relative velocity of the target. Analysis that included all of these factors predicted that a shortening of the round trip path length (i.e., a positive Doppler shift at the receiver input) would produce a positive shift at the output of the FFT processing. This was confirmed by direct measurement.

**Multistatic Tracker.** A two-receiver multistatic, multiple-target tracking (MTT) algorithm was developed and encoded for analyzing data collected from this experiment. This tracker incorporated the basic elements of an MTT system as shown in Figure 16 [8]. An MTT algorithm uses *gating* and *correlation* steps to associate new observations with established tracks or as candidates for starting new tracks, *track initiation*, *confirmation*, and *deletion* steps, and *filtering* to predict future target locations. Some steps may be combined, such as filtering and gating when Kalman filtering is used.

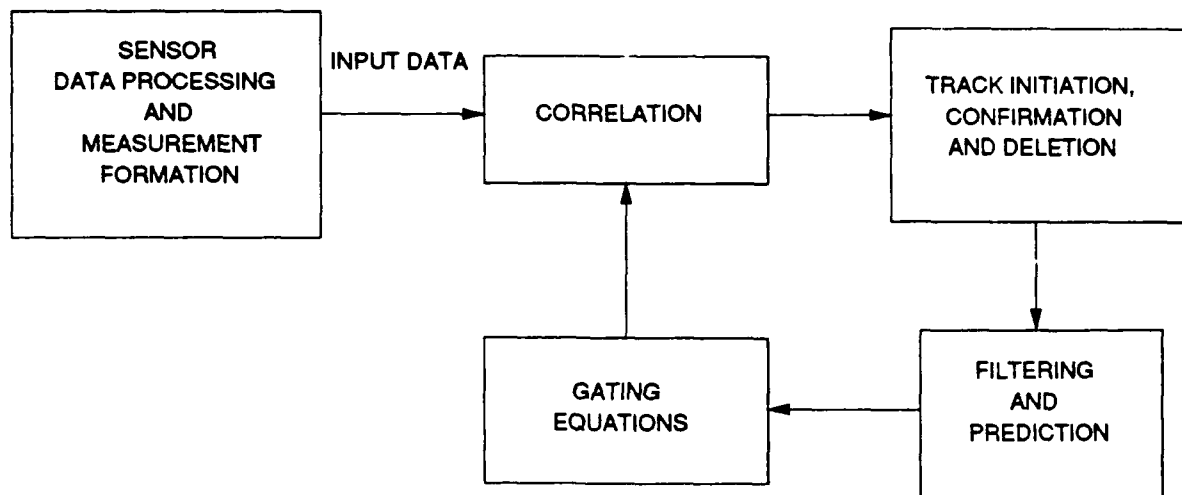


Figure 16. Basic elements of an MTT system.

Two filters were investigated. The first was a standard Kalman filter. This filter required good initial estimates of the target state vector and recovered slowly from bad initial estimates. Note that for the SWOTHR surveillance and track mission in general the (incoming) target SNR is lowest when the track is initiated and thus the initial estimates are likely to be the least reliable. The second was a covariance-weighted filter based on the first one. This filter overcame the deficiencies of the first one by more appropriately weighting the track parameters and input data.

Figure 17 presents some results from tests of the MTT using simulated data that compare the performances of the two filters. Three cases are presented. In all, the target is assumed to fly inward at a steady rate 300 m/s from a position 100 km west of the transmitter. The two receivers are taken to be 3 km east and 9.5 km north and south, respectively, of the transmitter. Range-dependent Gaussian noise has been added to the position and velocity-state components to simulate the uncertainty in target state estimation. Comparison 1 is a "high" SNR case where the initial estimate is based on a single "observation." Comparison 2 is the same as the first except that the initial estimate is based on several observations. This delayed the onset of the track as evident. Comparison 3 is a "low" SNR version of the second. The superiority of the covariance-weighted filter over the standard Kalman filter is obvious. Note that the tracker using the latter filter significantly improved the accuracy of target azimuth estimates.

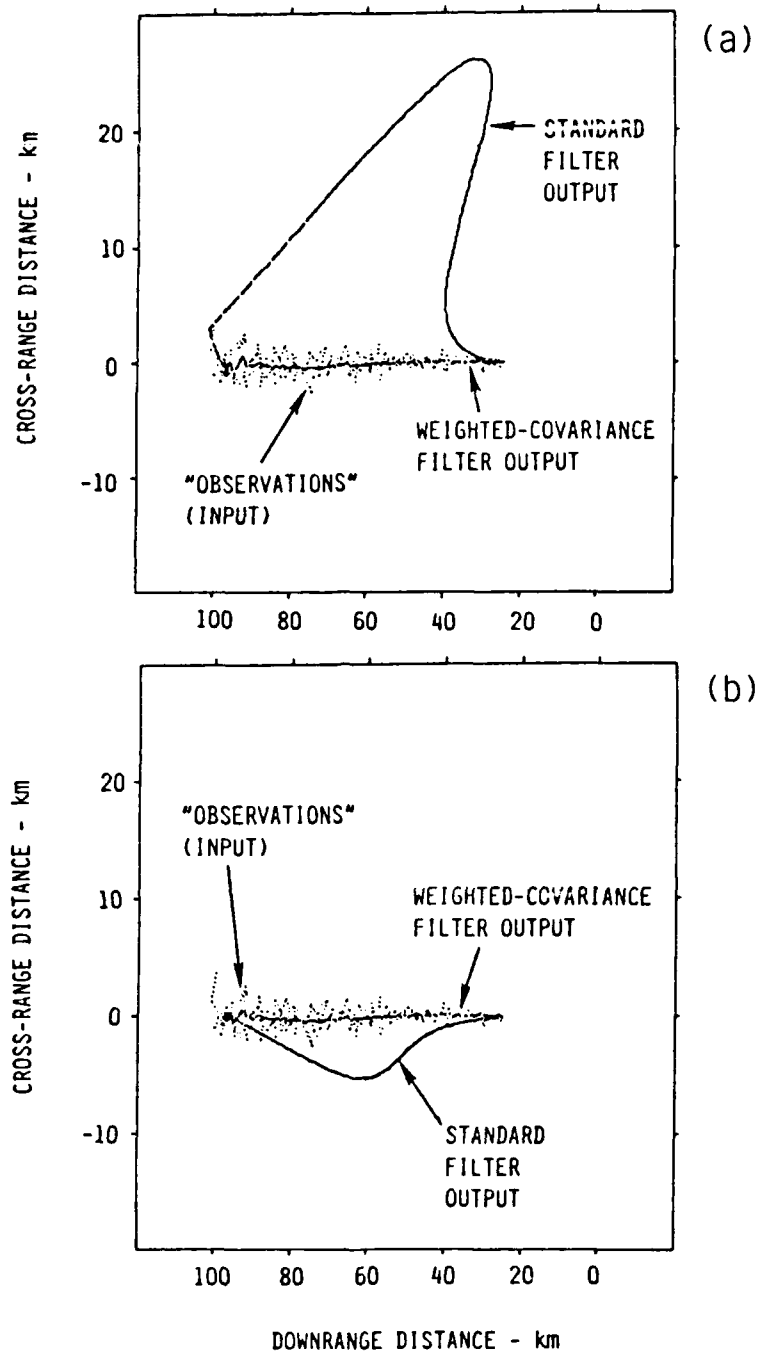


Figure 17. MTT filter comparisons. (a) Comparison 1. High SNR, single-observation initial estimate. (b) Comparison 2. High SNR, multiple-observation initial estimate. (c) Comparison 3. Low SNR, multiple-observation initial estimate.

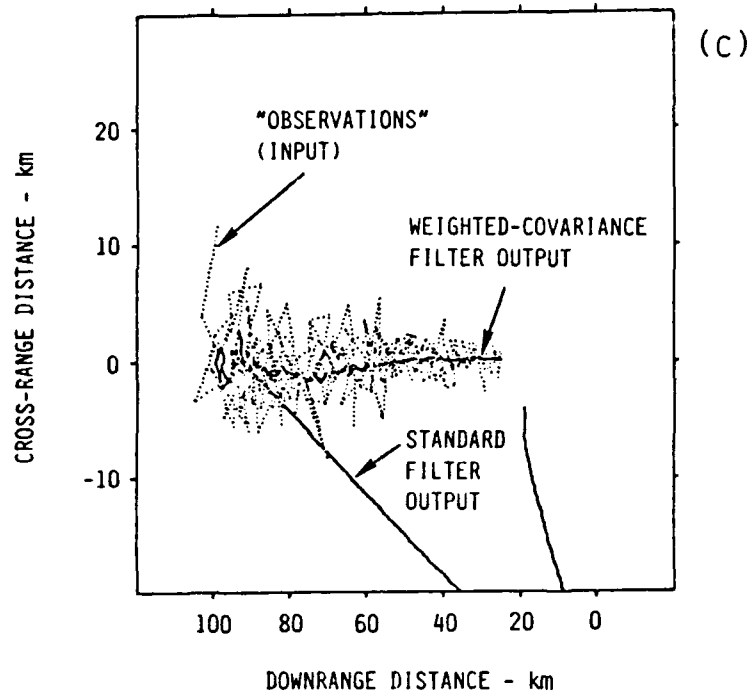


Figure 17 (concluded). MTT filter comparisons. (a) Comparison 1. High SNR, single-observation initial estimate. (b) Comparison 2. High SNR, multiple-observation initial estimate. (c) Comparison 3. Low SNR, multiple-observation initial estimate.

A somewhat more elaborate procedure than described above is actually employed by the multistatic MTT. The basic MTT filtering and tracking is first done in the range-Doppler space output of each receiver to establish tentative tracks. The input data are range-Doppler cell coordinates of signal intensity peaks that exceed a specified threshold. (We also investigated using the estimated coordinates of the centroid of the group of cells surrounding a peak to improve the data quality into the tracker, but this was difficult to implement reliably, and simulations showed that this approach produced no tracking improvement in the long run because the MTT itself took care of the granularity of the data---this may not be true for short-duration tracks, however.) Tentative tracks are also in those coordinates. Then a coordinate conversion is made to position-velocity space for the final track initiation, confirmation, and deletion steps. This procedure minimizes the number of coordinate transforms that

need to be performed, which yields a considerable savings because each transformation requires solving four second-order equations (for the reduced, two-receiver SWOTHR field test configuration). All possible matches between tentative tracks are considered.

*Supporting Software.* Standard graphical programs were adapted to permit displays of the intermediate and final outputs from the experiment. These included contour-, waterfall-, and 3-D surface-plotting capabilities.

### 3.4 Experiment Execution

Experiment fielding began in the last week of April, 1988. A series of three cooperative flight tests were completed on 12, 16, and 18 May, 1988. About 2.4 h of data were collected altogether, which tallied to 720 MBytes of raw data. No non-cooperative, targets-of-opportunity data runs were attempted due to the lack of appropriate targets. Appendix D is a synopsis of the flight test operations.

In spite of the abbreviated period available for setup and testing, this work proceeded relatively smoothly. The main logistical problems experienced were with setting up the 30-ft transmitting antennas and with inter-site communications. In retrospect, however, the aggressive schedule that we attempted to follow due to time and resource limitations did not provide quite enough time to shake out the equipment and procedures completely.

Part of the antenna design effort involved NEC-program calculations of the antenna field strengths and radiation efficiencies, for the low-conductivity coastal soil in Hawaii (Appendix B). These also provided predictions of the locations for the taps on the antenna tuning coils, which were found to be extremely accurate when the antennas were tuned up during the field effort. This agreement supports the validity of the antenna efficiency calculations, which were used in Table 2 and Figure 11. Echoes from Niihau Island could readily be observed on the oscilloscopes provided at each receiver. These were used to verify that the antenna arrays were correctly phased to form a beam out to sea.

Although our original intention was to process test data in between flight operations, this turned out to be impractical due to the long period of time required to permanently save the raw data on magnetic tape. Since the analysis routine itself was relatively slow, it was decided only to process enough data in the field to assure that the data-acquisition system was operating correctly.

Several significant problems were unearthed subsequent to test execution after the main data analysis effort began. One was an unanticipatedly large temporal slip between the received pulses and the digitization burst. This effect is related to the frequency offset between the transmitter and receiver reference sources. It can be avoided by phase-locking the receiver to the direct signal from the transmitter. A small amount of slip would have had a negligible effect. However, the slip magnitude experienced during the tests was large enough to shift the positions of the sample times by one cell typically every 20 to 40 s, which is significant compared to the coherent integration times used here (overall width of FFT transform weighting windows used in the analysis was typically 52 s). Discontinuities in the data stream occurred when the slip reached the sample interval, which artificially raised the noise level. It was possible to correct for this effect by resampling the data and realigning the pulses, but that entailed writing new computer code and slowed the data analysis effort. This is described in more detail in Section 3.5.

Another serious potential problem was a loss of sensitivity in one of the receivers that was traced to a burnout of the rf amplifier stage. It is not known when this occurred, and it was not uncovered during the fielding effort. The experiment procedure called for receiver calibration tests and checks for external-noise-limited operation to insure that the receiving antennas were correctly set up and connected. These field checks indicated that the receivers were operating correctly at the time, which is supported by measurements on fixed echoes (see Section 4.2). This loss of sensitivity could have led to internal-noise-limited operation of that receiver and a 10-dB loss of SNR. It has been forwarded as an explanation for the lack of detectable target echoes at the affected receiver site.

The close proximity of the WWVH transmitters to our transmitter also caused some problems. High voltages were induced in our transmitter array, which made it impossible to tune it using a normal method. A more complex but time-consuming alternative procedure was successfully employed. No interference from WWVH was identified in the receivers. However, WWVH may have been the cause of the receiver front end burnout, and may have induced subtle effects.

No sign of ionospherically propagated backscatter was seen at either operating frequency. At least at 2.8 MHz, this is consistent with the dip in the atmospheric noise level. A 244-Hz prf was picked for the first test flight, which corresponds to a 614-km unambiguous

range and permitted about 65 min of data storage. Because of the absence of detectable backscatter, a 390-Hz prf was chosen for the last two flights. Theoretically, the higher prf provides a 2-dB-higher SNR, but at the expense of limiting the test duration to 40 min.

### 3.5 Additional Data Processing Steps

Two additional major data processing steps were added after the field effort to the IRSP program: (1) resampling, and (2) pulse-alignment. These steps were needed to compensate for the slip produced by the frequency offsets between the transmitter and receiver master oscillators. Besides these, an "I-Q alignment" step was implemented, as was a special frequency-translation step to compensate for a 200-Hz mis-tuning of one of the receivers (#1) on one of the test days (5/16/88); this was easily accomplished by multiplying the complex receiver output by the appropriate complex exponential function (i.e.,  $\exp -i2\pi(200)t$ ).

*Description.* Both the transmitter carrier signal and the modulating waveform are derived from the stable oscillator in the HP-51 frequency synthesizer. All of the receiver local-oscillator signals and the 25-kHz digitizer sampling triggers are derived from the 9-MHz crystal-controlled master oscillator in the receiver. (Transmitter and receiver details are discussed in Appendix B.) After warmup, there was typically about a 1-ppm effective offset between these oscillators, which remained quite stable for extended periods of time (within hundredths of a Hertz for minutes). As described above, IRSP was designed to measure the offset frequency,  $f_o$ , and shift the receiver output spectrum as a whole so that the direct signal from the transmitter was at  $f=0$  Hz.

The small difference between the time bases produced a steadily progressing slip between the transmitted pulses and the digitizer trigger waveform as depicted in Figure 18. By itself, the slip was not thought to be a potential problem because it was not expected to be significant compared to the range-cell depth over planned coherent integration times. This turned out not to be true. Serious problems arose because the digitizer burst effectively jumped by one range cell when the slip grew to match the 40- $\mu$ s sample interval, after which either a "new" sample appeared at the beginning of the burst or the first one in the burst "disappeared." The digitizer gate was designed to produce a burst (nominally 32) of quadrature sample pairs starting with the pair following the threshold-exceedence on the leading edge of the direct pulse from the transmitter. Jitter in the start of the burst gate due to even the small amount of noise on the direct signal exacerbated the problem with the sampling discontinuities because it produced a period of back-and-forth jumps as shown in Figure 18. If there

were no random jumps, the position of the sample with respect to the transmitted pulse would have a regular sawtooth appearance. The effects of any of these range-cell jumps are to shorten the effective coherent integration time, which lowers the signal strength, and to introduce wideband noise due to discontinuities in the stronger, low-frequency-offset clutter and direct-transmitter signals. Although both effects reduce SNR, the latter is particularly troublesome. In order to avoid these problems it is necessary to furnish a continuous record from each range delay to the FFT processor.

The strongest manifestation of trouble was a high spectral sidelobe contamination level at shorter ranges occupied by the trailing edge of the direct signal from the transmitter and the fixed echo from Niihau Island. However, this problem often raised the effective background noise level unacceptably at all ranges because the continuously radiated residual direct signal could be affected by the range-jump discontinuities.

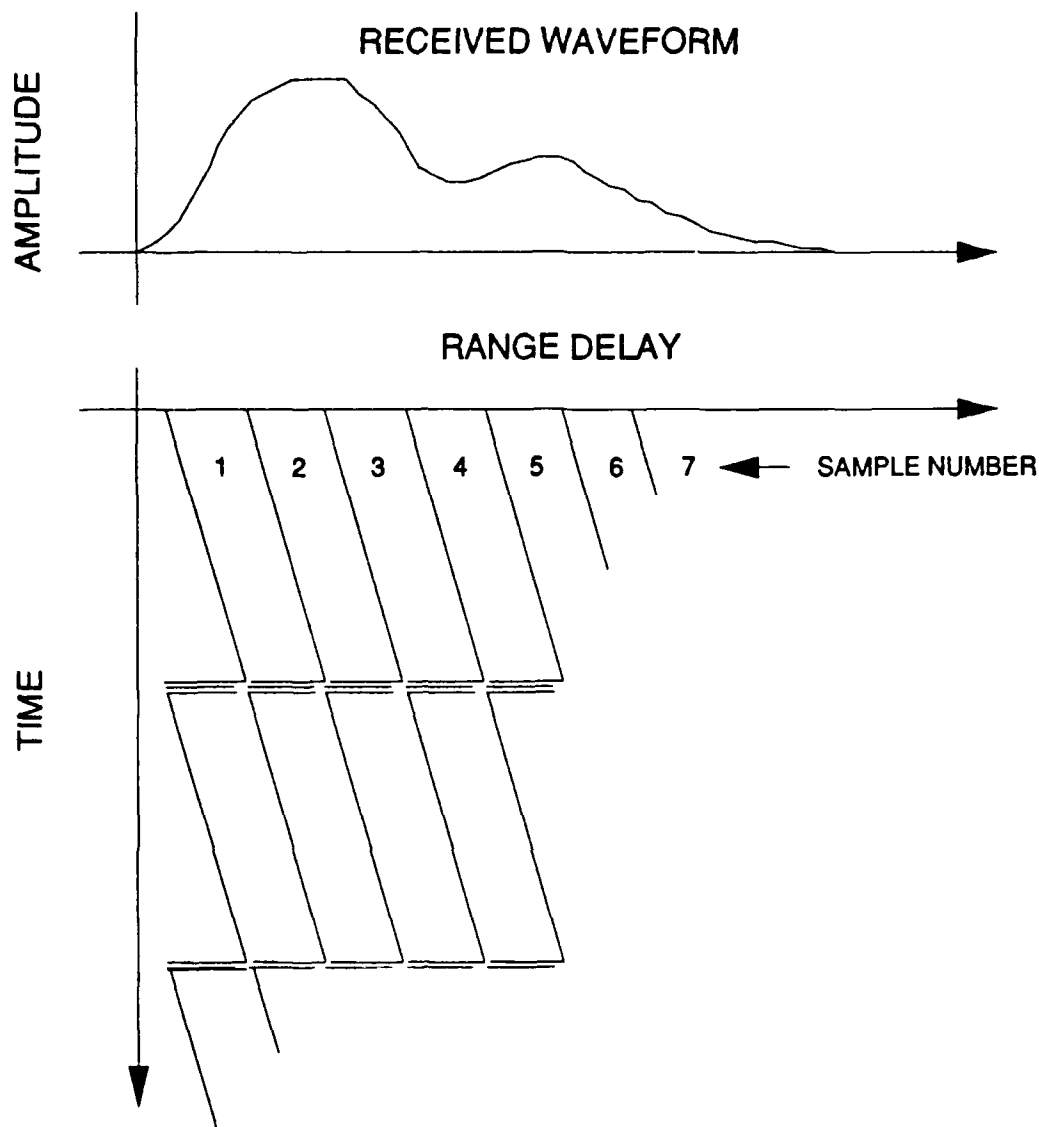


Figure 18. Sample positions relative to the received pulses versus time.

**Resampling and Pulse Alignment.** A continuous record can be generated by resampling each pulse in the range direction and then aligning them to get rid of the jumps. Resampling is best accomplished by linear interpolation between the original samples. The position of the interpolated points is proportional to the offset frequency, which was already being measured in IRSP in order to remove it. In effect, the interpolation locations have the appearance of another smooth sawtooth, but of the opposite sign as the original slip.

The amount of slip per pulse is given by the following formula:

$$\delta t = \frac{f_o \times 10^{-6}}{\text{prf} \times f_r} \text{ s}$$

where  $f_r$  is the operating frequency in MHz. For example, if  $f_o$  is -3.4 Hz (which is a value measured during one of the runs) at  $f_r = 2.8$  MHz and a prf of 390 Hz,  $\delta t = -3.11$  ns. In this case, it will take about 32.9 seconds, or 12,860 pulses, to slip by one 40- $\mu$ s sample interval.

Several interpolation schemes were tried. None produced better performance than simple linear interpolation based on the calculated slip. The slip rate was calculated by estimating the frequency offset,  $f_o$ , for each data file, and was thus updated every 10 to 20 s, depending on the prf. Typically, the offset frequency was stable to within 0.02 Hz for several minutes.

An additional linear interpolation step was also used to time-align the quasi-quadrature samples by respectively delaying the in-phase and advancing the quadrature sample by 1/8 of the 40- $\mu$ s sample interval. Tests with and without this extra step showed that resampling produced little change, which confirmed that the quasi-quadrature sampling technique worked adequate. Although it was therefore not really necessary, this processing step was included because it was trivial to implement as part of the slip-compensation algorithm.

Substantial improvements in the effective background noise level were obtained with these fixes. Although spectral sidelobes were still present above the background noise at short ranges, they were driven down to the random noise level at ranges beyond the echoes from Niihau Island. This has permitted target detection at longer, over-the-horizon ranges. The high sidelobe level continues to preclude target detection at short ranges. Since it is not certain that the artifacts have been totally removed, it may be possible to achieve further, modest improvement.

## 4 Test Results

### 4.1 Target Detection

*Range-Doppler Plots.* Figure 19 presents a sequence of contour plots of the *magnitude* of the range-Doppler processor outputs that show the progress of the target during its first inbound pass on the 2.8-MHz operation conducted on 16 May 1988 (Appendix D provides details of that test). The contour interval was 50 units. A 52-s window was used to generate these frames, which corresponds to a 26-s coherent integration time and a 13-s interval between frames. The spectral resolution was 0.019 Hz, which translates to 2 kn. The frame times listed in Figure 19 refer to the center of the window.

These results are for Receiver 1, which was located at the Hoku Rd., or North, site. Because the aircraft track was nearly in line with both the transmitter and Receiver 1, its range-Doppler trajectory is virtually at constant Doppler shift. Thus a velocity scale can be added to the Doppler axis, as has been done in Figure 19. The aircraft's ground speed was reasonably close to the expected, nominal 450-kn indicated airspeed.

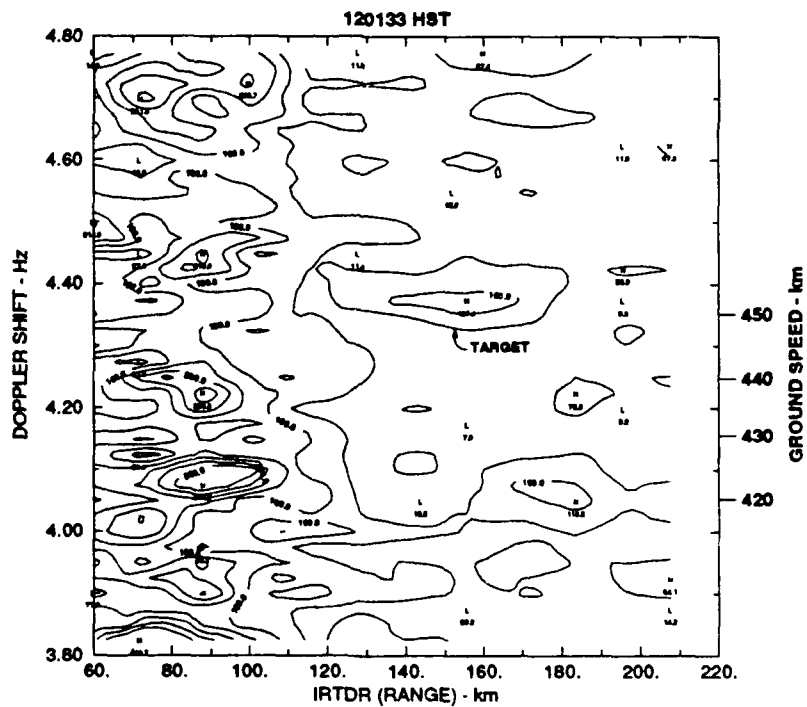
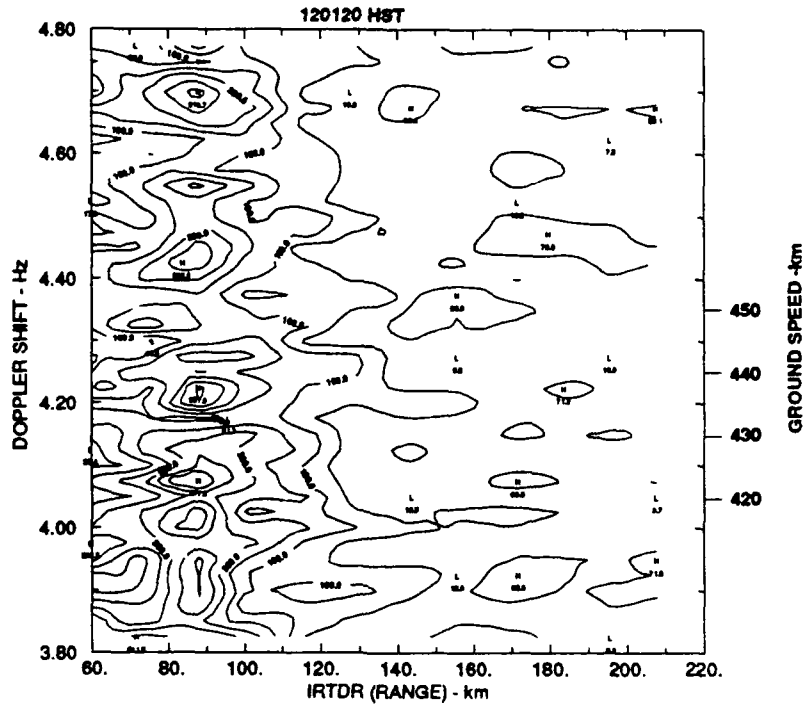


Figure 19. Range-Doppler frames, first inbound pass, Receiver 1, 5/16/88 Test.

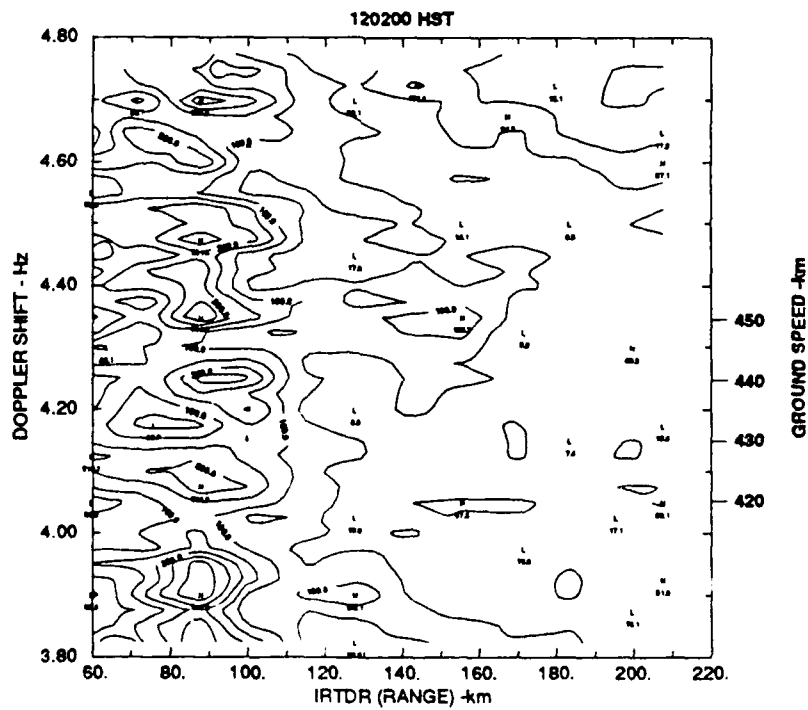
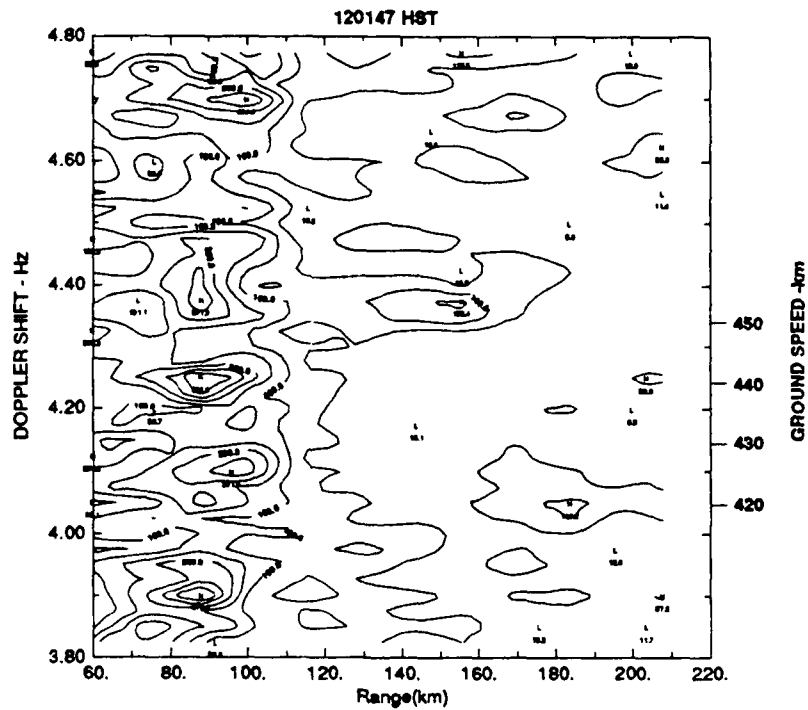


Figure 19 (continued). Range-Doppler frames, first inbound pass, Receiver 1, 5/16/88 Test.

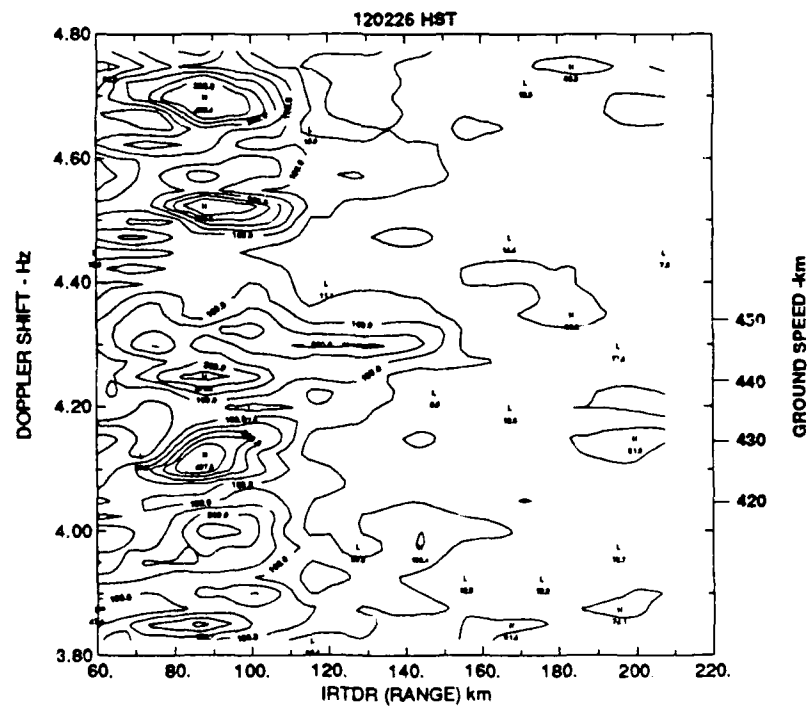
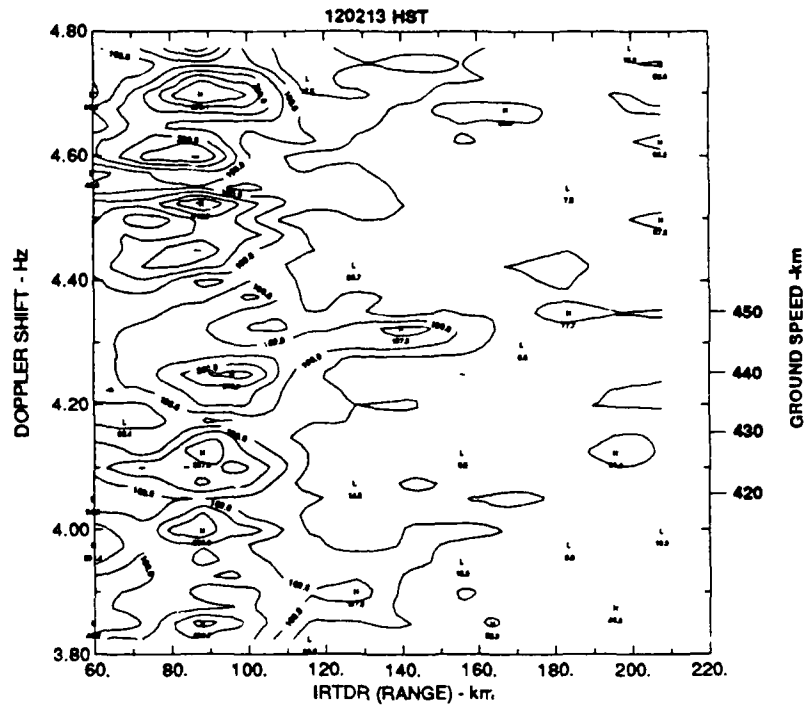


Figure 19 (continued). Range-Doppler frames, first inbound pass, Receiver 1, 5/16/88 Test.

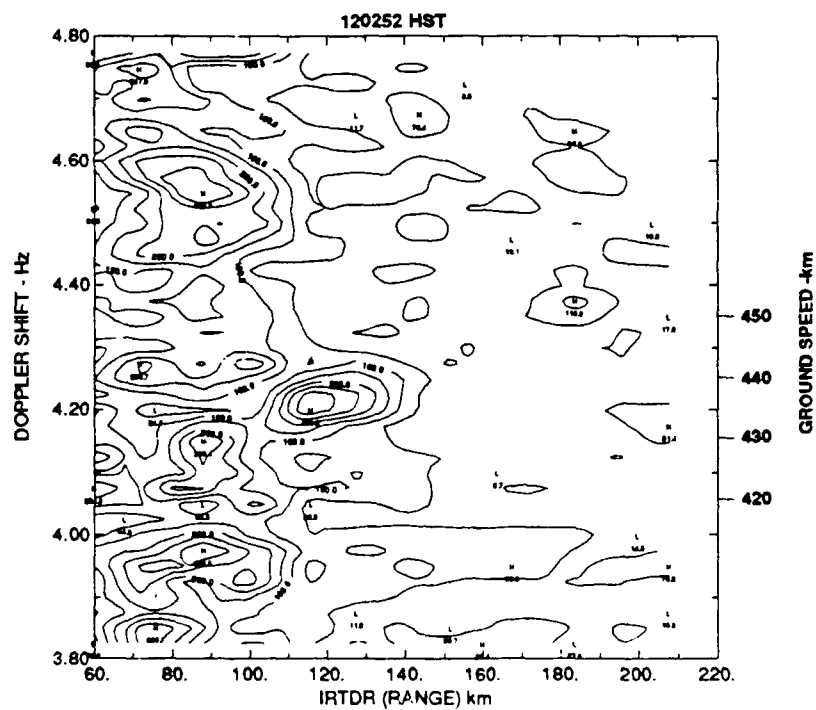
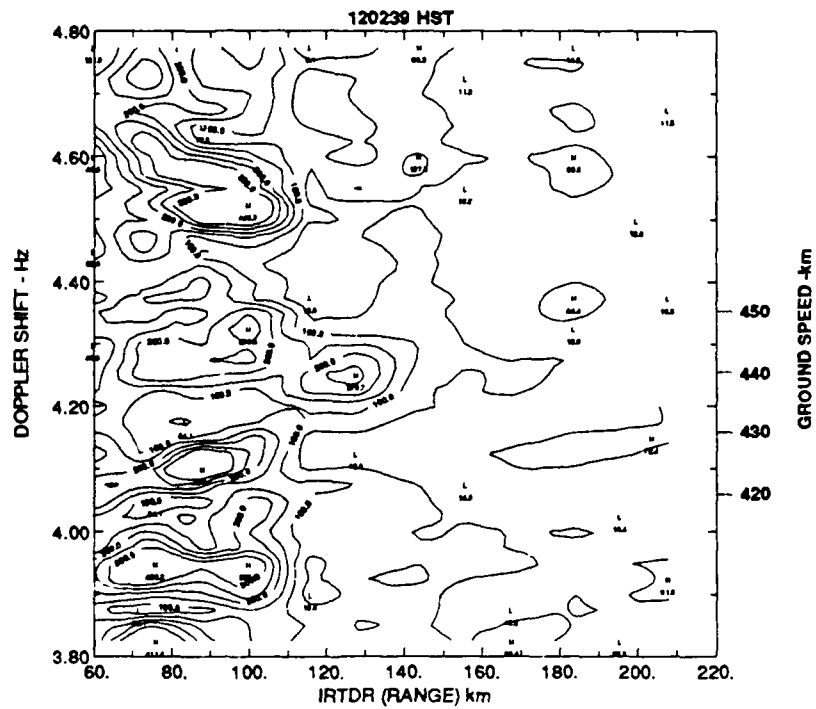


Figure 19 (continued). Range-Doppler frames, first inbound pass, Receiver 1, 5/16/88 Test.

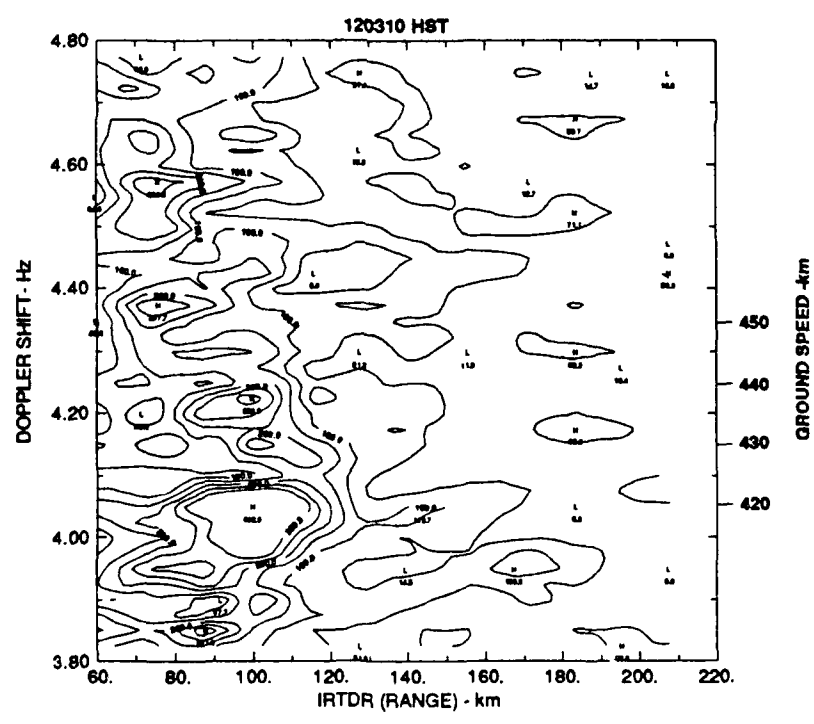
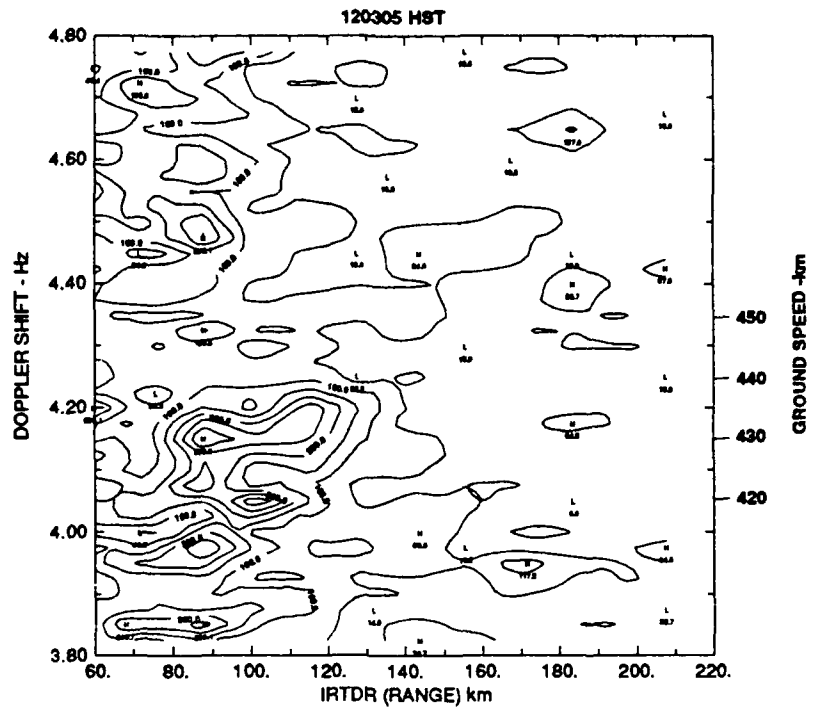


Figure 19 (concluded). Range-Doppler frames, first inbound pass, Receiver 1, 5/16/88 Test.

In range-Doppler plots such as those in Figure 19, the "range" scale is actually the time-difference-of-arrival between the direct pulse and an echo, expressed as a distance, or the "round-trip differential range." At ranges much greater than receiver-transmitter separation, this is about twice the distance from the target to the centroid of the receiver and transmitter. Precise range registration is obtained from the location of the fixed echo from Niihau Island, which falls at an indicated range of 84 km in the Figure 19 frames. From the charts, the true range difference is 60 km, or four digitizer range cells closer than in the range-Doppler frames. The discrepancy is an artifact due to combined effects of the trigger level of the digitizer burst gate, which occurs ahead of the peak, and permanent shifts caused by the jump-alignment algorithm. In Figure 19, then, the target will be over the horizon from Receiver 1 at 94-km indicated round-trip differential range (IRTDR) and over the horizon for both Receiver 1 and the transmitter at 109-km IRTDR.

Figure 19 includes all of the frames from somewhat before the target is distinct until it disappears into the confusion of the sidelobes of the echo from Niihau Island and the trailing edge of the direct signal. It is persistent in the second through seventh frames (Figures 19 (b) through 19 (h)), starting at 154-km IRTDR and ending at 114-km IRTDR. *Thus the target is over the horizon from both transmitter and receiver sites for this entire sequence.* At 450 kn (243 m/s), it would take the target 85 s, or six and one-half 13-s frames, to change its IRTDR by 40 km, which is consistent with observation. A plot of the target IRTDR versus time appears in Figure 20. Shown are the IRTDRs of the cells that produced the highest echo strengths and the span of the highest contour intervals surrounding those peaks. These target positions compare well with the 450-kn trajectory.

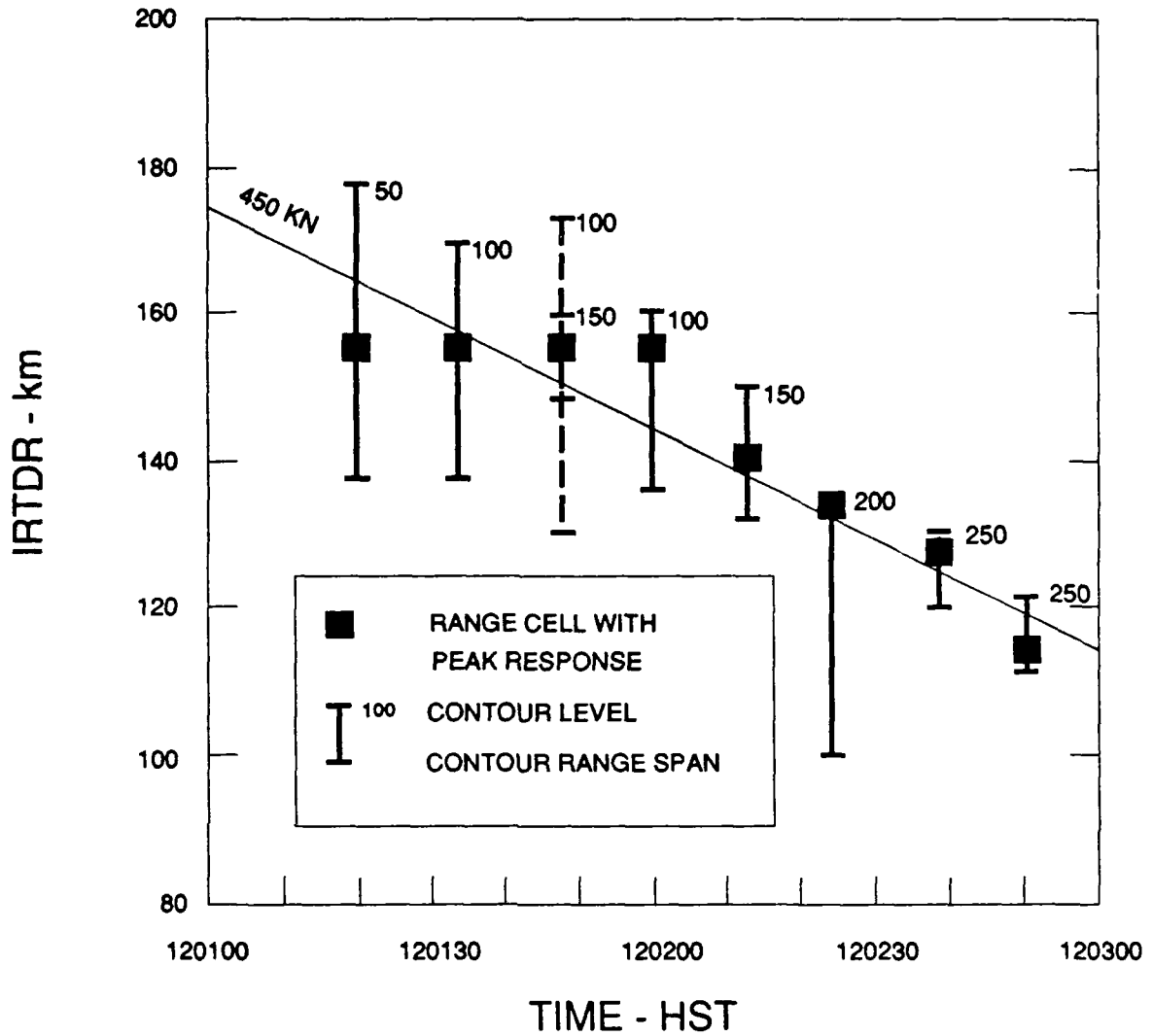


Figure 20. Target IRTDR vs. time.

The ground speed of aircraft apparently slowed by nearly 20 kn (4%) during this interval, with the greatest deceleration toward the end. This may have been due to a change in the wind field with location relative to the islands, a change in the airspeed or heading, or both. We note that the pilot began to receive TACAN navigational signals from Barking Sands toward the end of the interval as the airplane came over the horizon and that he may have adjusted his heading and airspeed either to get back on course or in preparation for the

upcoming turn. This is significant because a change of velocity will cause a spread in Doppler shift and prevent attaining the full theoretical coherent integration time. It appears that the Doppler spread of the target has widened significantly by the end of the sequence.

**SNR and Noise Level.** The SNR can be estimated from Figure 19 by comparing the peak level to the background noise level. The latter quantity is obtained by computing the mean level of the magnitude of the signal in a portion of the range-Doppler frame free of clutter sidelobes and spurious receiver responses. The ratio of the standard deviation to mean level should be unity for a spectral estimate of random noise. From frame to frame, the measured ratio in 5/16/88 Receiver 1 data typically ranges between 0.97 to 1.07 units, which is thus consistent with expectations. The mean detected noise magnitude and its standard deviation were approximately 40 units for this data set, so the noise power was 1600 units<sup>2</sup>.

Table 3 summarizes the SNR estimates derived from Figure 19. The IRTDR and transmitter-target range are estimates based on the linear, 450-kn trajectory plotted in Figure 20. The SNR versus range estimates are compared in Figure 21 to the 2.8-MHz prediction for conditions essentially the same as that of Figure 11(a). There is good agreement between prediction and observation.

Table 3. SNR vs. Estimated Range

Frame Time (HST)	IRTDR (km)	Target Transmitter Range (km)	$\sqrt{(S + N)_p}$	SNR (dB)
12:01:20	162	69.5	81	4.9
12:01:33	156	66.5	137	10.3
12:01:47	149	63.0	155	11.5
12:02:00	143	60.0	136	10.2
12:02:13	136	56.5	168	12.2
12:02:26	130	53.5	200	13.8
12:02:39	124	50.5	271	16.5
12:02:52	117	47.0	340	18.5

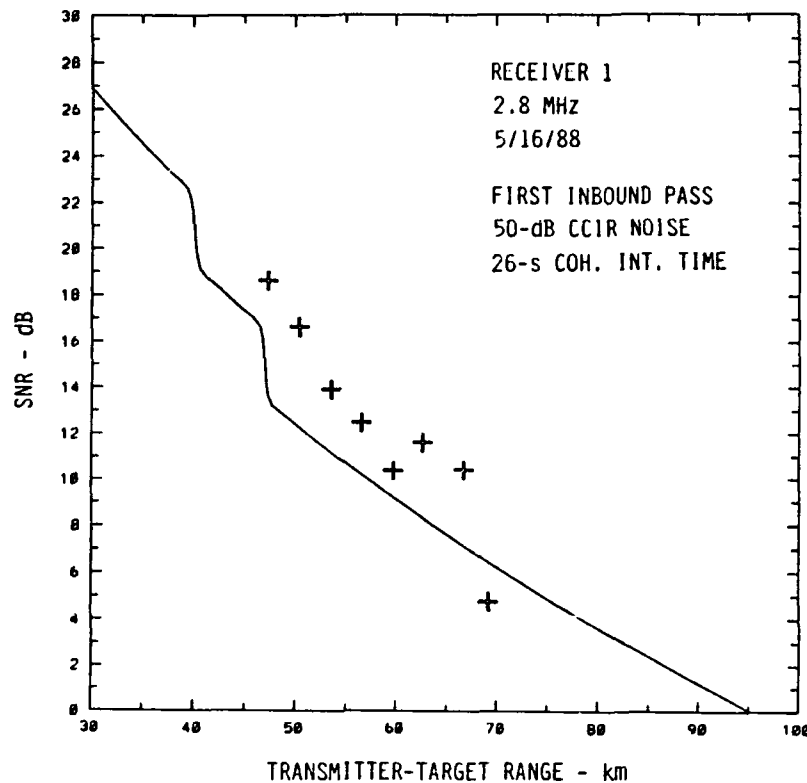


Figure 21. Comparison between the measured SNR and a prediction.

For the corresponding Receiver 2 data, the mean and standard deviations of the magnitude of the noise level were about 21 and 12 units, respectively. Thus the ratio of the standard deviation of the spectral variability to its mean is half that expected. This indicates that there was likely some residual contamination from sidelobe leakage that was not compensated for completely by the additional data processing. Leakage would be expected to be less variable than noise. Thus there is a possibility that some added improvement may be achievable with further data-processing efforts on the Receiver 2 data set.

#### 4.2 Fixed Echoes and Sea Clutter

High clutter-to-signal ratios due to echoes from land masses and sea scatter characterize this radar environment. Figure 22 shows a typical example of the signals in the low-Doppler region. Figure 22(a) is a range-Doppler contour plot and (b) is a slice at 162 km IRTDR from a frame in the same data set as discussed in the previous section. A 6-dB contour interval was used for Figure 22(a). Prominent features in Figure 22 are the two Bragg ocean-scatter lines at  $\pm 0.17$  Hz and the peak due to the residual CW transmitter signal

at zero frequency. The large peak centered at 78 km is the echo from Niihau Island (the peak here is at 78 km IRTDR rather than 84 km due to a slightly different processing procedure). More than half of the part of Niihau facing the experiment sites on Kauai is a 1000-ft high *pali* rising from the ocean (Figure 10). This cliff should be an exceptionally large HF scatterer (also, most of it is above the horizon). The Niihau echo strength at Receiver 1 was  $1.0 \times 10^6$  units, so its SNR was 88 dB. This is only a few dB less than the direct signal (which had to traverse a shorter path, but over lossier, low-conductivity soil). Trailing the fixed echoes from Niihau are range sidelobes resulting from the receiver time response (c.f., Appendix B).

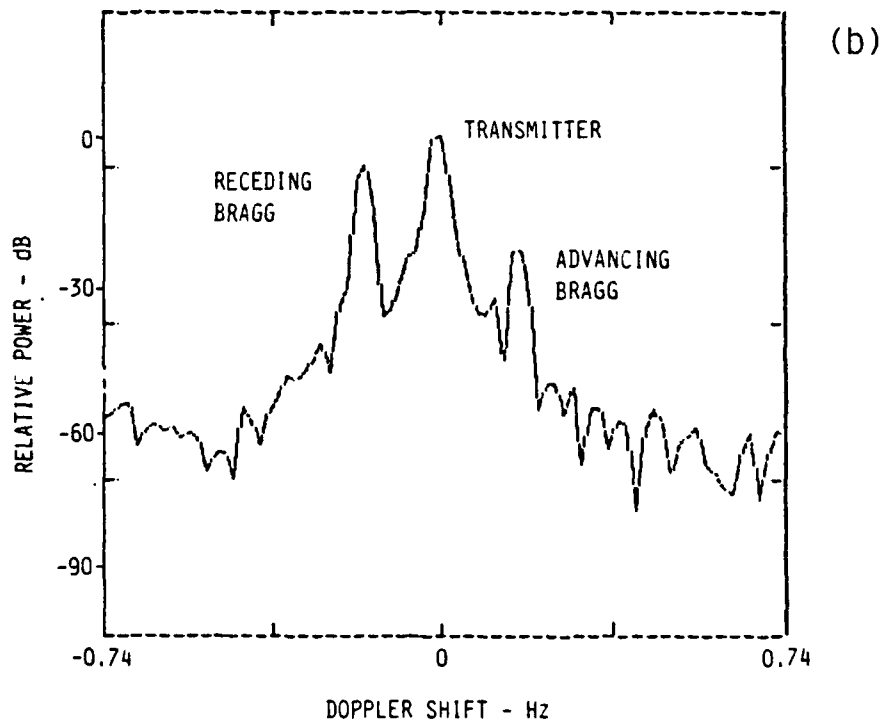
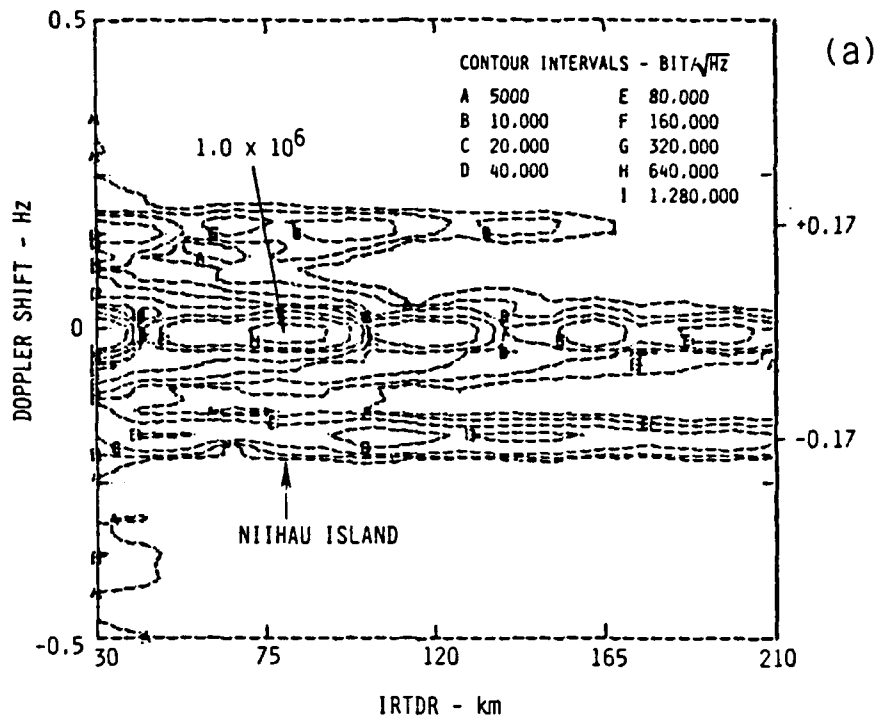


Figure 22. Clutter examples, Receiver 1, 5/16/88, 120213 HST frame; (a) range-Doppler contour plot, (b) spectrum at 162-km IRTDR.

A plot of the spectrum from -8 to +8 Hz at 114 km IRTDR for this frame appears in Figure 23. This was computed from the downsampled data, so the actual spectral width spans  $\pm \frac{1}{2} 390/20 = \pm 9.75$  Hz. The several spurs are artifacts consisting of harmonics (sometimes aliased) of the receiver offset frequency and of a residual "dc" component that has been shifted away from zero in the data processing. None of these spurs fell at frequencies where they interfered with target echoes. However, they do represent a potential problem, which can be eliminated by phase-locking the receiver to the transmitter.

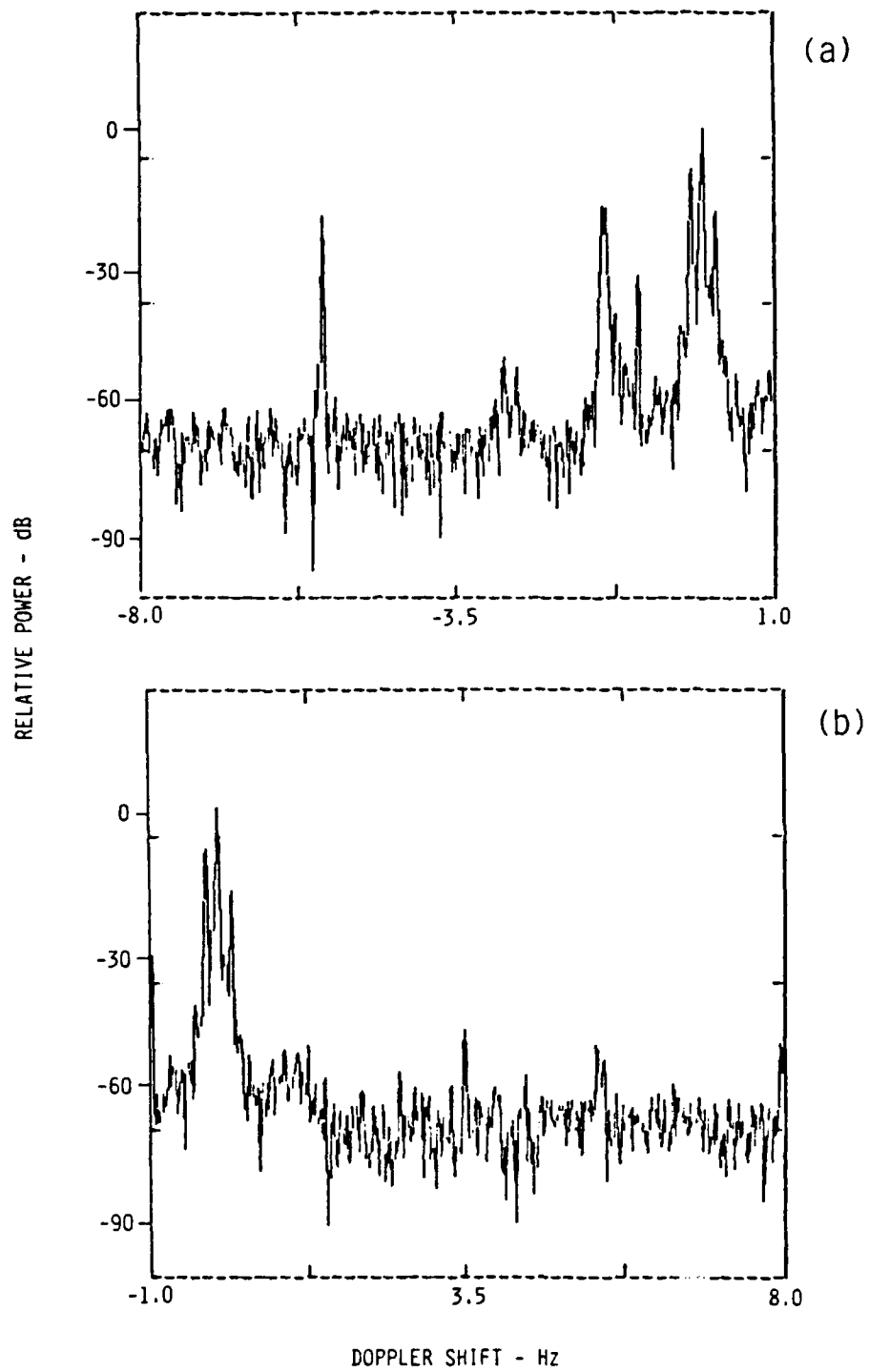


Figure 23. Spectrum from -8 to +8 Hz at 114-km IRTDR (a) negative side; (b) positive side.

### 4.3 Receiver 2 Target Detection

It has not yet been possible to identify target echoes in the Receiver 2 output. This is puzzling because both receivers produced the essentially same SNR for the fixed echoes from Niihau Island, and the target was readily visible in Receiver 1. Furthermore, Figure 11 predicts that the Receiver 2 signal will be somewhat larger than for Receiver 1 for the longer transmitter-target ranges.

A relative performance check can be made by comparing SNRs of the echoes from Niihau Island at the two receivers. If external-noise-limited operation is achieved, these can differ only because of differences in lengths of the paths from Niihau to the receivers, in the directional properties of the scattered signal and receiving antennas, or in the noise level. The path lengths were 33 and 49 km, respectively, from Niihau to Receivers 1 and 2, which would produce a 3.4-dB difference under space-wave propagation conditions. The scattered signal strength can reasonably be assumed to be the same in the two receiver directions due to the relatively small and similar-magnitude scattering angles. Wide-beamwidth antennas were used. The receiver sites were close enough together to experience the same ambient noise level. Table 4 compares the SNRs as measured for the Niihau Island echoes and as corrected for the path-length difference (note that the Receiver 2 noise level is based on the standard deviation of the noise floor, not its mean level). Very good agreement is obtained between the range-corrected SNRs. This, plus the good agreement between predicted and measured target SNR at Receiver 2, supports a conclusion that nearly equal performance and correct, external-noise-limited operation were experienced at both receiver sites during the 5/16/88 test.

Table 4. SNRs of Echoes from Niihau Island

	Receiver 1	Receiver 2	Units
Echo Magnitude	$1.0 \times 10^6$	$2.2 \times 10^5$	bits/ $\sqrt{\text{Hz}}$
Noise Level	40	12	bits/ $\sqrt{\text{Hz}}$
SNR (raw)	88.0	85.3	dB
SNR (range-corrected)	88.0	88.7	dB

Thus there does not appear to have been a loss of sensitivity due to Receiver 2 burnout at that time. Later measurements showed that main effect of the burnout was to raise the receiver noise figure from 19 dB to about 30 dB. Making the system operating noise figure calculation as in Appendix B, but with  $f_n = 30$  dB, we get  $f = 47$  dB. This would have produced internal-noise-limited operation and a large discrepancy between the SNRs of the Niihau echoes. This is contrary to observations made in the field during the receiver operation checks that were occasionally made. However, there remains some uncertainty because, inadvertently, receiver calibration data were not consistently recorded and thus performance cannot be precisely quantified with respect to absolute, known levels.

A possible explanation for the lack of target indications in Receiver 2 is that background-noise-limited operation was not attained in the region of the range-Doppler field where the target should be. However, there is no real evidence that the noise field was any different there from the region where the background level was estimated. An FFT processing artifact is unlikely because Figure 15 shows that the sidelobes of the spectral processing window were well below the contamination level. The only unusual factor in the Receiver 2 output was the discrepancy between the standard deviation and the mean level of the noise, but the discrepancy apparently occurred over all of the range-Doppler field that is free of visible spurs and obvious sidelobe contamination. Furthermore, it persisted for at least tens of minutes at the same level, and was thus unlikely to have been due to impulses. It may have been an effect due to leakage from the nearby WWHV transmitters.

Another difficulty for Receiver 2 was that there was a relatively narrow gap between the range at which the target could be detected and where it should disappear into the contaminating Doppler sidelobes of the Niihau Island echoes. The first three columns in Table 5 list the IRTDR and transmitter-target ranges derived from the target track for Receiver 1 and the offset of the target range from Niihau Island for the first inbound pass on the 5/16/88 test. The final three columns list the corresponding target-Receiver 2 range, IRTDR, and offset. All ranges are in kilometers. For Receiver 1 the target could be seen in all eight frames, but for Receiver 2, it would encounter the Niihau Island interference after four frames. In retrospect, this problem could have been minimized, and the range windows for both receivers opened up, by shifting the flight path to the west from the 180° to the 220° radial (Figure 10).

Table 5. Ranges (in Kilometers) for Receivers 1 and 2

Time (HST)	Receiver 1			Receiver 2		
	IRTDR	R <sub>TX</sub>	Offset	R <sub>Rx2</sub>	IRTDR	Offset
12:01:20	162.0	69.5	78	66.0	115.5	53.5
12:01:33	156.0	66.5	72	63.5	110.0	48.0
12:01:47	149.0	63.0	65	60.0	103.0	41.0
12:02:00	143.0	60.0	59	57.5	97.5	35.5
12:02:13	136.0	56.5	52	54.0	90.5	28.5
12:02:26	130.0	53.5	46	51.0	84.5	22.5
12:02:39	124.0	50.5	40	48.5	79.0	17.0
12:02:52	117.0	47.0	33	45.0	72.0	10.0

Further improvement in the unwanted Doppler sidelobe level may be possible, depending on its source. If they are due to jump discontinuities that have not been caught by the present pulse-alignment algorithm, improvement is possible. Note that even a one-sample gap in the 1024-point FFT of a uniform-magnitude signal, such as the complex signal representation of a sinusoid, will lead to a -60 dB "noise" level. In comparison, the unwanted sidelobe level in the processed output data is still on the order of 70 dB below the Niihau Island peak for both receivers. If the high unwanted sidelobes are due to receiver nonlinearities or instabilities, on the other hand, there is probably little that can be done. The sidelobe contamination level tends to track its source, however, which argues that jumps or discontinuities are the sources, so there is a reasonable expectation that processing can produce further improvement and permit multistatic tracking.



## 5 Conclusion

A basic, simplified experiment was fielded to verify and demonstrate several SWOTHR concepts. It was successful in meeting many objectives. A low-cross-section (-15 dBsm) target was detected at over-the-horizon ranges by means of surface-wave propagation. Radar operation at frequencies below the HF band was demonstrated. Detected signal-to-noise ratios were in very good agreement with predictions. Comparative noise surveys verified the existence of a noise minimum below 5 MHz in a maritime environment free from cultural contamination, which was exploited in the radar experiments. Signal-processing and multistatic multiple-target-tracking algorithms were developed. Preliminary tests were conducted on the latter with simulated data.

The main shortfall was the inability to demonstrate the multistatic tracker on real data due to an as yet unexplained problem with one of the receivers or its data processing. Usable radar signals were consequently available from only one of the two receivers. A very considerable effort was made to eliminate artifacts from the data, which had acted to raise the effective noise level. Although this effort was successful in significantly reducing the noise level, there are indications that further improvement may be possible with improved processing, which will permit a demonstration of the multistatic tracker. It has not yet been possible to look at the data collected at 7.8 MHz.



## References

1. A. A. Burns and W. J. Volchek, "Surface-Wave Over-the-Horizon Radar (SWOTHR)," Final Report, Vista Research Project 1004, Vista Research, Inc., Palo Alto, CA 94303 (February 1987).
2. CCIR (International Radio Consultative Committee), "World Distribution and Characteristics of Atmospheric Radio Noise," CCIR Report 322, International Telecommunication Union, Geneva, Switzerland (1964).
3. A. D. Spaulding and J. S. Washburn, "Atmospheric Radio Noise: Worldwide Levels and Other Characteristics," NTIA Report 85-173, U.S. Department of Commerce, Washington, D.C. (April 1985).
4. G. J. Fulks, HF Ground Wave Propagation Over Smooth and Irregular Terrain," Final Report DNA 5796F, Mission Research Corporation, Santa Barbara, CA 93102 (April 1981).
5. H. Bremmer, *Terrestrial Radio Waves/Theory of Propagation* (New York: Elsevier Publishing Co., Inc., 1949).
6. D. E. Barrick, "Theory of HF and VHF Propagation Across the Rough Sea," *Radio Science*, Vol. 6 (1971), pp. 517-533.
7. A. S. Eley, "Shipboard High Frequency Ambient Noise Investigation," Technical Memorandum, Naval Ocean Systems Command (11 December 1985).
8. S. S. Blackman. *Multiple-Target Tracking with Radar Applications*, (Norwood, MA: Artech House, Inc., 1986).

**Appendix A**

**Excerpts from the Initial Phase SWOTHR Test and Operations Plan**

## A.1 Introduction

### A.1.1 SWOTHR Description

Surface-Wave Over-the-Horizon Radar (SWOTHR) is a radar-system concept designed in particular to detect low-flying (surface-skimming) high-speed threats to a battle group. Surface waves hugging the highly conductive sea provide the propagation mechanism needed to reach threats hidden below the horizon. SWOTHR employs a single illuminator (transmitter) on one ship and three or more receivers carried by various ships in a battle group. Targets are detected coherently at each receiver and tracked by combining the time delay and Doppler shift information from the various receivers. A previous study showed this approach to be feasible, and predicted that the best performance would be achieved in the low-HF/high-MF frequency bands.

### A.1.2 Experiment Objective

The SWOTHR experiment is designed to verify basic multistatic surface-wave radar detection and tracking concepts. It will demonstrate system capabilities using inexpensive, off-the-shelf hardware.

### A.1.3 Experiment Description

The experiment will be performed with two receivers and one transmitter. The transmitter will be located approximately midway between the two receivers. This configuration will verify estimates of system performance.

An example of the predicted performance of the initial field test system is shown in Figure A-1. The deployment in this example consists of a transmitter between two receivers, each 15 km away on the arms of a 120° dogleg. In Figure A-1, threshold level *B* refers to the approximate threshold to be used in the SWOTHR experiment. A small jet fighter is used as the target for these calculations. At the 2-MHz carrier frequency, it is predicted that this target can be detected approximately 120 km away. However, the curves shown in Figure A-1 are probably very optimistic, especially at low frequencies, because of the choice of a low CCIR noise level and the use of a realistically high value for transmitter radiation efficiency.

The experiment sites for the preplanned low-altitude flights will roughly replicate the described scenario, and data will be collected for a cooperative target in the range of 30 to 200 km.

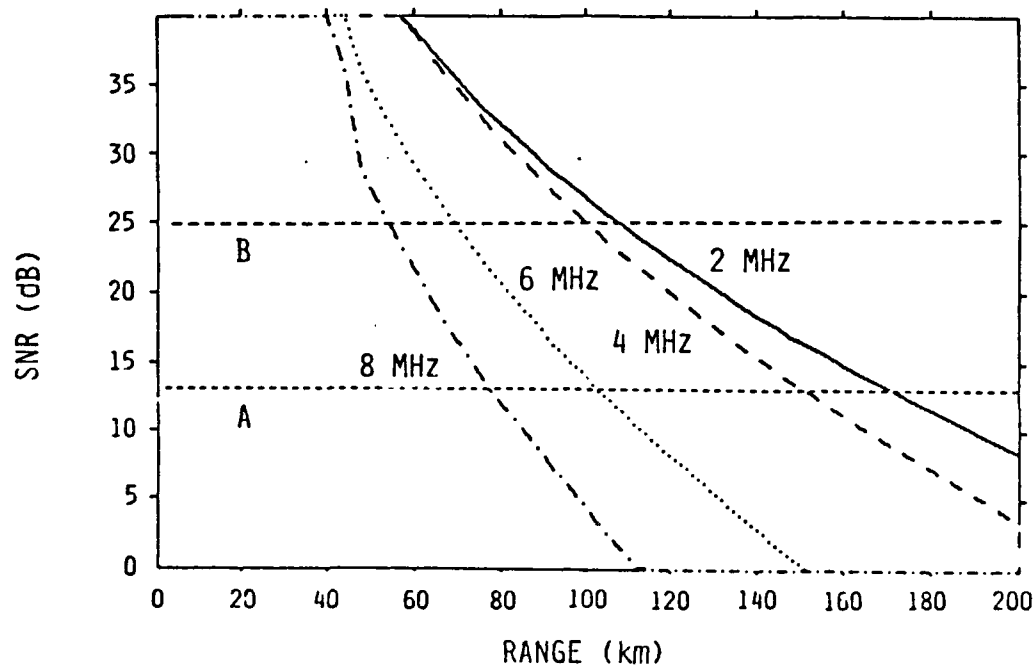


Figure A-1. Prediction of system performance of an initial field test using two receivers.

Targets of opportunity, which will also be used if they can be accommodated within the limits of experiment resources, are expected to be detectable at much greater ranges for two reasons. First, the altitudes of even low-flying targets of opportunity may be as much as 20 times higher than the preplanned low-flying targets. Because the propagation in both directions is via space wave in that case rather than surface wave, there will be far less signal loss. Secondly, the radar cross sections of targets of opportunity are expected to be greater than those of the cooperative targets because the latter will likely be airliners.

The data processing will emulate that of a real time system. Data obtained at each receiver will be reduced separately prior to being combined by the tracking algorithm.

## A.2 Required Equipment

The required equipment is listed in three sections : (1) transmitter, (2) receiver, and (3) special support equipment. The equipment listed for the receiver sites represents the amount required for one site. For this experiment it is necessary to equip two receiver sites.

### A.2.1 Transmitter Equipment

The following equipment is required for the transmitter site:

- Frequency Synthesizer (HP 5110A)
- Driver Amplifier (HP 5110A)
- Modulator
- Amplifier Power Supply
- Kenwood R-2000 Monitor Receiver
- Multi-element array antenna
- Cabling
- Oscilloscope

### A.2.2 Receiver Equipment

The following equipment is required for the receiver site:

- Kenwood R-2000 Radar Receiver (modified)
- 500-W Inverter
- Oscilloscope
- Computer and A/D board
- Two-Element Array Antennas

### A.2.3 Special Support Equipment

The following support equipment will be required:

- Antenna noise bridge
- Miscellaneous parts

### A.3 Test Sites

The transmitter and receiver sites will be located very close to the shoreline on the island of Kauai in Hawaii. This area was chosen because it is located in a low-noise environment and has relatively easy shoreline access, and because a reasonably controlled set of targets of opportunity, as well as preplanned flights, are available. A map of the area is presented in Figure A-2. A set of possible sites for both the target of opportunity portion of the experiment and the preplanned flight portion of the experiment are listed in order of priority. For each set of sites, the expected target detection area is also discussed. The approximate location of each of the sites is tabulated in Section A.2.3.

#### A.3.1 Targets of Opportunity Site

This configuration is designed for aircraft approaching and departing from the Barking Sands airstrip and flying in the W-186 area.

Site	Location
Receiver 1	Port Allen
Receiver 2	North of Barking Sands Airstrip
Transmitter	Kohole Point (South of WWVH)

#### A.3.2 Preplanned Flight Sites

Both a primary and a secondary site configuration are described below. The desired flight patterns for both configurations are defined in Section A.6.

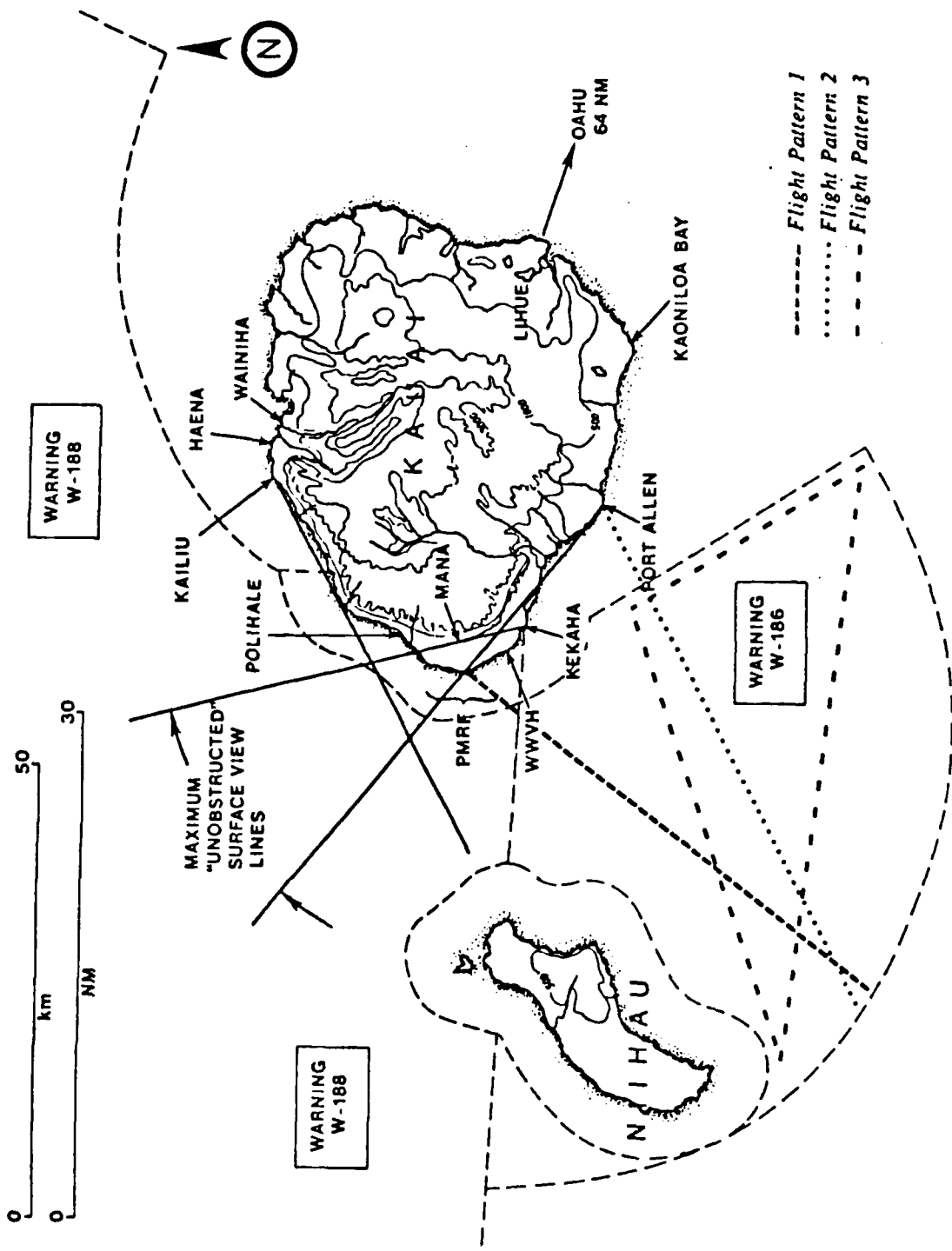


Figure A-2. Map of experiment area (showing flight patterns).

### A.3.2.1 Primary Site

This configuration is designed for targets flying in the W-186 area. Due to the presence of Niihau and the coastline of Kauai itself the flight plan has only a radial pattern.

Site	Location
Receiver 1	Port Allen
Receiver 2	North of Barking Sands Airstrip
Transmitter	Kohole Point (South of WWVH)

### A.3.2.2 Secondary Site

This configuration is designed for targets flying in the W-186 area, but the location of the transmitter and receiver differs from that of the primary site.

Site	Location
Receiver 1	Port Allen
Receiver 2	Poipu Beach Area
Transmitter	Kekaha

### A.3.2.3 Tertiary Site

This configuration is designed for targets flying in the W-188 area. Although it allows a long radial pattern, the projected baseline separation of the receivers is only marginally acceptable.

Site	Location
Receiver 1	Polihale
Receiver 2	Southern End of Barking Sands
Transmitter	Northern End of Barking Sands

### A.3.3 Site Coordinates

Figure A-2 indicates the approximate locations of the specified sites. The actual coordinates are noted below.

Site	Latitude	Longitude
Polihale	22° 05m 54s	159° 45m 14s
Pt. Allen	21° 53m 44s	159° 36m 20s
Poipu Beach Vicinity	21° 52m 38s	159° 26m 09s
North of Barking Sands Airstrip	22° 03m 15s	159° 47m 15s
Kohole Pt.	21° 58m 58s	159° 45m 45s
Kekaha	21° 58m 54s	159° 44m 25s

## A.4 Data Acquisition, Processing and Analysis

Data will be collected at the two receiver sites with A/D boards installed in portable 286-type personal computers. The data consist of bursts of 32 16-bit sample pairs digitized at a 100-kHz fundamental rate; the bursts are synchronized to the transmitter prf (pulse repetition frequency), which is approximately in the 175- to 650-pps interval. Data will be stored directly onto 132-Mbyte hard drives. Approximately 1 h of data can be collected with these hard drives, and this defines the duration of an experiment. After an experiment has been completed, the data for each site will be reduced by the individual receiver processing software. The results of this first data reduction at each site will be combined using a tracking algorithm to determine the track of the target. Adjustments to the preprocessing and tracking algorithms will be made as necessary. The original raw data will be backed up and archived for future analysis. A fraction of each day's data will be analyzed overnight to ensure data quality.

### A.4.1 Data Acquisition

Data will be acquired at a sampling rate of 25 kHz with a 16-bit 100-kHz throughput A/D board (DT2827) manufactured by Data Translation, Inc. The method of acquisition will be such that both the in-phase and quadrature components of the signal can be determined. This is done by externally clocking the A/D board to collect two samples 10  $\mu$ s apart every 40  $\mu$ s, so that the data are effectively sampled twice at the 25-kHz rate with a quarter-cycle

shift. Approximately a 1.0-ms burst of data will be collected starting with the arrival of each direct signal pulse from the transmitter, which will have a prf of 175 to 650 Hz. The digitized data will be continually logged asynchronously on a 132-Mbyte disk residing in the computer. At a pulse repetition rate of 250 Hz, 1.5 Mbytes of data are collected each minute, which limits the data collection to approximately 1 h. After the experiment is complete, the collected data will be archived to tape. To avoid data loss, two backup sets will be produced. This will require approximately 12 40-Mbyte tapes per day.

## **A.5 Operations**

### **A.5.1 Receiver Sites**

The primary and secondary receiver sites are listed in Sections A.3.1.1 and A.3.1.2. At each receiver site there will be one operator. The equipment is packaged so that the receiver, data acquisition unit, and antenna can be set up by an individual. It is estimated from rf noise-level experiments performed in the same area, and using essentially the same equipment, that the equipment can be easily installed and checked out within 1.5 h.

#### **A.5.1.1 Equipment Setup and Check-out**

The receiver, data acquisition system, and special test equipment will be set up inside vans. This will simplify transportation of equipment, provide electrical power, and also shelter the equipment in case of inclement weather. The antenna will be located far enough from the vehicle to avoid significant coupling, and far enough away to avoid noise from the inverter and the vehicle. The antenna is connected to the receiver via RG58 coaxial cable. After the basic setup of the equipment, receiver, and data acquisition system, the antenna must be set in the correct phasing and orientation, and a check of the system must be made. The following procedures indicate exactly what must be done for each piece of equipment so as to avoid incorrect settings, tuning, etc.

##### **A.5.1.1.1 Data Acquisition System**

Setting up the data acquisition system includes the following steps:

- 1) Attach power strip to inverter

- 2) Plug the following items into power strip:
  - Oscilloscope
  - Receiver
  - Computer
- 3) Connect the external clock signal from the receiver to the oscilloscope.  
Connect the 25-kHz signal from the receiver to the oscilloscope.
- 4) Attach the ribbon cable between the A/D card and the receiver.
- 5) Connect the RG58 cable from the antenna to the receiver.
- 6) Turn off the inverter.
- 7) Attach the inverter to the car battery.
- 8) Start the car, turn on the inverter, and turn on the equipment.

#### A.5.1.1.2 SWOTHR (Radar) Experiment

The receiver will be placed in the radar mode by turning the following switches and selectors to the appropriate settings.

Description	Setting
Calibration Attenuator	30 dB
Receiver (RF) Attenuator	0 dB
Tuning Speed	Slow (Locked)
Mode Selector	FM
AGC	(disabled in radar mode)
Squelch	Off
MGC (manual gain control)	Set to appropriate level
Normal/Radar Switch	Radar
Input Impedance Switch	50
Frequency Setting	Transmitter frequency
Tone/Volume	As desired

### **A.5.1.1.3 Antenna**

The antenna must be tuned and the two elements spaced correctly. The tuning is done once and is not changed unless the transmitting frequency is changed. The antennas are spaced as determined by the connecting RG cabling.

## A.5.2 Transmitter Site

### ***CAUTION : HIGH VOLTAGE at RF FREQUENCY***

*Approximately 10 kV will be present across the inductor at the base of the antenna. Severe burns can result even if no direct contact is made. All personnel should be a minimum of 10 ft from the antenna when the amplifier is in operation.*

#### A.5.2.1 Equipment Setup

The antenna system will be raised and left at the transmitter site. The following equipment will then be set up and connected: the transmitter, the oscillator board, the frequency synthesizer, the modulator and the antenna tuner. All the transmitting equipment will be housed in two portable 19-in. standard racks approximately 2 to 3 ft in height. The only cable, other than the RG8 coaxial cable from the transmitter to the antenna, therefore, will extend from the generator to these racks and between the racks.

***Warning:*** It is dangerous to power up equipment before the antenna system is set up and all connections are complete and checked.

#### A.5.2.2 Equipment Check-out

The equipment is checked out by monitoring the transmission pulse on an oscilloscope. A final check is made by communication with the receiver sites that the signal is being received at the appropriate level.

## A.5.3 Communications

Communication is essential not only between the two sites but also between the sites and the flight controller located at Barbers Point NAS, the departure point of the aircraft.

#### A.5.3.1 Site to Site

Given the desired configuration, a minimum requirement for site-to-site communication would be a direct link between each receiver site and the transmitting site. Citizen-band radios operating in the 27-MHz band range will be used to communicate between the transmitting site and receiver site located at PMRF Barking Sands. The receiver site

located at Port Allen will use a car telephone. Because local repeaters do not adequately support portable telephone use at Barking Sands, communication with Port Allen will be made via the communication/operations team at Barking Sands.

#### A.5.3.2 Site to Flight Operations (Controller)

It is required that a direct communication link be available between one of the sites (transmitter) and the flight controller. This will allow the cancellation of a preplanned flight if for any reason the experiment is not ready. Given the limited number of flights available and the cost of each flight, this capability is absolutely essential. The following procedure will be implemented to avoid loss of flight time.

- 1) The experimenters will request a flight pattern a minimum of 36 h prior to expected flight time.
- 2) Two hours prior to the flight, the experimenters will contact VC-1 at Barbers Point NAS by telephone to confirm or cancel the flight.
- 3) The flight from Barbers Point will land and the pilot will have a face-to-face meeting with the experimenters prior to commencing operations. This will ensure that a small delay will not cause the forfeiture of an entire flight.

## A.6 Experiment Procedure

### A.6.1 Targets of Opportunity

During experiments with targets of opportunity, the following procedure will be implemented.

- 1) Set up receiver and transmitter sites.
- 2) Perform normal check-out as outlined in Section A.5.
- 3) Run transmitter. Receiver sites determine threshold signal and verify that the direct signal is being received.
- 4) Perform experiment. If possible obtain information concerning the busiest flight times expected in the target area, and perform the experiment at this time. Listen to commercial flights on VHF to determine aircraft presence, and perform data collection during this period.

- 5) Perform processing and analysis. Compare tracking results to ground truth if available.

### **A.6.2 Preplanned Flight**

During experiments with preplanned flights, the following procedures will be implemented.

- 1) Set up receiver and transmitter sites. Specific instructions for setting up the receiver and transmitter sites are presented in Section A.5.1.2.1.
- 2) Perform normal check-out of receiver and transmitter equipment as outlined in Section A.5.1.2.1.
- 3) Run the transmitter. Receiver sites will then determine the threshold signal and verify that the direct signal is being received, and that the triggering process is working correctly.
- 4) Contact VC-1 at Barbers Point NAS and confirm or cancel flight. This will be done by one of the personnel at the transmitting site.
- 5) Wait for flight to arrive at Barking Sands and have a face-to-face meeting with the pilot.
- 6) Once it has been determined that the flight will take place, contact both receiver sites and establish a start time for data collection. This will remove the requirement of communication to initiate data collection.
- 7) Execute the flight and collect data.
- 8) Process and analyze data. Obtain "truth" data from the pilot after the flight. Compare tracking results to ground truth.

### **A.6.3 Ground Truth Data Sources**

Data gathered in the experiment will be compared to ground truth data sources, both in the case of targets of opportunity and in the case of preplanned flights.

#### **A.6.3.1 Targets of Opportunity**

Flight schedules, flight logs, pilot notes, and debriefings of pilots are some of the sources of ground truth to be used when the experiment involves a target of opportunity.

This information may be difficult to obtain, but an attempt should be made to do so. Furthermore, an effort should be made to obtain the location and vector heading of a target of opportunity when it enters the target area. The cost of planned flights is high, and detailed information on targets of opportunity could avoid a costly failure.

#### A.6.3.2 Preplanned Flights

When an experiment involves a preplanned flight, ground truth will be available from detailed logs kept by the pilot. First, the flight pattern or scenario is defined by the test plan prior to flight time, so that the expected flight path will be known. The pilot will be required to keep a detailed flight log of location, speed and heading. The pilot is required to maintain a constant velocity, and must record the ground speed, heading, and position information. At any time when the heading, course, and/or air speed is changed, the pilot must note the time and position, and the new velocity vector or the rate of change. Such a change would occur during a turn to produce the race track pattern or when the pilot is changing headings on the return radial pattern.

#### A.6.3.3 Preplanned Flight Patterns

The following are the flight patterns that have been planned for flights originating from Barbers Point Naval Air Station on the island of Oahu. The flight patterns are also indicated in Figure A-2. An A-4 aircraft from the VC-1 Squadron stationed at Barbers Point NAS will be used. Each flight pattern is either for the *primary* or *secondary* site configuration. To avoid miscommunication, flights will be referred to by the flight pattern numbers identified below.

*Note:* These flight patterns are intended to be illustrative; most likely, it will be necessary to adjust distances and courses as experimental experience is gained.

##### *Flight Pattern 1 (Primary)*

This pattern will approximately bisect the projected baseline of the two receiver sites for the primary site configuration. The projected baseline is approximately 15 km and the actual receiver separation is 27 km.

- 1) The aircraft departing from Barbers Point will take a heading of  $180^\circ$  magnetic North.

- 2) The flight will proceed by dead reckoning after the TACAN signal has been lost. After traveling approximately 70 km the flight will return on the same radial. It is expected that due to cross winds certain deviations from the headings defined here may be necessary; these are left to the pilots' discretion.
- 3) The flight will perform the radial pattern twice and then return to Barbers Point.

*Note:* As stated previously, the pilot is required to note position, air speed, ground speed, and heading as frequently as possible. When the PMRF TACAN signal is obtained on the outbound pattern and reacquired on the inbound pattern, the position and time must be recorded.

#### *Flight Pattern 2 (Secondary)*

This pattern will approximately bisect the projected baseline of the two receiver sites for the preplanned secondary site configuration. The projected baseline is approximately 21 km and the actual receiver separation is 30 km.

- 1) The aircraft departing from Barbers Point will take a course towards the VORTAC South Kauai traveling on the V16 airway.
- 2) When the aircraft is within 10 NM of VORTAC South Kauai, an attempt will be made to contact the experiment personnel located at Port Allen.
- 3) The aircraft will intercept the South Kauai VORTAC 232° radial and proceed outbound on a course of 232° at a 300-ft altitude at approximately 300 kn. When the VORTAC signal is lost, the aircraft will continue outbound on the same course by dead reckoning.
- 4) Upon reaching a distance approximately 39 NM from South Kauai VORTAC (the border of W-186), the flight will perform a standard turn, and climb if necessary, until it reacquires VORTAC South Kauai. The flight will then intercept the 232° radial, descend, and return on the reciprocal course, 52°, at an altitude of 300 ft and a ground speed of 300 kn.

- 5) The flight will continue inbound until it is approximately 10 NM from VORTAC South Kauai. At this time the aircraft will perform a standard turn and return outbound on a course of 232° and repeat the above pattern.
- 6) Upon completing the second inbound radial, Flight Pattern 2 is complete. It is expected that to complete Flight Pattern 2 will take approximately 25 to 30 minutes.

*Note:* As stated previously, the pilot is required to note position, air speed, ground speed, and heading as frequently as possible. When VORTAC South Kauai signal is obtained on the outbound pattern and reacquired on the inbound pattern, the position and time must be recorded.

### *Flight Pattern 3 (Secondary)*

This flight pattern is a triangular pattern flown in area W-186.

*Note:* The pattern described is designed to remain in the warning area W-186; it is very desirable to extend the pattern to the northwest by a distance factor of 2 to 3.

- 1) The aircraft departing from Barbers Point will take a course towards the VORTAC South Kauai traveling on the V16 airway.
- 2) When the aircraft is within 10 NM of VORTAC South Kauai, an attempt will be made to contact the experiment personnel located at Port Allen.
- 3) The flight will proceed on an outbound course of 240° at an altitude of 300 ft and a ground speed of 300 kn. The flight will continue on this course by dead reckoning.
- 4) When the flight is approximately 38 NM from VORTAC South Kauai it will perform a standard turn and climb in order to reacquire the VORTAC signal. The flight will then descend and take up a course of 33°.
- 5) The flight will continue for approximately 38 NM on this course.
- 6) Upon completing the 38 NM, or approaching the border of W-186, the flight will make a standard turn and increase altitude to reacquire VORTAC South Kauai (if necessary). The flight will then descend and proceed on a course of 323° until it is approximately 38 NM from VORTAC South Kauai.

- 7) The flight will continue on this course for approximately 22 NM. The pattern is complete when the flight is on the 240° radial.

*Note:* As stated previously, the pilot is required to note position, air speed, ground speed, and heading as frequently as possible. When VORTAC South Kauai signal is obtained at the end of the outbound pattern and reacquired on the inbound pattern, the position and time must be recorded.

## A.7 Data Processing

### A.7.1 Pre-Test Data QA

Prior to an experiment, the data acquisition system will be checked to assure that no fatal failures have occurred. This will be done by collecting a small amount of data and the producing a plot with a quick-plot (qlook) graphics package. The operator will ascertain if the transmitted signal is being received and recorded correctly.

Complete the following steps to assure that the data acquisition is proceeding as expected.

- 1) Set up receiver and data collection equipment.
- 2) Log data.
- 3) Display collected data and verify that magnitude output agrees with oscilloscope.

### A.7.2 Individual Receiver Signal Processing

A coherent integration period of 4 to 20 s of data is entered into the processing routine. The data are placed into a matrix, one row per pulse and one column per range cell. The columns of the matrix are demeaned and tapered and then transformed (FFT) from range/time space to range/Doppler space, and the resulting matrix is saved. The remaining range/Doppler data are searched for local maxima corresponding to possible targets (the local maxima are dependent on the threshold setting; processing may be repeated with different thresholds by means of the saved range/Doppler matrices previously computed). For each

local maximum determined, an estimate of the range and Doppler shift is obtained and output for use by the multistatic signal processing software. The data window is then moved approximately half a coherent integration interval, and the process is repeated.

### A.7.3 Multistatic (Combined Receiver) Processing

The receiver signal processing assumes, in determining the range/Doppler matrix, that site location is known. Specific site location is determined by using USGS maps at a 1:24000 scale. Thus the sites' locations will be known within at least 200 m.

The range/Doppler shift values for possible targets from the two receivers are input to the multistatic processing software. The input data are assigned to established tracks (if any, the assignment algorithm is to be selected from several alternatives based on comparison during the first runs). The remaining data values (if any) are assigned to existing tentative tracks. Tentative tracks are established for any remaining data values. Established tracks without data values are flagged and are deleted after some number (to be determined) of consecutive missing values. Tentative tracks with sufficient data become established, those tracks lacking sufficient data are deleted, and the remainder continue as tentative tracks. The established tracks are updated with current data values, and the track file is then updated.

Tracking can be performed in either range/Doppler space or location/velocity space. In either case, the tracking algorithm produces an estimate which minimizes a quadratic criterion function (i.e., variance, standard deviation) for a single step, and the final output (track file) is a sequence of estimates in location/velocity space. Currently, the components of the state vector ( $x$ ,  $y$ ,  $v_x$ ,  $v_y$ , or  $R1$ ,  $f1$ ,  $R2$ ,  $f2$ ) are modeled as independent quantities. A more complicated dependence structure can easily be included in the model, but the resulting increase in complexity and computation time does not produce a corresponding increase in tracking accuracy.

The resulting track file is compared to ground truth data obtained after the experiment has been performed. Ground truth will be used to determine algorithm validity and performance capabilities.

## **Appendix B**

### ***Equipment Description and Modifications***

## B.1 Equipment Description and Modifications

### B.1.1 Receiver

The radar receivers were extensively modified Kenwood R-2000 communications receivers. The R-2000 is a digitally synthesized triple-conversion general-coverage receiver with a 45.85- to 45.90-MHz first IF, a 9.85- to 9.90-MHz second IF, and a 455-kHz third IF. Its basic coverage is 0.15 to 30 MHz. MOSFET transistors are employed in the rf amplifier stage and as balanced mixers. All of the local oscillator signals are derived from a 9-MHz crystal-controlled oscillator, which has frequency stability and accuracy specification of better than 2 ppm per 30 min and 10 ppm, respectively. Based on published specifications, the noise figure of the R-2000 should be about 19dB; this was verified by direct measurement.

Figure B-1 is a simplified block diagram of the receiver. Modifications are shown as dashed lines. For the radar mode, the receiver was modified to operate under manual gain control and to pick off the final IF signal after the 15-kHz FM filter. The wider FM bandwidth provided adequate radar range resolution, which would not have been available using the narrower, 2.7- and 6-kHz AM bandwidths. Outputs from the AM and FM level detectors were provided at the rear of the receiver for monitoring purposes.

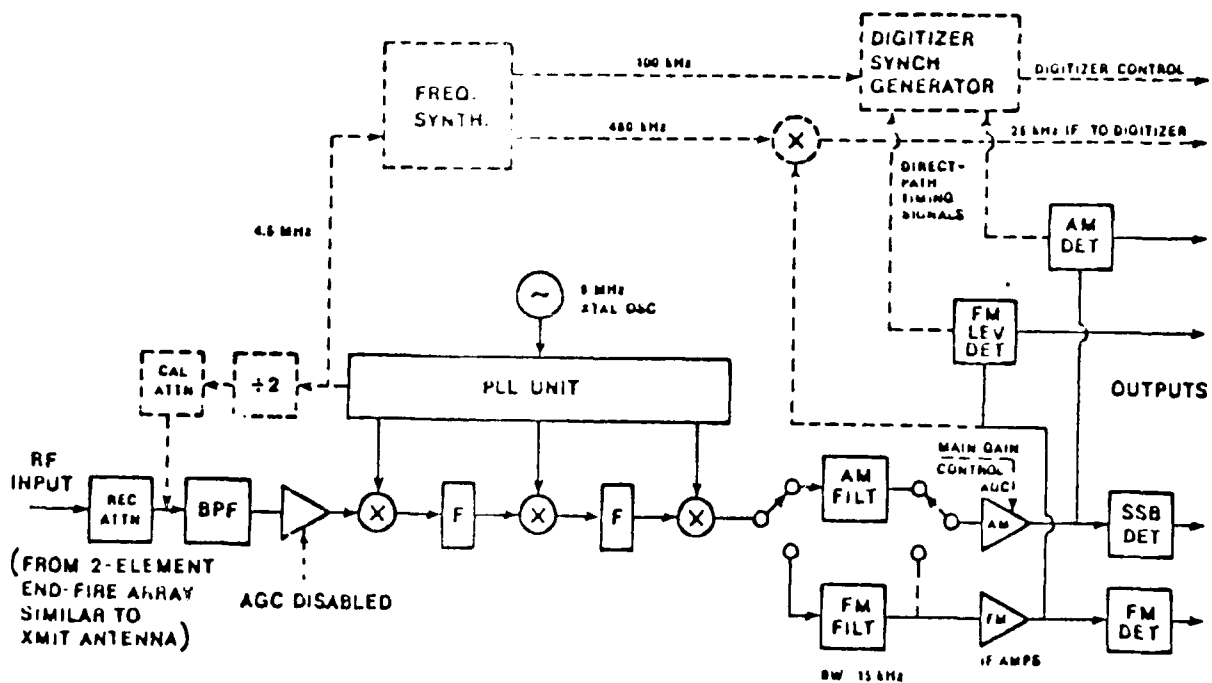


Figure B-1. Receiver block diagram.

A fourth conversion stage was added to produce the 25-kHz IF signal, which was also fed out of the receiver to the (IQ) digitizer card. This used an LM1496 balanced modulator linear IC, which is stated to have 90-dB dynamic range at optimum drive levels, driven by a 480-kHz LO signal. The 480-kHz signal was obtained by dividing a 4.5-MHz signal already present in the receiver, using a phase-locked loop. A 100-kHz reference was generated in a similar way. This was used to produce the quadrature sample trigger signal for the digitizer. Thus all of the LO signals and the sample timing signal can be traced to the 9-MHz master oscillator in the receiver.

The remainder of the radar synchronization generator added to the receiver controlled the timing of the sample burst sent to the digitizer. After the operator had set up the computer and thrown the "start" switch, an "arm" signal was sent to the digitizer, which prepared it to take samples. The digitizer then took over the computer. Whenever the received signal exceeded a manually adjustable threshold, a burst of quadrature sample triggers were sent. A pre-adjustable counter controlled the burst duration, which was set at 32 quadrature pairs for this experiment. Burst trigger thresholds were to be set to fire on the leading edge of the direct signal from the transmitter. The operator could select the output of either the FM level detector or the AM detector as the input to the threshold detector (these two had somewhat different characteristics because the former was saturated). An adjustable "hold-off" could be used to prevent retriggering until another direct pulse arrived. Another output allowed the operator to monitor the "hold-off" signal and thus optimally set it. A final option permitted the operator to use a phase-locked oscillator set to the prf and tie it to the threshold detector. This loop was not needed, fortunately, since it often exhibited enough intrinsic jitter to slew the digitizer burst by a range cell; the direct signal from the transmitter was overwhelming and produced a clean digitizer burst if the threshold was correctly set. A higher order PLO would be needed to overcome this difficulty. These latter circuit features were included as contingencies to deal with high impulsive-noise-level situations.

As an aside, we note that it would be feasible to phase-lock the receiver to the transmitter with a modest further effort. This can be done by gating the direct signal and comparing it to a signal derived from the 9-MHz master oscillator. Then a phase-locked loop can be closed around the 9-MHz oscillator.

The final modification was the addition of a 2.25-MHz calibration signal. This was obtained by dividing the 4.5-MHz signal from the receiver and feeding it into the receiver front end through a series of fixed and variable attenuator stages.

### B.1.2 Waveform

The impulse response of the 15-kHz receiver filter was modeled analytically in order to estimate its impulse response, which in turn was used to design the transmitter waveform. This is the reverse of, but is analogous to, the normal procedure in which the filter is designed to match the waveform. Based on the published specifications and measured frequency response (Figure C-3), it was decided to model the filter as a fourth-order maximally flat gain function. Figure B-2(a) shows its impulse response, which was calculated by taking the Fourier transform of its gain function. Figure B-2(b) is the corresponding matched filter output. The impulse response can be seen to be very close in form to a cosine-weighted pulse, so it was decided to use a 64- $\mu$ s half-width raised-cosine transmitter waveform. Figure B-2(c) shows the resulting receiver output pulse, which also has a half width of 82  $\mu$ s. This response has better time sidelobe characteristics than does the matched response. Bench tests using the transmitter waveform confirmed that the actual receiver output closely duplicated Figure B-2(c), including many of the details of the ringing trailing the main pulse.

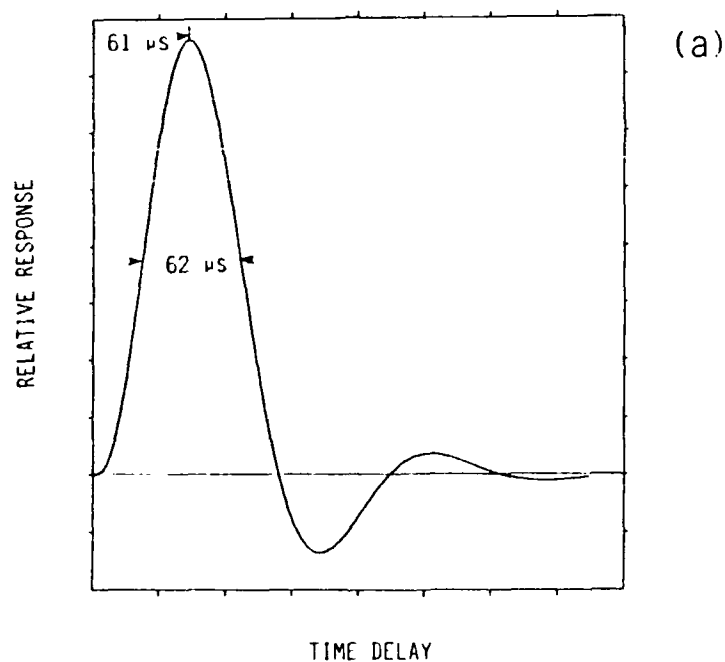


Figure B-2. Theoretical receiver time responses; (a) impulse response, (b) matched waveform response, (c) raised-cosine response.

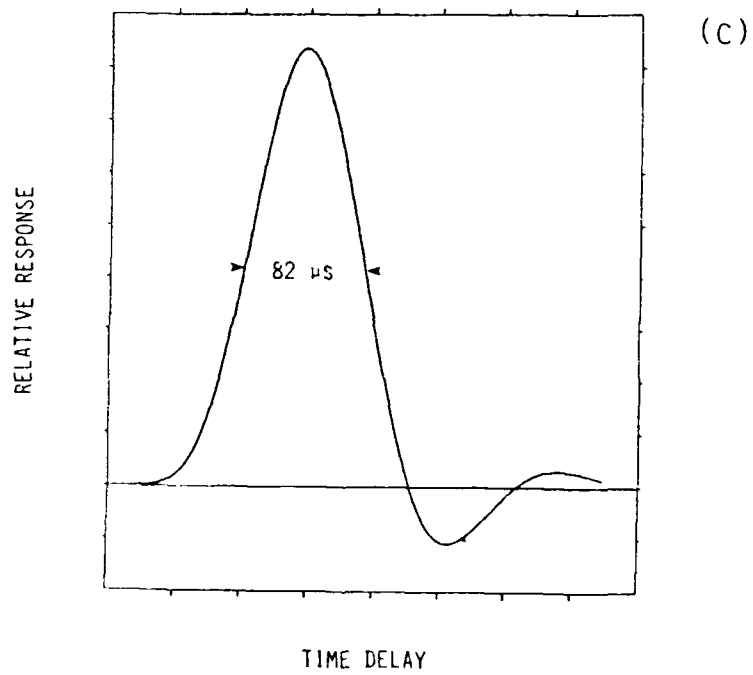
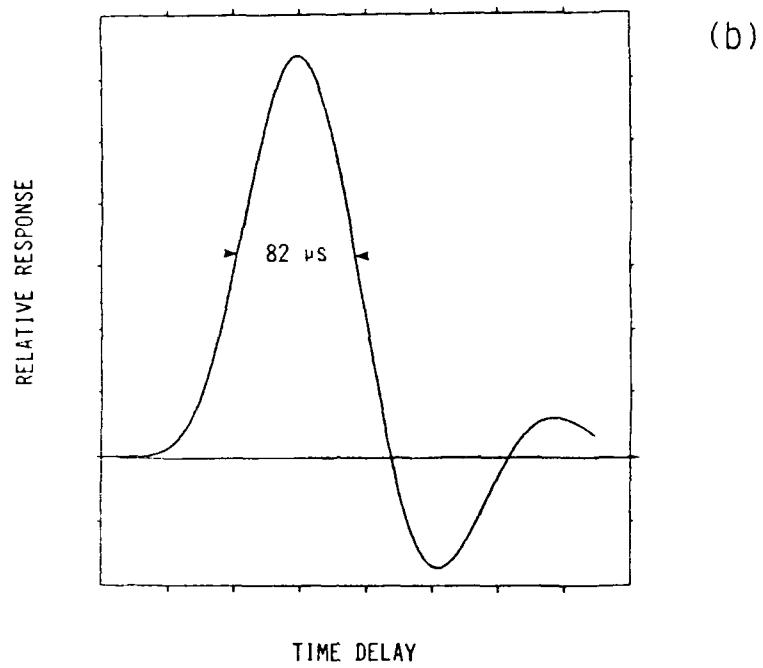


Figure B-2 (concluded). Theoretical receiver time responses; (a) impulse response, (b) matched waveform response, (c) raised-cosine response.

The raised-cosine waveform itself was digitally synthesized by means of a 16-part sequence of voltage levels, each of 8- $\mu$ s duration. Timing was controlled by the HP-51 synthesizer that provided the transmitter frequency reference. This approach produced an extremely stable and clean transmitted waveform.

### B.1.3 Transmitter

Figure B-3 is a block diagram of the transmitter. It consisted of the HP-51 frequency synthesizer, a waveform synthesizer and modulator, a wideband power preamplifier, a 2-kW peak linear final power amplifier, and an antenna tuner. It was not necessary to use the feedback loop shown in the diagram due to the inherent stability of the amplifiers. The waveform synthesizer and modulator was a Vista design that used high-speed CMOS technology and an LM1496 balanced modulator chip. No tuning was required, as the modulator was a wideband, low-pass circuit. The 100-W output preamplifier was also a wideband unit, capable of covering the entire MF and HF bands. Low-pass filters were inserted between the modulator and preamplifier to suppress spurious signals. A portable generator easily powered the transmitter, which had an average power output of less than 100 W.

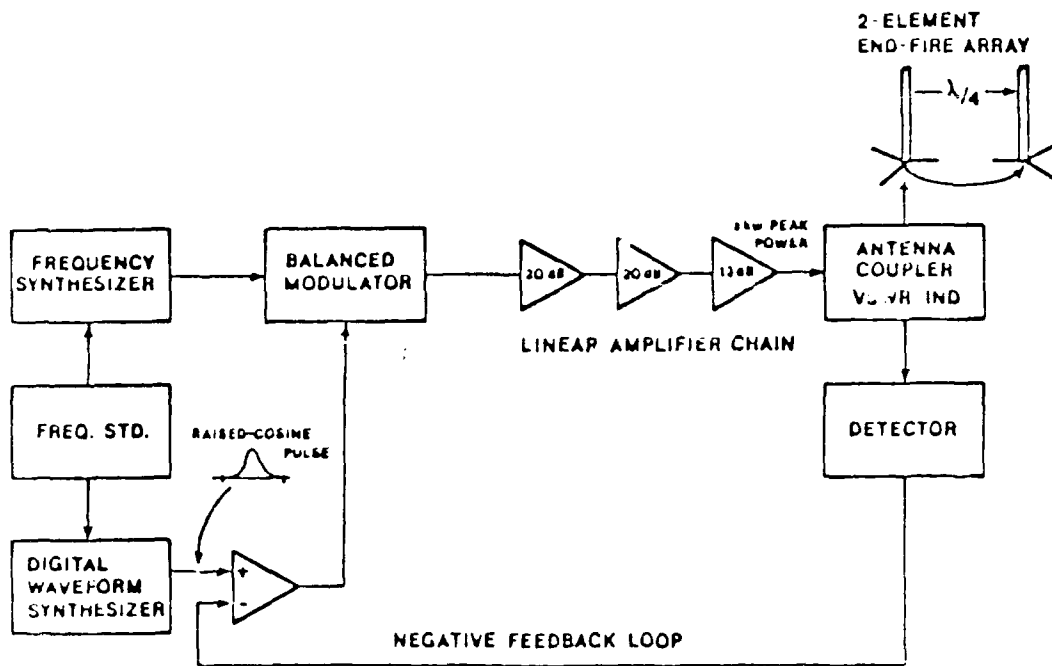


Figure B-3. Transmitter block diagram.

#### B.1.4 Antennas

Two-element arrays spaced a quarter-wavelength apart were used for both transmitter and receiver sites. They were emplaced and phased, with  $\lambda/8$  and  $5\lambda/8$  transmission line sections, so as to produce a broad mainlobe in the direction of the flight operations. In what represents a considerable design effort, the NEC code was used to optimize the antennas, calculate antenna efficiency factors, and provide guidance for placing taps on the tuning coils for both impedance matching and frequency tuning. In most instances, the predicted tap locations were very close to those arrived at during antenna tuning in the field, which supports the correctness of the antenna efficiency calculations.

The transmitter antenna was a pair of vertical whips with wire ground planes. Slightly different configurations were used at 2.8 and 7.8 MHz. At 2.8 MHz, these were 33.8 ft (10.3 m) whips with a ground screen consisting of 12 wires 75 ft (22.9 m) long. Top, center, and base loading was employed at the lower frequency. It was necessary to load the top and center in order to raise the efficiency to an acceptable level and to reduce the capacitive reactance of the antenna. The center loading coil was located 20 ft (6.1 m) above the base, and the capacitive hat consisted of a wire tetrahedron with 1-m sides. The tetrahedron was part of the upper set of guy ropes. At 7.8 MHz, where the whip closely approximated a quarter-wave monopole, the top section of the whip was removed, and only base loading was used, for fine tuning and impedance matching purposes. In that case the overall length of the whip was 30 ft (9.1 m), which made the antenna slightly capacitive.

Extensive analysis with the NEC code was done in order to optimize the antenna and to predict impedances and efficiencies. These calculations used the low value for soil conductivity expected for the Hawaii sites, and showed that most of the energy loss was into the ground. A large part of this effort was to determine how many radials were needed in the ground plane, and how long they should be. This is a tradeoff between efficiency and the difficulty of setting out the radials. It was determined that only slight improvements (a few percent) in efficiency at 2.8 MHz could be achieved by increasing the number of radials substantially above 12 and the length above 25 m. These calculations were for unloaded whips, and produced theoretical efficiencies about 21% for that ground plane and bare whip at 2.8 MHz; however, losses in the loading elements preclude reaching that level and eventually dominate, which means that enlarging the ground plane would have been a fruitless exercise in any event.

Table B-1 summarizes the calculated parameters of the individual whips. The antenna input impedances at 2.5 and 2.8 MHz are based on the calculated values of the loading coils as finally employed. We found that the whips were somewhat inductive at 2.8 MHz when the original value for center-loading inductance was used, so we reduced it about 50% to ease tuning and matching. The non-zero values for the reactive components of the input impedances are due to small differences between the formula-based calculated values of the inductances and the actual values (also, the nominal value for the base coil at 2.5 MHz was used in the calculation for 2.8 MHz). These small differences had negligible effect on the real part of the impedance and on the calculated efficiency. The imaginary part was essentially zeroed by the antenna tuning. At 7.8 MHz, where the center coil was not used, the predicted base-coil tap locations for tuning and matching were found to be very close to the predicted locations.

Table B-1 Calculated Transmitter Antenna Element Parameters

Frequency	2.5	2.8	7.8	MHz
Efficiency	16	19	28	%
Input Impedance				$\Omega$
with Base Coil	8.2 - j18	9.2 + j50	-----	
w/o Base Coil	-----	-----	52 - j32	
Inductance				$\mu\text{hy}$
Center Coil	29.5	29.5	none	
Base Coil	22.9	22.9	-----	
Length				m
Ground Screen				
Number	12	12	12	
Length	23	23	23	m
Soil Parameters				
$\epsilon_r$	5	5	5	
$\sigma$	$10^{-4}$	$10^{-4}$	$10^{-4}$	$\text{sm}^{-1}$

Fifteen-foot (4.6-m) whips were used for the receiving antenna elements at both frequencies. Only base loading was used for these antennas. Again, extensive analysis was performed with the NEC code. For these shorter antennas, increasing the number of

ground-screen radials and their lengths above 8 and 15 ft, respectively, produced a rapidly diminishing return in efficiency. Table B-2 summarizes the receiving whips. Much larger base inductances were needed than for the transmitter whips in order to tune the shorter receiver antennas. At both 2.8 and 7.8 MHz, the predicted tap locations turned out to be very close to those needed for tuning and matching.

**Table B-2** Calculated Receiver Antenna Parameters

Frequency	2.5	2.8	7.8	MHz
Efficiency				%
w/o Base Loading	3.7	5.1	17	
with Loading Coil (Q = 300)	1.6	2.2	15	
Radiation Resistance	0.15	0.19	1.4	$\Omega$
Q (inc. Base Coil)	170	170	40	
$\Delta f$ (antenna bandwidth)	15	17	190	kHz
Input Impedance (w/o Loading)	4.1 - j1630	3.8 - j1450	8.2 - j380	$\Omega$
Length	4.6	4.6	4.6	m
Ground Screen				
Number	8	8	8	
Length	4.6	4.6	4.6	m
Soil Parameters				
$\epsilon_r$	5	5	5	
$\sigma$	$10^{-4}$	$10^{-4}$	$10^{-4}$	$\text{sm}^{-1}$

### B.1.5 System Operating Noise Figure

The overall system operating noise figure is given by

$$f = f_a + (l_c - 1) \frac{T_c}{T_0} + l_c(l_t - 1) \frac{T_t}{T_0} + l_c l_t (f_r - 1),$$

where

$f_a$  = external noise factor

$l_c$  = antenna circuit available power loss (available input power/available output power)

$l_t$  = transmission line available power loss

$T_c$  = antenna/ground temperature

$T_l$  = transmission line temperature

$T_0$  = reference temperature (288 K)

$f_r$  = receiver noise figure

If  $T_c = T_l = T_0$ , and  $l_l = 1$  (lossless line),

$$f = f_a + (l_c - 1) + l_c(f_r - 1)$$

For a matched antenna,  $l_c$  is the reciprocal of the efficiency. Thus, at 2.8 MHz, the nominal value for  $f$  is 38 dB, since  $f_a$  and  $f_r$  are 35 and 19 dB, respectively, and the calculated antenna efficiency is 2.2%. At 2.8 MHz, then, the nominal operation was just at the background limit, which was as experienced. At 7.8 MHz, the nominal background level was the same, but the efficiency was 15%, so  $f$  is 35.7 dB nominally. It is clear that improving the receiving antenna efficiency to achieve much beyond operation at the threshold of background-limited operation is not worth a major effort. For example, to attain a 2.3-dB improvement at 2.8 MHz, to match the performance at 7.8 MHz, an antenna height of 45 ft would be required, as well as a commensurately large ground screen, which would not have been feasible for this experiment.

**Appendix C**

**Noise Survey Results**

## C.1 Introduction

### C.1.1 Description

Surface Wave Over-the-Horizon Radar (SWOTHR) is a multi-static radar system concept whose best performance is predicted to occur in the low-HF/high-MF frequency band. It employs a single illuminator (transmitter) on one ship and three or more receivers carried by various ships in a battle group. Threats are detected coherently at each receiver and tracked by combining the time delay and Doppler shift information from the various receivers.

The initial SWOTHR experiment is designed to verify the basic detection and tracking concepts of this system. Because it was expected to provide a relatively benign and controllable test environment, the Hawaiian island of Kauai was picked as the preferred test site.

### C.1.2 Site-Survey Objective

Prior to fielding the SWOTHR experiment, a survey of proposed test sites was made (1) to verify expected ambient rf noise levels, (2) to compare noise levels at the proposed site to noise at other (mainland) locations, (3) to determine the effects of the shoreline and overland propagation paths on the rf signal strength, and (4) to obtain first-hand knowledge of the physical aspects of the sites. In order to launch surface waves efficiently over the sea, it is important that antennas be located immediately at the shoreline, which means that physical access is very important.

### C.1.3 Summary of Results

The results of the field site and noise survey done in February 1988 showed that the anticipated rf noise levels were as expected. Furthermore, the site survey showed that site accessibility was such that both the transmitting and receiving sites could be easily deployed and that the antennas would be relatively close to the ocean surface.

## C.2 Site Survey

Seven different sites were surveyed for physical accessibility and proximity to the ocean. A map of the site locations is shown in Figure C-1. Three of the sites, Polihale, Kekaha, and Port Allen, appeared to provide the best combination of proximity and accessibility for the receiver and transmitter sites. Port Allen was by far the most accessible and was next to the

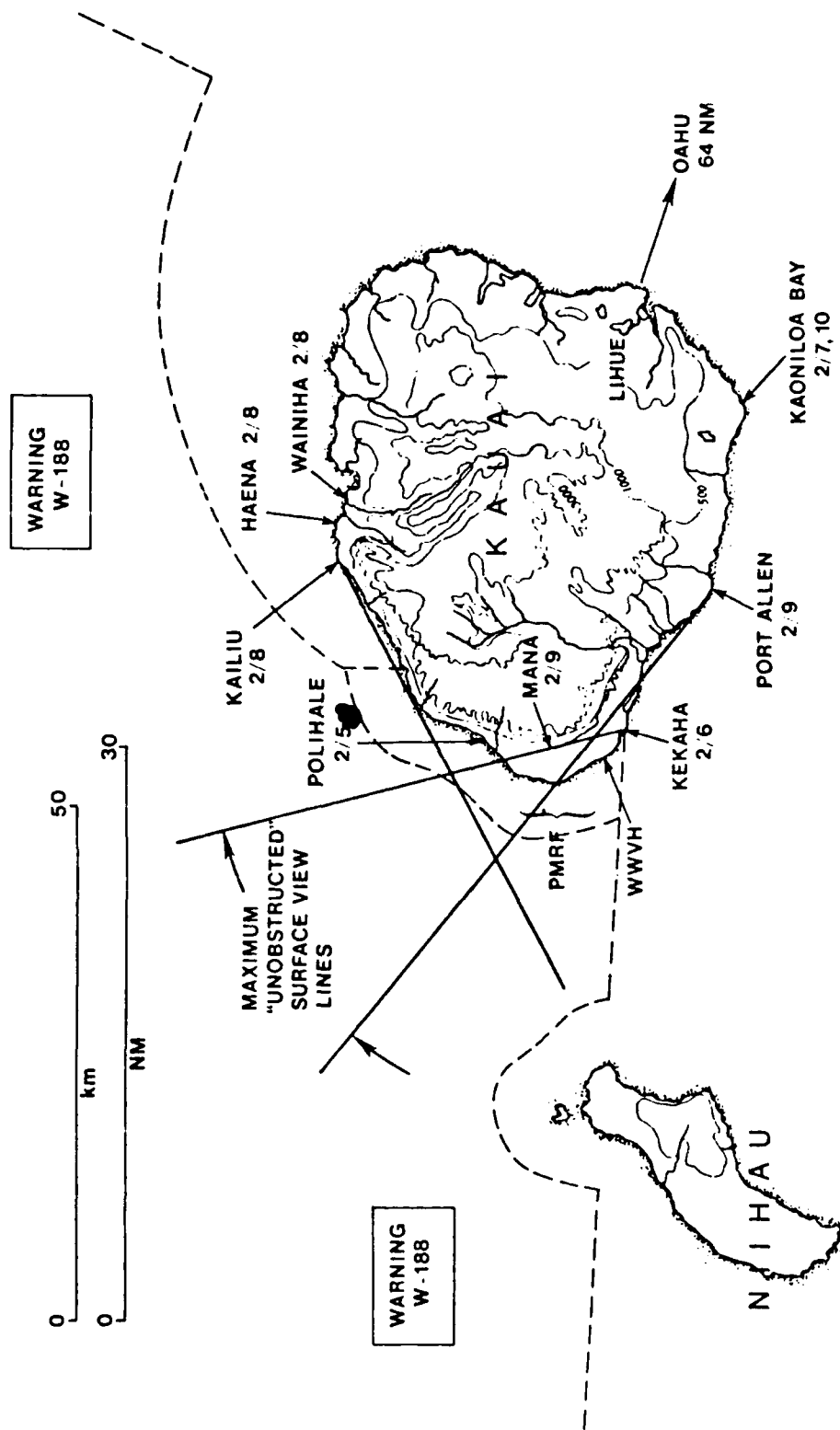


Figure C-1. Location of survey sites and noise measurements at each site.

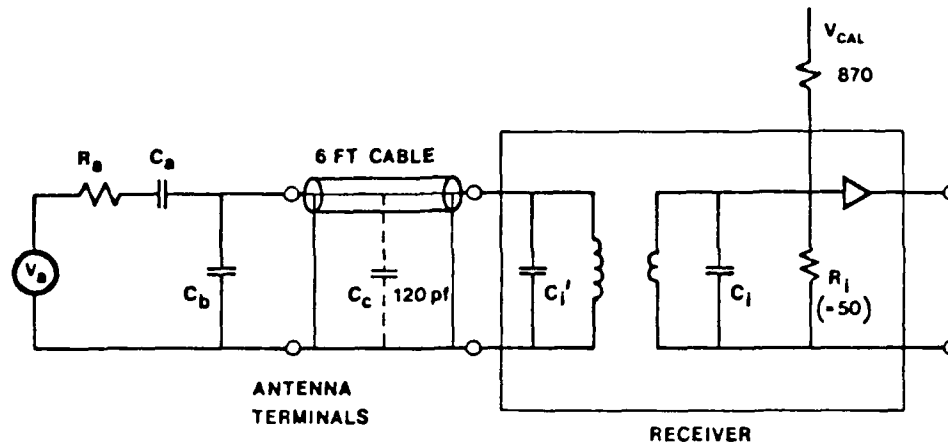
water. Two other sites, not displayed on the map, were also very promising. These were located at Barking Sands, near the WWVH transmitter and on the north end of the Barking Sands air-strip. However, no noise measurements were made directly on Barking Sands. For the primary configuration defined in the test operations plan, it was decided to place the transmitter near WWVH, with one receiver on the north end of Barking Sands and the other at Port Allen. Polihale, although not inaccessible, involved a long trek, and a communication link was difficult to establish. The Barking Sands location allowed reasonable communication between the sites and also allowed the permanent deployment of the transmitting antennas and, at one site, the receiver antennas.

### **C.3 Noise Measurement Approach**

Excess noise due to external sources is referred to a unique but physically inaccessible point in the antenna: the terminals of a hypothetical equivalent lossless antenna, whose characteristics, other than efficiency, are identical to the actual antenna. Measurable signals at the actual antenna terminals are affected by the antenna circuit. The actual power or voltage measured is lower than the available power due to the losses such as antenna mismatch. In order to determine the available noise power, an equivalent circuit for the antenna was modeled and then used to compensate for the loss from the mismatch. The final available power that is measured is related to  $kTB$  by means of the calibration signal injected into the receiver's front end

#### **C.3.1 Antenna Model**

A simple equivalent circuit diagram of the antenna/receiver system is presented in Figure C-2.



$C_a = 70 \text{ pF}$  FOR 10-FT ANTENNA (THEORETICALLY)

Figure C-2. Simple equivalent circuit diagram of the antenna/receiver system.

The available power,  $P_a$ , can be written in terms of the measured power,  $P_i$ , as shown in the following equations :

$$P_a = \frac{|V_a|^2}{4R_a} = \frac{|T_a T_b|^2}{4R_a} \cdot R_i P_i = TT \cdot P_i$$

where

$$T_a = \frac{\ddot{Z}_1 + R_a + \frac{1}{j\omega C_a}}{\ddot{Z}_1}$$

$$T_b = \frac{\exp -j\beta l + \rho \cdot \exp j\beta l}{1 + \rho}$$

$$\dot{Z}_1 = Z_0 \cdot \frac{n^2 \cos \beta l + j Z_0 \sin \beta l}{Z_0 \cos \beta l + j n^2 R_i \sin \beta l}$$

$$\ddot{Z}_1 = \frac{\dot{Z}_1}{\frac{j\omega C_b}{z_1 + \frac{1}{j\omega C_b}}}$$

$$\rho = \frac{n^2 R_i - Z_0}{n^2 R_i + Z_0}$$

TT is used as a correction factor to convert the measured voltage to the available power. Certain unknown parameters in the solution of the antenna circuit were solved empirically; these include the base capacitance,  $C_b$ , and the input impedance,  $R_i$ . The radiation capacitance,  $C_a$ , and the radiation resistance,  $R_a$ , were determined theoretically from the model of a short ( $< \lambda/4$ ) monopole antenna above an ideal perfectly conducting surface.

The method of determining  $C_a$  and  $R_a$  is presented below<sup>1</sup>:

$$R_a = 20 \cdot (\beta l)^2$$

$$C_a = \frac{1}{120 \cdot \ln\left(\frac{l}{a} - 1\right)}$$

The values for  $R_i$  and  $C_b$  were determined empirically in the following way. The antenna connection was replaced first with a 50- $\Omega$  resistive load at the receiver input and then with a series of capacitors. The change in output voltage was then measured for each configuration. The ratio of  $V_a/V_c$  (capacitor load/50- $\Omega$  load) was obtained at 2.25 MHz. An equivalent circuit solution, as a function of capacitance, was also plotted with the empirically determined results. The equivalent circuit solution results in a family of parametric curves dependent on the input impedance value,  $R_i$ . Figure C-3 shows that there is good agreement between the empirical curve, corresponding to a value of 70  $\Omega$  for  $R_i$ , and the theoretical prediction. Thus, 70  $\Omega$  was used for  $R_i$  in the compensation formula, TT. To measure the ratio  $V_a/V_c$  for the antenna, the ground plane was connected to the receiver. Thus, as shown in Figure C-3, an equivalent value for the combination of  $C_a + C_b + C_c$  can be obtained.  $C_a$ ,  $C_b$ , and  $C_c$  look like three capacitors in parallel when the voltage,  $V_{cal}$ , is examined; given that  $C_a$  and  $C_c$  are known, a value for  $C_b$  is determined. The measured ratio for  $V_a/V_c$  with the antenna connected was 0.85; therefore, the combined capacitance is approximately 210 pF. Given that the expected theoretical value of  $C_a + C_c$  is 155 pF,  $C_b$  is then approximately 55 pF.

The resulting correction factor, TT, is presented in Figure C-4 as a function of frequency. The parameters determined from the calculations shown in Table C-1 were used to obtain TT, which compensates for the loss of antenna sensitivity due to mismatch.

---

<sup>1</sup> Jasik, H. (ed.), Antenna Engineering Handbook, McGraw-Hill, New York, 1961.

### C.3.2 Exact Antenna Calculations

The antenna model shown in Figure C-2 and used in calculating the signal level was based on the standard formula for a monopole above a perfectly conducting surface. In reality, our measurements were made on low-conductivity surfaces (e.g., beach sand). A small ground plane consisting of four 9.1-m radial wires was used to compensate partially for the low conductivity surface. Vista Research has made, for this antenna configuration, a method-of-moments (MOM) calculation from which values for the ground-loss resistance as well as for the radiation resistance and the antenna capacitance are obtained. Table C-1 shows the results of this calculation. The standard value for ground (beach sand) conductivity,  $10^{-4}/(\Omega\text{-m})$ , was used to calculate the values shown in Table C-1.

### Calibration Voltage Output vs Capacitance (2.25 MHz)

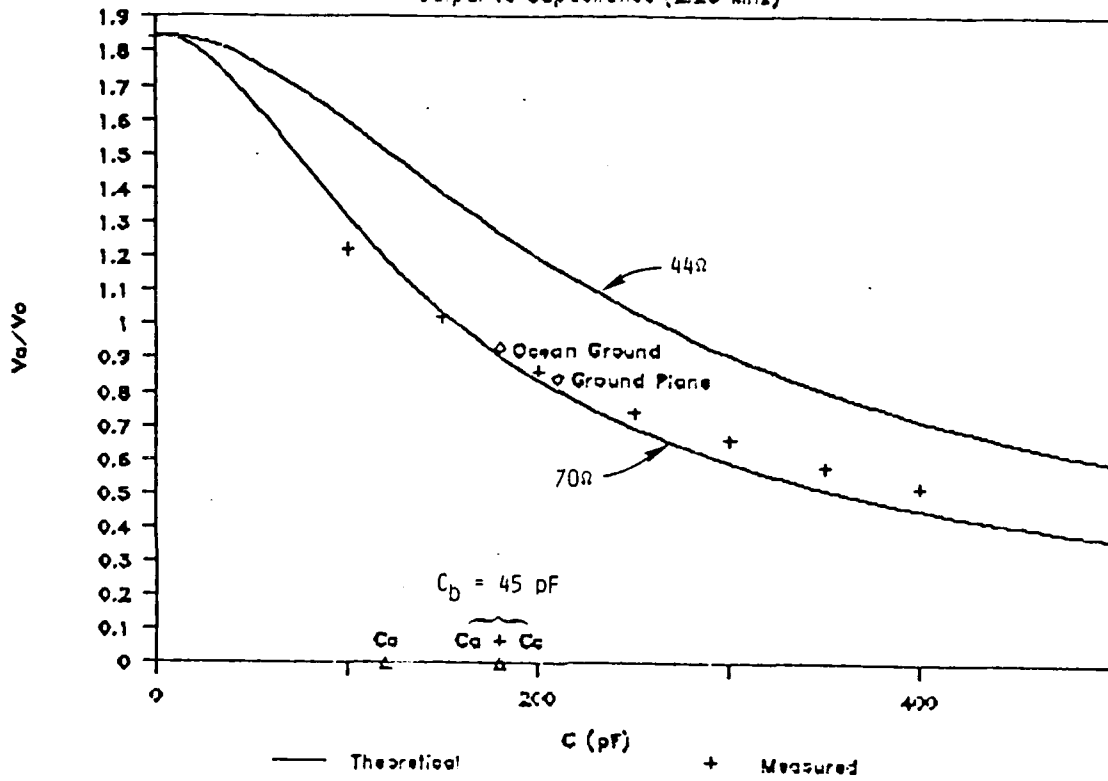


Figure C-3. Ratio of  $V_a/V_c$  as theoretically predicted and as measured.

# TT correction

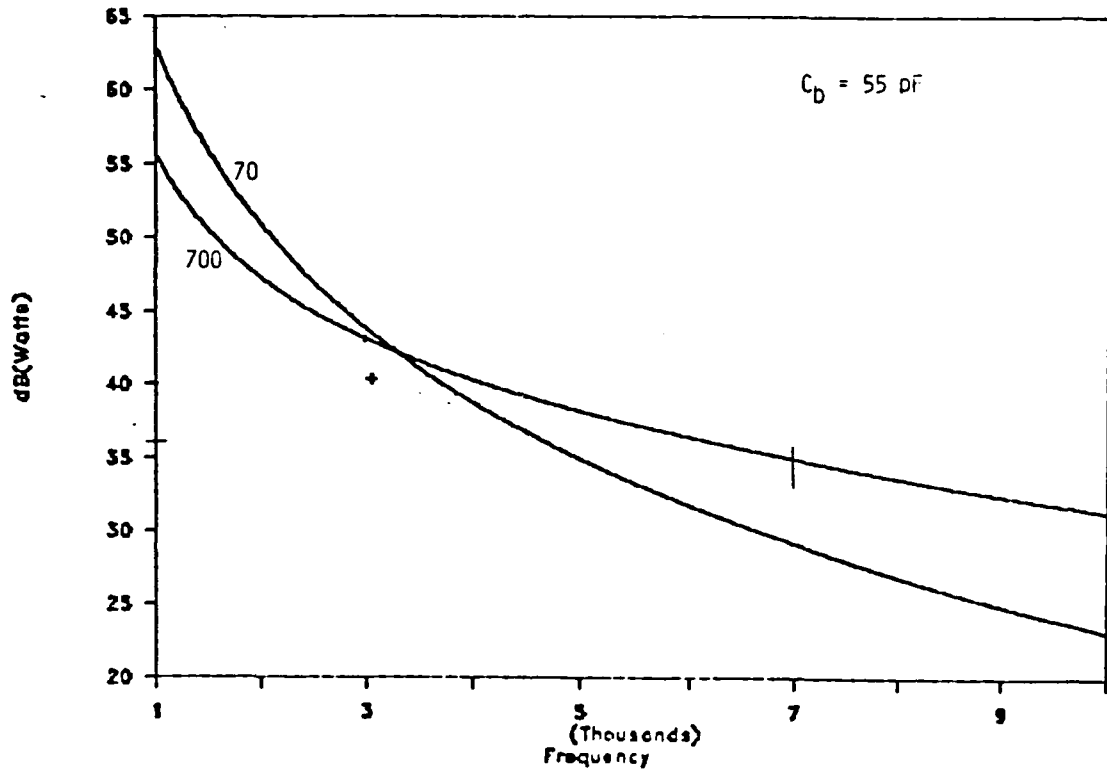


Figure C-4. Correction factor TT.

**Table C-1. Exact Antenna Calculation Results**

Frequency (MHz)	Radiation Resistance ( $\Omega$ )	Ground-Loss Resistance ( $\Omega$ )	Capacitance (pF)	$R_a$ ( $\Omega$ )
2	0.05	9.4	27	0.16
3	0.09	3.7	27	0.37
4	0.18	3.4	27	0.65
5	0.29	2.9	28	1.02
6	0.42	2.7	29	1.47
7	0.62	3.0	31	2.00
8	0.88	4.3	33	2.61

Also listed in Table C-1 is the ideal-antenna radiation resistance,  $R_a$ , which was used for determining the absolute noise level. The ideal antenna capacitance is 34 pF, which is close to the value obtained from the MOM calculations.

The ground-loss resistance appears in series with the radiation resistance. Although it is significantly larger than the radiation resistance for this small antenna, it does not affect the TT correction factor significantly because the reactance of the capacitor is much larger than it is in this band. The smaller value (< 34 pF) for the capacitance has a minor effect on the TT factor (~2 dB) at the low-frequency end.

However, the lower value of the radiation resistance does have a significant effect. The radiation resistance from the exact calculations is approximately 30% of the ideal value across the 2- to 8-MHz band, which increases the available power, and hence the inferred external noise factor, by 10 to 11 dB across that band.

#### C.3.2.1 Ground Conductivity

A measurement of the DC conductivity of beach sand was made at one site (Kekaha 02/06/88). The antenna at this site was located in relatively dry dune material, relatively far from the shoreline. The measurements were of the DC resistance between two

grounding rods 0.95 cm in diameter and 2.67 m apart. The two rods were buried at equal depth. This depth was variable with each measurement that was made. It can be shown that the resistance between the rods is given by the following equation:

$$R \cong \frac{1}{4\pi\gamma L} \left( \ln \left( \frac{16L^2}{d^2} \right) - \ln \left( \frac{L + \sqrt{L^2 + D^2}}{-L + \sqrt{3L^2 + D^2}} \right) \right)$$

for  $L^2 \gg d^2$ , where

$\gamma$  = conductivity

D = distance between rods

d = rod diameter

L = burial depth of rods

Our measurements agree with the standard value for ground conductivity shown in Table C-1.

Table C-2 summarizes the measurements and inferred ground conductivity. A value of  $\gamma = 10^{-4}$  S/m is typical of beach sand. The increased conductivity with the larger value for L was presumably due to increased moisture deeper in the sand. Pouring sea water over the grounding rods did not change the value of the resistance between the rods, which was 9 k $\Omega$ .

Table C-2. Resistance Measurements and Conductivity Values

L (m)	R (k $\Omega$ )	$\gamma$ (S/m)
0.46	24.5	$7.5 \times 10^{-5}$
0.91	9.0	$1.1 \times 10^{-4}$

## C.4 Equipment

The equipment used in this noise survey includes a receiver, an antenna, and a data acquisition system. The receiver was a Kenwood R-2000. It is capable of a 150- to 30,000-kHz digitally controlled tuning range and in the FM mode has a 15-kHz bandwidth. (A plot of the

bandpass of the receiver is shown in Figure C-5.<sup>2</sup>) Because the receiver also has a programmable frequency-scan mode, it can be used as a spectrum analyzer. The data acquisition system consists of a Compaq 286 Portable computer with a high-rate analog-to-digital card installed. The A/D card has a 100-kHz single-channel throughput and 16-bit resolution. The antenna system was a vertical monopole constructed of copper water pipe 1.6 cm in diameter. The length of the antenna was adjustable from 3.05 to 4.75 m. An artificial ground plane consisting of four 9.1-m radial wires was normally used. Ground rods pushed into the soil were used in an attempt to assess the effects of different grounding systems; existing water pipes were also used. On one occasion it was possible to connect the grounding bus into the ocean.

---

<sup>2</sup> The data for this plot were obtained by slowly stepping the receiver across the 2.25-MHz calibration signal in the programmable frequency-scan mode. The discontinuity at 2250 kHz is an artifact due to the receiver's frequency synthesizer.

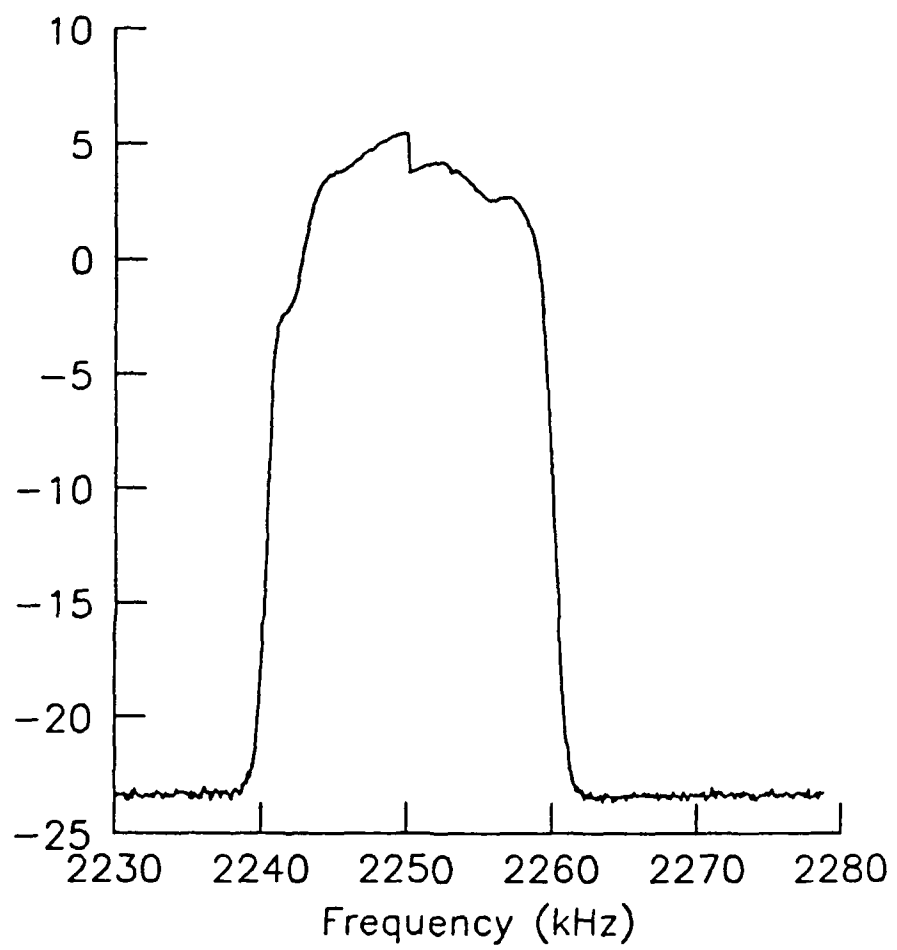


Figure C-5. Receiver bandpass.

## C.5 Data Acquisition

The data acquisition system was run in two modes. The scan mode was the primary method. In this mode, the receiver scanned through a preset range of frequencies and at each frequency 40 ms of data was collected at a rate of 8.0 kHz (320 samples). Normally, the "fast" frequency-scan rate was used, which stepped 5 kHz every 40 ms. The data collected at each frequency were reduced to four values: mean, standard deviation, minimum and maximum; the data were then logged to the hard disk. The second mode of data collection was continuous; in this mode data were logged continuously and the receiving frequency was not altered.

## C.6 Data Analysis

The data analysis yields a value for noise level relative to  $kTB$ . Before the antenna mismatch is compensated for, the internal-noise level of the receiver is subtracted from the total noise, or signal. This level was obtained from the frequency-scan calibration and was found to vary only slightly ( $< 1$  dB) from day to day. To place the ordinate in units of dB above  $kTB$ , the absolute level of the calibration signal was used as a reference value. At room temperature,  $kTB$  is approximately -162 dB, and the calculated level of the calibration signal with a  $50\text{-}\Omega$  resistive load attached to the receiver input is -127 dB.<sup>3</sup> Therefore, the calibration signal is approximately 37 dB above  $kTB$ . Prior to any processing, the calibration signal is -6.5 dB. Thus, to transfer the ordinate so that the value is relative to  $kTB$ , the ordinate values were shifted by 43 dB. For these comparative site survey measurements, no attempt was made to perform highly accurate calibrations; however, the measurements are thought to be accurate to 1 or 2 dB. A larger uncertainty is introduced by the assumption of a perfect antenna and ground plane.

### C.6.1 Absolute Power Level

#### C.6.1.1 Kauai

Figures C-6 and C-7 present the power level determined from data collected at different sites in Kauai. Published results of the expected power level are approximately 40 dB above  $kTB$  in the 2- to 3-MHz range. The results obtained here agree well with predicted levels. It is recognized that some of the modeling performed is not completely accurate and may contribute to the differences observed.

---

<sup>3</sup> This value was measured with the calibration attenuator set at -30 dB.

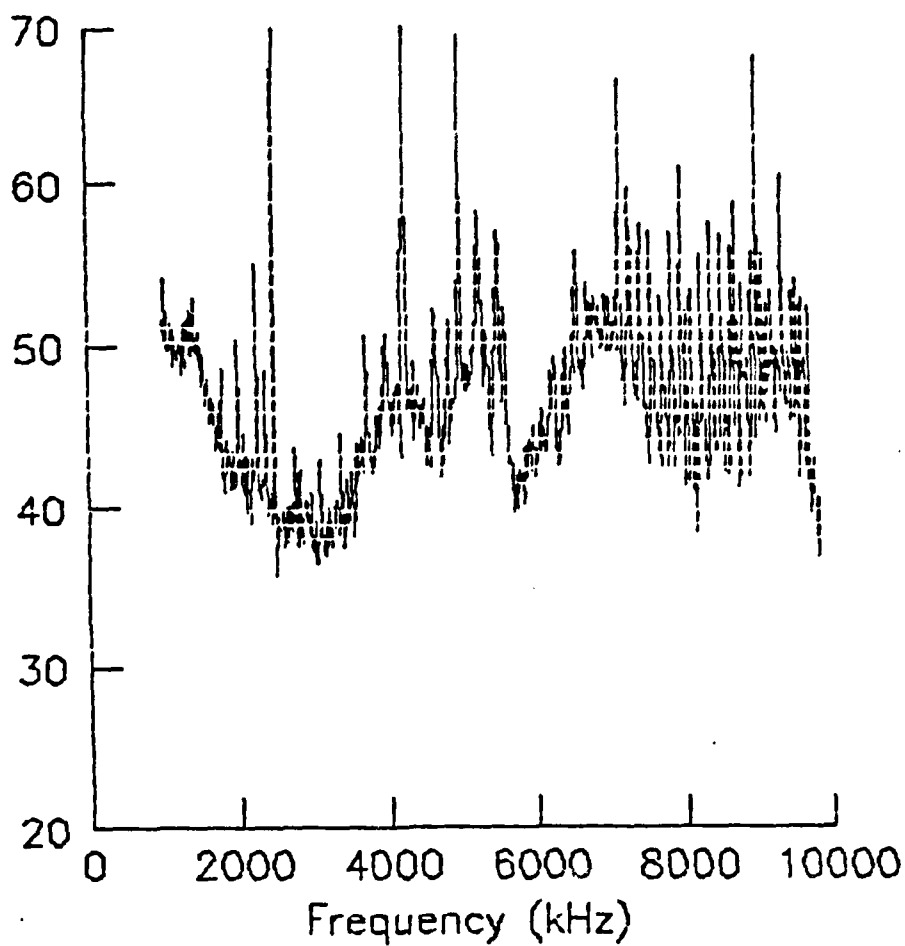


Figure C-6. Data collected at Polihale State Park. Antenna configuration: four 10-ft radials for ground plane, 500- $\Omega$  input impedance setting, receiver attenuation 0, calibration attenuator -30 dB.

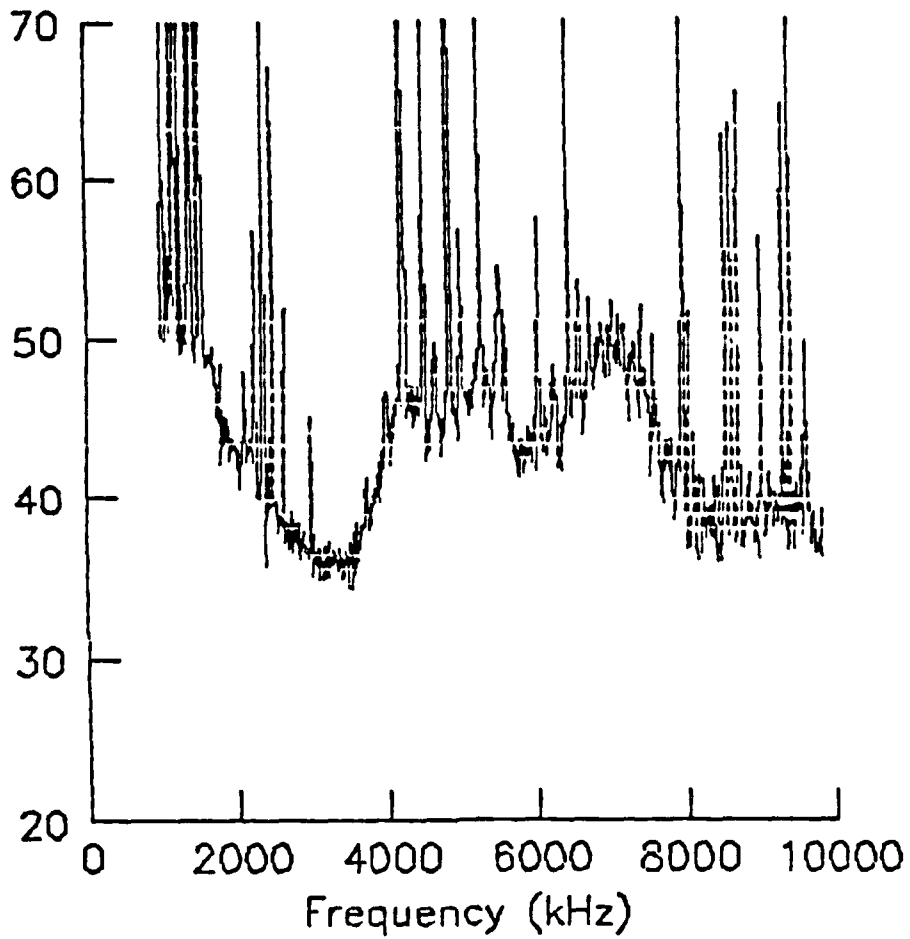
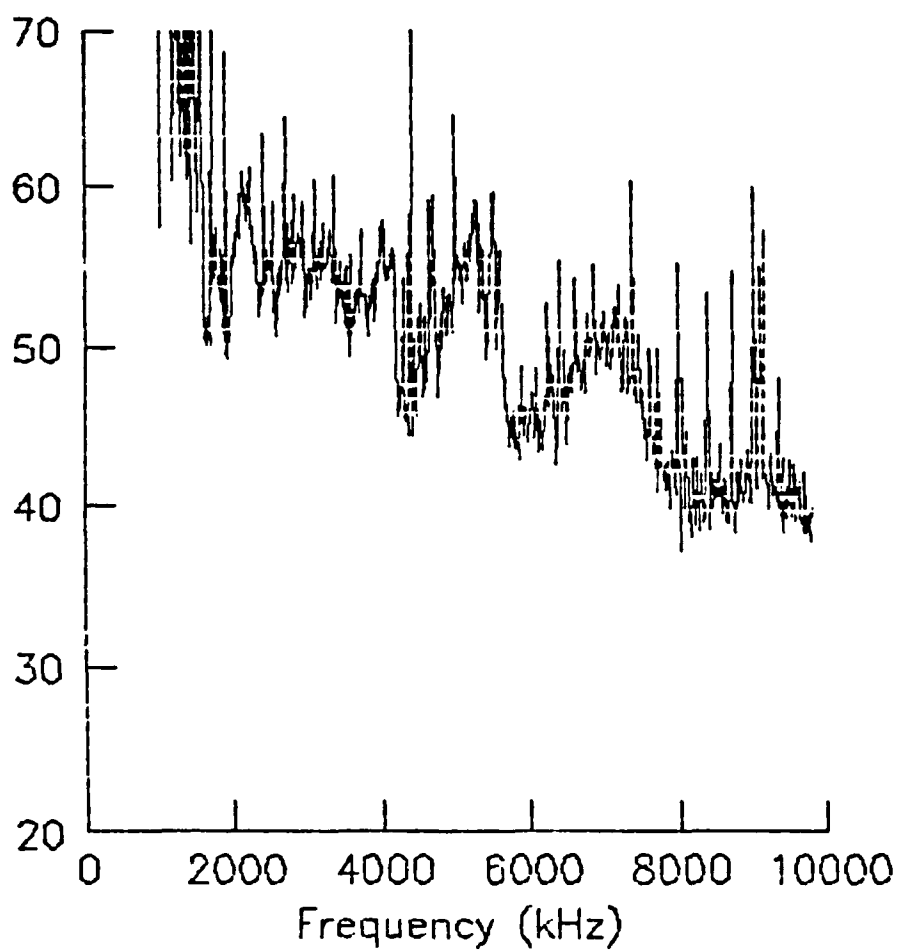


Figure C-7. Data collected at Poipu Beach area. Antenna configuration: four 10-ft dipoles for ground plane, 500- $\Omega$  input impedance setting, receiver attenuation 0, calibration attenuator -30 dB.

### C.6.1.2 Los Angeles Area

Figures C-8 and C-9 present the results for two sites in the Los Angeles area. It was expected that here the noise level would be much higher due to the presence of man-made noise. This was certainly borne out at the first site, located south of the city. However, the measurements made north of the city, at Pt. Dumé Beach, were significantly different. The measurements at the southern site were made on a weekday, while those at Pt. Dumé were made on a weekend; this may be a cause of the difference in rf activity. However, it is more likely that the reason has to do with the site itself. A complete explanation is not available; however, in the 2- to 4-MHz band the noise at both sites in the Los Angeles area is higher by 5 to 15 dB than it is in Kauai.



**Figure C-8.** Data collected at Morro Beach. Antenna configuration: four 10-ft radials for ground plane, 500- $\Omega$  input impedance setting, receiver attenuation 0, calibration attenuator -30 dB.

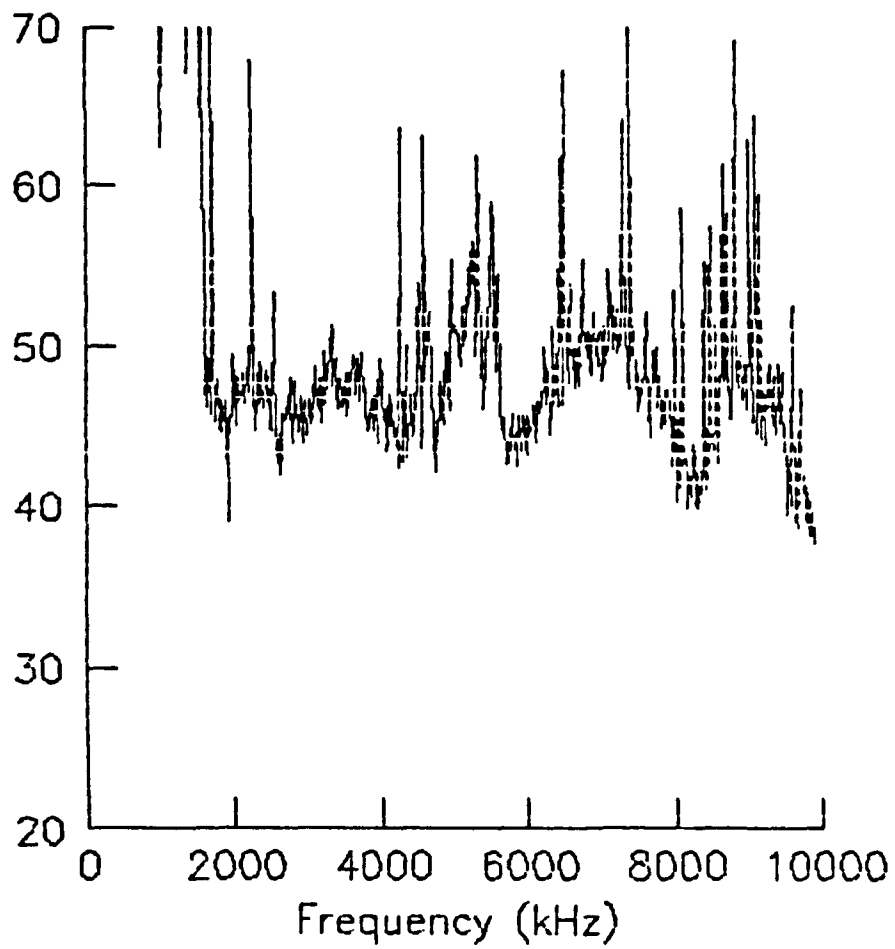


Figure C-9. Data collected at Pt. Dumé State Beach. Antenna configuration: four 10-ft radials for ground plane, 500- $\Omega$  input impedance setting, receiver attenuation 0, calibration attenuator -20 dB.

## C.7 Conclusions

Measurements indicate that the noise levels are consistent with expected results. In southern California the noise level was as much as 20 dB greater than that measured in Kauai. The biggest differences occurred below 5 MHz, and are evidently the result of human activity. Thus, the island of Kauai presents a low-noise environment with easy physical access in which to perform the initial SWOTHR experiments.

**Appendix D**

**Synopsis of Experiments Performed in Kauai, Hawaii, in Support of SWOTHR**

## D.1 Introduction

Surface-Wave Over-the-Horizon Radar (SWOTHR) is a radar-system concept designed in particular to detect low-flying (surface-skimming) high-speed threats to a battle group. Surface waves hugging the highly conductive sea provide the propagation mechanism needed to reach threats hidden below the horizon. SWOTHR employs a single illuminator (transmitter) on one ship and three or more receivers carried by various ships in a battle group. Targets are detected coherently at each receiver and tracked by combining the time delay and Doppler shift information from the various receivers.

The SWOTHR experiment is designed to verify basic multistatic surface-wave radar detection and tracking concepts. It will demonstrate system capabilities using inexpensive, off-the-shelf hardware.

The SWOTHR field tests were performed in May of 1988. The experiments performed in Kauai, Hawaii, in support of the SWOTHR program included five to seven data sets. Three of these data sets had a preplanned flight available. This document details the preplanned flight experiments that were performed, the configuration utilized, and the flight made in support of Project 1014 by Vista Research, Inc.

## D.2 Flight Experiments

Three data sets were collected with preplanned flights. The aircraft was an A-4 Navy jet. These data sets were collected on 12 May, 16 May, and 18 May, 1988. The following sections detail the flight scenario and the operations. During these experiments manual logs were maintained to record the exact time of data collection. These logs are also presented.

### D.2.1 Flight Operation 1 (12 May 1988)

#### D.2.1.1 General Information on Flight Operation 1

Operations began at approximately at 07:00 local time. No significant problems occurred in setting up either the receiver sites or the transmitter sites. At approximately 08:30 it was discovered at the Port Allen site that the data acquisition system was not functioning correctly. This failure was due to a cold solder joint on the IDC connector from Receiver 2 to the computer. The cold solder joint was repaired and the data acquisition proceeded as expected. The run began at 13:30, with the plane departing at 13:29. A

detailed timetable defining the flight plan and the data acquisition is presented below. Details of the flight plans are available in Appendix A. The A-4's radar altimeter was not operational.

### D.2.1.2 Details of Flight Operation 1

#### Receiver 1 (South)

	X-Coordinate (m)	Y-Coordinate (m)	Path Length (m)
Location Relative to Transmitter	-10990	17000	20243
Carrier Frequency (MHz)	2.8		
Pulse Repetition Frequency (Hz)	244.14026		

#### Receiver 2 (North)

	X-Coordinate (m)	Y-Coordinate (m)	Path Length (m)
Location Relative to Transmitter	-2600	7700	8127
Frequency (MHz)	2.8		
Pulse Repetition Frequency (Hz)	244.14026		

#### Flight Plan (Pilot : Lt. Shane Hendricks)

<u>Time</u>	<u>Comment</u>
12:29:00	Take off. Climbed to 1000 ft. Turned South, radial 170. Descended.
12:30:30	Intercepted radial 190 at 5 nmi (nautical miles). Descended to 450 ft on barometric altimeter. Increased air speed to 420 kias. Lost TACAN at 20 nmi, time not noted.

12:41:00 Up to 1000 ft. 71 nmi DME on 196 radial. (left turn)

12:42:00 Heading 010 at 450 kias at 400 ft indicated barometric altimeter. Note there is an E/W drift.

12:48:00 Cutoff TACAN at 33 nmi on radial 210. Corrected heading to 015 airspeed 450 kias.

12:51:00 Location 10 DME. Commenced right hand turn to 1000 ft (350 kias).

12:52:00 Outbound 10 DME airspeed 420 kias. Altitude 450 ft indicated.

12:58:00 Commence climbing left-hand turn. Acquired TACAN at 3000 ft 60 nmi on radial 192.

13:00:00 60 DME heading 010 at 450 kias with an altitude of 400 ft.

13:05:00 Acquired TACAN at 24 nmi on the 196 radial corrected to 020 heading.

13:07:00 10 DME, outbound on radial 190, 420 kias, at an altitude of 400 ft.

13:14:00 Climbed to 3000 ft on 191 radial 60 nmi.

13:15:00 Turn inbound on heading 015, 450 kias, at 400 ft.

13:19:00 Acquired TACAN (did not note distance) corrected to 010 heading.

13:22:00 10 nmi DME at 010. Right-hand turn. Headed home.

Notes: Pilot noted that he thought the 400-ft altitude estimated by the barometric altimeter was high. Given the seastate he estimated altitude at 250-300 ft. DME = distance measuring equipment.

Data Acquisition Receiver 1 File name convention: 5121r1.nnn (where nnn is a consecutive file number)

(36 Buffers/file)

<u>Buffer</u>	<u>Time</u>	<u>@ File No.</u>	<u>Buffer</u>	<u>Time</u>	<u>@ File No.</u>
10	12:30:11	0	2000	13:04:57	55
100	13:31:45	2	2100	13:06:42	58
200	12:33:30	5	2200	13:08:27	61
300	12:35:15	8	2300	13:10:12	63

400	12:37:00	11	2400	13:11:57	66
500	12:38:45	13	2500	13:13:42	69
600	12:39:29	16	2600	13:15:06	72
700	12:42:14	19	2700	13:17:01	75
800	12:43:59	22	2800	13:18:56	77
900	12:45:44	25	2900	13:20:41	80
1000	12:47:29	27	3000	13:22:26	83
1100	12:49:14	30	3100	13:24:11	86
1200	12:50:58	33	3200	13:25:56	88
1300	12:52:43	36	3300	13:27:41	91
1400	12:54:28	38	3400	13:29:25	94
1500	12:56:13	41	3500	13:31:10	97
1600	12:57:58	44	3600	13:32:55	100
1700	12:59:43	47	3700	13:34:40	102
1800	13:01:28	50	3800	13:36:25	105
1900	13:03:02	52			

Data Acquisition Receiver 2 File name convention: R5121r2.nnn (where nnn is a consecutive file number)

<u>File No.</u>	<u>Time</u>	<u>File No.</u>	<u>Time</u>
15	12:39:30	56	13:05:17
17	12:40:45	58	13:06:33
19	12:42:00	61	13:08:27
21	12:43:16	64	13:10:19
23	12:44:32	66	13:11:34
25	12:45:47	68	13:12:50

29	12:48:18	70	13:14:05
32	12:50:11	72	13:15:20
34	12:51:27	74	13:16:36
36	12:52:42	76	13:17:54
39	12:54:35	85	13:23:32
41	12:55:51	88	13:25:25
43	12:57:07	90	13:26:40
45	12:58:22	92	13:27:56
47	12:59:38	94	13:29:12
49	13:00:51	96	13:30:27
52	13:02:47	99	13:32:20
54	13:04:01	101	13:33:36
103	13:34:52		

## D.2.2 Flight Operation 2 (16 May 1988)

### D.2.2.1 General Information on Flight Operation 2

Operations began at approximately at 07:00 local time. No significant problems occurred in setting up either the receiver sites or the transmitter sites. At approximately 08:30 it was discovered at the Port Allen site that the data acquisition system was not functioning correctly. The cause of this failure was an intermittent short circuit between the receiver/computer connector circuit board and the receiver chassis. The failure was corrected and the error did not recur. The data run began at 11:50, with the airplane taking off at 11:48:30. A detailed timetable defining the flight plan and the data acquisition is presented below. Details of the flight plans are available in Appendix A. Note that the radar altimeter was not operational.

### D.2.2.2 Details of Flight Operation 2

#### Receiver 1

	X-Coordinate (m)	Y-Coordinate (m)	Path Length (m)
Location Relative to Transmitter	-10990	17000	20243
Frequency (MHz)	2.8		
Pulse Repetition Frequency (Hz)	390.625		

#### Receiver 2

	X-Coordinate (m)	Y-Coordinate (m)	Path Length (m)
Location Relative to Transmitter	-2600	7700	8127
Frequency (MHz)	2.8002		
Pulse Repetition Frequency (Hz)	390.625		
Carrier Frequency (MHz)	2.8		

#### Flight Plan (Pilot : Lt. Shane Hendricks)

<u>Time</u>	<u>Comment</u>
11:48:30	Take off. Air speed 350 kias attaining altitude of 500 ft.
11:50:00	5 nmi DME. Heading 180. 450 kts. Altitude 300 ft.
11:58:00	64 nmi DME. Radial 180. 450 kias.
11:59:00	Heading 360. Altitude 300 ft. 450 kias.
12:02:00	Heading 004. Altitude 300 ft. Distance not noted.

12:06:00 10 DME, Heading 005. Increased elevation to 1200 ft (R) turn.  
 12:07:00 Heading 180. Altitude 300 ft. 450 kias.  
 12:13:00 62 nmi (did not note DME, this is a wag). Increased elevation to reacquire TACAN (3500 ft).  
 12:17:00 Heading 180. Altitude 300 ft. 450 kias  
 12:21:00 10 nmi DME. Radial 185  
 12:28:00 Radial 004. 300 ft. 450 kias (distance not noted).  
 12:39:00 17 nmi DME. radial 004. Right-hand climb.

Notes: Lost and reacquired TACAN at approximately 20 nmi.  
 DME = distance measuring equipment.

Data Acquisition Receiver 1 File name convention: R5161r1.nnn (where nnn is a consecutive file number)

<u>File No.</u>	<u>Time</u>	<u>File No.</u>	<u>Time</u>
1	11:50:24	64	12:15:11
2	11:50:48	76	12:19:54
3	11:51:11	88	12:24:38
4	11:51:34	100	12:29:20
16	11:56:18	101	12:29:43
28	12:01:02	102	12:30:07
40	12:05:48	103	12:30:30 (observed)
52	12:10:28		12:30:30 (predicted)

Data Acquisition Receiver 2 File name convention: R5161r2.nnn (where nnn is a consecutive file number)

<u>File No.</u>	<u>Time</u>	<u>File</u>	<u>Time</u>
3	11:51:12	51	12:10:05
6	11:52:23	56	12:12:02

8	11:53:10	60	12:13:37
10	11:53:57	64	12:15:10
12	11:54:45	66	12:15:15
16	11:56:19	74	12:19:07
21	11:58:17	78	12:20:42
24	11:59:28	82	12:22:16
28	12:01:02	86	12:23:30
32	12:02:36	90	12:25:25
36	12:04:11	94	12:27:00
40	12:05:46	99	12:28:57
44	12:07:20	102	12:30:08 (observed)
48	12:08:06		12:30:08 (predicted)

### D.2.3 Flight Operation 3 (18 May 1988)

#### D.2.3.1 General Information on Flight Operation 3

Operations began at approximately at 07:00 local time. As expected the 7.8-MHz frequency would not work due to the large amount of noise created on Receiver 2. Although this problem was not present at Receiver 1, it was decided to change the carrier frequency to 7.8125 MHz. Upon landing the plane burned up the brakes and the operation was delayed approximately 45 min. The operation began at 11:30. The plane did not depart until 11:35 due to a malfunction. This caused a loss of approximately 7 min of data. The radar altimeter was operational.

### D.2.3.2 Details of Flight Operation 3

#### Receiver 1

	X-Coordinate (m)	Y-Coordinate (m)	Path Length (m)
Location Relative to Transmitter	-10990	17000	20243
Frequency (MHz)	7.8125		
Pulse Repetition Frequency (Hz)	390.625		

#### Receiver 2

	X-Coordinate (m)	Y-Coordinate (m)	Path Length (m)
Location Relative to Transmitter	-2600	7700	8127
Frequency (MHz)	7.8125		
Pulse Repetition Frequency (Hz)	390.625		

#### Flight Plan (Pilot : Lt. Jay McCarthy & Unknown)

<u>Time</u>	<u>Comment</u>
10:35:00	Airborne, 450 kias, 200 ft. (Time not noted). Lost TACAN at 24 nmi DME.
10:44:00	(Time dry lab) 70 nmi. 180-181 radial.
10:45:00	Heading 360. 450 kias, 200-ft altitude. TACAN regained at 24 DME
10:54:00	10 DME

10:55:00 Radial/heading 180. 450 kias. 200 ft.  
TACAN lost at 24 DME.

11:02:00 73 DME, radial 177.

11:03:00 Heading 360. 450 kias. 200 ft.

11:11:00 Picked up TACAN at 24 DME.

Notes: Lost and reacquired TACAN at approximately 24 nmi. DME = distance measuring equipment. Log entries after 11:10:00 not recorded because data acquisition ended at this time.

Data Acquisition Receiver 1 File name convention: R5181r1.nnn (where nnn is a consecutive file number)

<u>File No.</u>	<u>Time</u>	<u>File</u>	<u>Time</u>
2	10:30:49	66	10:55:58
3	10:31:18	78	11:00:41
4	10:31:35	90	11:05:24
17	10:36:47	100	11:09:20
30	10:41:50	101	11:09:44
42	10:46:32	102	11:10:07 (observed)
54	10:51:15		11:10:06 (predicted)

Data Acquisition Receiver 2 File name convention: R5181r2.nnn (where nnn is a consecutive file number)

<u>File No.</u>	<u>Time</u>	<u>File</u>	<u>Time</u>
0	10:30:00	62	10:54:28
19	10:37:31	66	10:56:03
21	10:38:19	72	10:58:25
24	10:39:30	76	11:00:00
26	10:40:17	80	11:01:35
28	10:41:04	84	11:03:09

32	10:42:39	88	11:04:44
36	10:44:14	92	11:06:20
40	10:45:48	96	11:07:54
44	10:47:24	99	11:09:05
48	10:48:58	101	11:09:53
54	10:51:19	103	11:10:40 (observed)
58	10:52:54		11:10:30 (predicted)*

---

\* Note: Difference between observed and predicted ending times corresponds to the loss of one transmitter probe per 2 s (0.13%).